SHINING LIGHT ON THE KONDO LATTICE: AN ANGLE RESOLVED PHOTOEMISSION STUDY OF HEAVY FERMION FORMATION IN URu_2Si_2 AND $YbAl_3$

A Dissertation

Presented to the Faculty of the Graduate School

of Cornell University

in Partial Fulfillment of the Requirements for the Degree of

Doctor of Philosophy

by

Shouvik Chatterjee

January 2017

© 2017 Shouvik Chatterjee
ALL RIGHTS RESERVED

SHINING LIGHT ON THE KONDO LATTICE: AN ANGLE RESOLVED PHOTOEMISSION STUDY OF HEAVY FERMION FORMATION IN URu_2Si_2 AND $YbAl_3$

Shouvik Chatterjee, Ph.D.

Cornell University 2017

Kondo lattices are a fascinating class of intermetallic compounds that contain certain rare earth elements such as Ce, Yb, U, and Eu, where the interaction between the localized f electrons at the rare earth sites and the delocalized conduction sea leads to exciting emergent properties, such as unconventional superconductivity, quantum criticality, valence fluctuation etc. In this thesis, we describe how momentum-resolving capabilities of angle-resolved photoemission spectroscopy (ARPES), performed with high energy resolution at the milli-electron volt scale help disentangle subtle changes in electronic structure in these multi-band systems, thus providing important insights into the microscopic mechanisms at play. Ability to directly visualize how electrons organize themselves in these strongly correlated systems also help reveal important characteristics of these materials, often unexpected in conventional theories of the Kondo lattice.

We report ARPES experiments on single crystals of the actinide heavy fermion compound, URu_2Si_2 that undergoes a second-order phase transition at 17.5 K, order parameter for which still remains enigmatic. We establish that the hidden-order phase transition is associated with an abrupt opening of a hybridization gap leading to the formation of a coherent heavy fermion liquid. This is in contrast to a gradual gap opening scenario via a crossover expected

from a Kondo lattice indicating coupling of the heavy fermion state to the hidden order parameter.

Next, we describe our efforts at first synthesis of epitaxial thin films of a prototypical mixed valence compound $YbAl_3$. Employing *in situ* ARPES we reveal that the temperature dependent change in average Yb valence manifests itself as a dramatic shift in chemical potential leading to a Lifshitz transition at low temperatures. Furthermore, independently estimating temperature dependent changes in Yb valence and Luttinger volume we, for the first time, establish a precise one to one correspondence between *r*-space and *k*-space electronic structure in $YbAl_3$ that should be generic to any mixed valence system. We also spectroscopically establish emergence of coherence in the *f*- derived states at $\approx$ 37 K by directly measuring temperature dependent changes in the quasiparticle lifetime and identify dispersive crystal electric field (CEF) split states. We describe how our photoemission results can help us understand results from transport, thermodynamic and quantum oscillation measurements on this system. We conclude with exciting prospects and new directions, such as dimensionality control of effective hybridization in *f* electron systems that has become a possibility with the advancement in synthesis and spectroscopy techniques, and in particular by a combination of the two.

BIOGRAPHICAL SKETCH

Shouvik Chatterjee was born in Burdwan and raised in Asansol, both in West Bengal, India. While at high school he developed his interest in science, thanks in no small parts to his excellent teachers. Following his interests he decided to pursue his undergraduate studies in physics at the Indian Institute of Technology, Kharagpur. As an undergraduate student he has received KVPY (*Kishore Vaigyanik Prohotsahan Yojana*) fellowship from the Govt. of India, an associateship at the Saha Institute of Nuclear Physics, Kolkata and has been a part of the NIUS (*National Initiative on Undergraduate Science*) program. He graduated with a Bachelors and a Masters degree in science in 2010, earning the J. C. Ghosh memorial gold medal.

During his time at Kharagpur he spent a summer as an exchange student at University of California, Berkeley, working with Professor Irfan Siddiqi on quantum nanoelectronics. His experiences, while at Berekely, inspired him to apply for a Ph.D. program in the United States. He arrived at Cornell in the fall of 2010 and in the summer of 2011 joined the research group of Professor Kyle Shen. Here, he has had the unique opportunity to learn both the techniques of angle-resolved photoemission spectroscopy (ARPES) and molecular beam epitaxy (MBE), and develop relevant instrumentation. He received a Master of Science from Cornell University in January, 2014 while pursuing research on Kondo lattice systems, most of which is presented in this thesis.

To,

Mom and Dad

for being there, ALWAYS.

ACKNOWLEDGEMENTS

Six years, perhaps is a long time for any endeavor! And, it is only with the love, support and guidance from my family, friends and peers that I have been able to navigate, during all these years through the trials of graduate school, at the same time enjoying what has been a thoroughly wonderful and enriching experience.

First of all, I would like to thank my adviser Kyle M. Shen, who had given me the chance to learn about ultra-high vacuum, photoemission and strong correlations. I have learnt a great deal from him, not just about the scientific aspects of our group's research, but also how to communicate scientific ideas in a clear, concise and effective manner. Kyle is helpful, approachable, and provides a degree of independence to his students. He has even ensured that all of us are properly caffeinated, a very important aspect of graduate school in my opinion, by purchasing several fancy espresso machines for the group.

I have learnt everything about 'thin films' growth from Darrell Schlom, to whom I owe a heart-felt gratitude. I am indebted to him for his incredible support and ever-willingness to do everything possible in-order to turn ideas into concrete results, which in my case included procuring new materials, making new crucibles, fabricating new sleeves and so on. It is fair to say, without his support much of the work would not have seen the light of the day. I have benefited greatly from his astute understanding of scientific equipments, encyclopedic knowledge of materials and his meticulous attention to detail. Of course, our lab would have been a much boring place without his infectious enthusiasm for science and hearty laughter.

Successful experimental research, in many ways, relies on good team work that starts with a vibrant and active research lab. I have been fortunate to be a

part of the Shen-Schlom group that has been a huge influence on my development as a researcher. Yuefeng Nie had been a great mentor, who took me under his wings and got me started on both epitaxial thin film growth and photoemission. John Harter, Eric Monkman and Daniel Shai painstakingly taught me every aspect of our lab, including maintenance and operating procedures. Phil King, Masaki Uchida, Jason Kawasaki and Yang Liu, each brought a new perspective and fresh ideas with them and it has always been great to have them around. Bulat Burganov and I started graduate school, joined the lab, and are now graduating almost at the same time. We have shared numerous great moments together, both in an off the lab, from the soccer pitch to sky-diving! Those memories will always be cherished. It has been a joy to watch Haofei Wei, Ed Lochochoki, Jacob Ruf, Brendan Faeth and Jocienne Nelson mature and grow as a researcher. I feel assured our lab could not have been passed on to more accomplished hands. It has been a pleasure to work alongside excellent material scientists from Darrell's group. John Heron, Julia Mundy, Hari Nair, Charles Brooks, Che-Hui Lee, Hanjong Paik, Zhe Wang, Eva Smith, Carolina Adamo, Chiara Sacco, Alicia Galdi, Natalie Dawley, Jessica Burton, Rachel Steinhardt all of you will be missed.

Over the course of the past six years I have been fortunate to collaborate with some of the brightest and accomplished minds. For the URu_2Si_2 project, collaboration with Dr. Jochen Geck's group at TU Dresden was very helpful and enriching. Particularly, it was a pleasure to work with Jan Trickauf, with whom I spent couple of sleepless nights at the BESSY synchrotron and shared numerous stimulating discussions. Along with Jan, thanks are due to Nadine Heming and Torben Hänke, for making me feel at home in far off Berlin. I am grateful to Travis Williams and Graeme Luke for providing us with excellent

quality pre-cut URu_2Si_2 single crystals without which this project would not have been accomplished. Back at home, I have greatly benefited working with Lena Kourkutis and Suk Hyun Sung who helped me understand the structural aspects of our $YbAl_3$ / $LuAl_3$ thin films by performing beautiful TEM imaging. I am also thankful to Jacob Ruff and Ken Finkelstein for helping me carry out x-ray diffraction and scattering experiments, respectively, at the Cornell High Energy Synchrotromn facility (CHESS). It has been a privilege to have Professors J.C. Seamus Davis and Erich Mueller on my dissertation committee. I have benefited greatly from their wealth of knowledge, keen eye and high standards.

Life in Clark Hall would not have been the same without active help and support from a few extremely hard-working and caring individual. I am grateful to Nate Ellis for teaching me how to *'make stuff'*. Bob Tilloston, Stan McFall, Chris Cowulich, and Jeff Koski was always there for help and advice. Bob, in particular always had an idea whenever I was stuck and machined extremely complicated parts with incredible ease. Rodney Bowman, Stephan Felix and James Sears frequently indulged me with my rush orders. Linda Hatch efficiently processed numerous orders, many of them to foreign companies and Leonard Freelove always brought every ordered package to us without misplacing a single one.

I have been immensely lucky to have incredible friends who made six long years in Ithaca a memorable one. Siddharth, Sudip, Arunima, Hema, Amit, Anshumali, Vikram, Leah, Tanvi, Oleg, Gabriela, Devon, Starr, May, Dave, Sumita, Tushar, Poornima, Matthew, Abhishek and Gunjan, I will miss our hiking trips, Friday night dinners, racquet games, and endless conversations. Thank you all for the good times!

Finally, and most importantly I could not have kept going without active

support, love and constant encouragement from my family. My mom and dad, to whom this thesis is dedicated, did everything possible to make sure I always had all the opportunities open to me and have always supported me in all my decisions. They called me everyday without fail for the last six years making sure I am sane and keeping well. Even though I was thousands of miles away, I never really felt they are far away. My beautiful wife, Vidhya is a source of endless love, inspiration and support, and is the reason why after more than six years I still keep a level-head.

Shouvik Chatterjee

Ithaca, 2016

TABLE OF CONTENTS

LIST OF FIGURES

CHAPTER 1

INTRODUCTION

"The behavior of large and complex aggregations of elementary particles, it turns out, is not to be understood in terms of simple extrapolation of the properties of few particles. Instead, at each level of complexity entirely new properties appear, and the understanding of the new behaviors requires research which I think is as fundamental in its nature as any other" -Philip W. Anderson in 'More is Different' (1967)

From the earliest of times the eternal human quest for knowledge about the natural world has taken a reductionist approach. This idea can be traced back to the ancient Indian, Chinese and Greek philosophies where the world was thought to comprise of five classical elements, a combination of them believed to be able to create everything known to the ancient world. The same spirit guided the discovery of atoms, electrons, quarks, continuing to the present day discovery of the Higgs boson, and is at the heart of our attempts to understand gravitation and quantum mechanics within a one single theoretical framework, aptly called the *"Theory of Everything"*, in striking resemblance to the ideas of our ancient forefathers. But along the way we stumbled upon something equally fantastic, perhaps having its roots in the Darwinian appreciation of complexity in the living organisms and in their gradual evolution. That, when aggregates of apparently simple constituents are combined, completely unanticipated exotic collective behaviors can emerge with no equivalence at the single constituent level. Condensed matter physics, in particular, is awash with numerous such examples including superconductivity, heavy fermions, topological insulators, quantum integer and fractional hall effect etc., many of them having been dis-

covered by *'accident'*.

A major breakthrough in our theoretical understanding of *many-particle systems* came from Lev Landau's *Fermi liquid theory*, where he showed that the many body problem, in cases where the interaction is weak, could be recast as a single particle problem. The particles now are composite quasiparticles that carry the effects of interactions with them in terms of their renormalized effective mass. Such an interpretation formed the basis to understand why a description in terms of Bloch waves work very well for *'simple metals'*. This description then naturally also became a starting point to understand properties belonging to the realm, beyond that of a *'simple metal'*, in terms of residual interactions.

Strongly correlated electron systems are materials which are on the other 'extreme' of that of the *'simple metals'*, in the sense that residual interactions are so strong that the whole *'Fermi liquid'* description itself starts to break down. Though significant progress has been made in our understanding of the strongly correlated systems, an over-arching theoretical tool to calculate the properties of such materials remains elusive. Therefore, though Fermi liquid theory provides a good starting point theoretical progress to understand these materials rely on appropriate approximation schemes, whose development relies extensively on the correct description of the observed experimental properties. It is at this frontier that major discoveries has been made where new, exciting, and completely unforeseen material properties has been found that has not only greatly advanced our understanding but also has had a major impact on modern technology. In recent times, advanced experimental techniques including the development of modern spectroscopy tools, precise material fabrication capabilities

along with sophisticated calculation methods has greatly accelerated our capacity to explore and understand novel functionalities in material systems.

Kondo lattice systems are a class of strongly correlated electron systems that exhibit a variety of exotic properties such as unconventional superconductivity, quantum criticality, hidden order, valence fluctuation etc. emerging out of *heavy fermionic* states that remains poorly understood. In this thesis we employ angle-resolved photoemission spectroscopy (ARPES) to understand *heavy fermion* formation and associated temperature dependent changes in the electronic structure in two Kondo lattice systems, viz. URu_2Si_2 and $YbAl_3$. Outline of the thesis is as follows. In Chapter 2, we describe the technique of ARPES, in particular its unique angle-resolving capabilities that allows directly visualization of the *k*-space resolved electronic structure of material systems. In Chapter 3, we describe Kondo lattice systems, their general characteristics and a broad theoretical framework to understand these compounds. In Chapter 4, we describe the mysterious *'hidden-order'* phase in URu_2Si_2. In Chapter 5, we present our photoemission results elucidating changes in its electronic structure in the *'hidden-order'* phase that reveals how a coherent heavy fermion liquid is formed via a phase transition in contrast to conventional wisdom for the Kondo lattice systems. In Chapter 6, we describe properties of $YbAl_3$, a prototypical mixed-valence system. We describe our efforts at epitaxial growth of thin films of $YbAl_3$ that brings this materials system, for the first time, under the purview of advanced spectroscopy tools such as ARPES. In Chapter 7, we describe momentum resolved electronic structure of $YbAl_3$ and its conventional metal analogue $LuAl_3$ as measured by our ARPES experiments and predicted by ab-initio calculations. In Chapter 8, by using a combination of high and low energy spectroscopy we establish a direct one to one correspondence between the *r*-space

and k-space electronic structure in $YbAl_3$, expected to be a generic feature for any mixed valence system. Finally, in Chapter 9, we exploit the full potential of our approach involving a combination of state-of-the-art tools of synthesis and spectroscopy, where we establish the ability to control effective hybridization between the Yb $4f$ states and the conduction like band electrons in $YbAl_3$ by reducing its effective dimensionality via fabrication of artificial superlattices, interrupting few atomic layers of $YbAl_3$ with $LuAl_3$ layers.

CHAPTER 2

ANGLE RESOLVED PHOTOEMISSION SPECTROSCOPY

2.1 Introduction

Angle resolved photoemission spectroscopy (ARPES) has emerged as a leading spectroscopic tool to directly visualize how electrons organize themselves in disparate crystal environments, providing invaluable insights into their emergent behavior, the over-arching theme of this thesis.[2, 3] Though in its current avatar it is a sophisticated technique with demanding system requirements,as discussed in this chapter, its underlying physical principle is quite simple, having its roots in the celebrated photoelectric effect discovered over a century ago.

2.2 Development of photoemission as a spectroscopic tool

First experimental evidence of the process of photoemission was provided by Heinrich Hertz in 1887 when he found that the electromagnetic radiation from an electrical arc can trigger another arc.[4] Subsequently, similar observations were reported by other experimenters, in particular by Philip von Lenard, who started his work as Hertz's assistant. The observed phenomenon was explained in terms of emission of charged particles on irradiation of a metal surfaces with ultra-violet light.[5, 6] With his Nobel prize (1905) winning work on cathode rays, von Lenard further demonstrated that the maximum energy of the emitted charged particles (electrons, known then as "cathode rays") is proportional to frequency of the incident light and not its intensity, at odds with the prevailing

Maxwellian notion of light as an electromagnetic wave. However, the number of emitted electrons were found to be proportional to the light intensity. In 1905, Albert Einstein inspired by the success of Max Planck's theory of light quanta in explaining the black body radiation,[8] proposed that the same quantized corpuscular nature of light can explain the experimental findings about the nature of the photoelectric effect.[7] Accordingly, he wrote down the celebrated Einstein equation for the photoelectric effect

$$E_{k,max} = h\nu - \phi \tag{2.1}$$

where, maximum kinetic energy of the emitted electrons is dependent on the energy of the incident light, ($h\nu$, h being the Planck's constant) and the work function of the metal (ϕ). Einstein was awarded the Nobel prize in Physics in 1921 for this novel interpretation, and to Millikan, in 1923, for experimentally verifying Einstein's interpretation with his photoemission experiments.[9] However, it was not until early 1960s that the full potential of this phenomenon was recognized as a powerful tool to probe the electronic structure of materials. Owing to the energy conservation encoded in Einstein's equation of the photoelectric effect, it was realized that this process could be used to gain knowledge about the energy distribution (density of states) of electrons in the cathodes. Indeed, Berglund and Spicer, working on Cu and Ag showed in 1964 that they can experimentally determine the position of the d band edge in these materials using photoemission that were found to agree with the predictions from band theory.[10, 11] In the same year, E.O. Kane proposed that by measuring the emitted electrons during the photoemission process in an angle-resolved manner, one can also obtain information about dispersive electronic states.[12] In 1974,

Smith, Tarum and Di Salvo, working with two dimensional layered compounds, TaS_2 and $TaSe_2$ performed first successful ARPES experiment establishing that it is indeed possible to map out momentum resolved electronic structure by exploiting the process of photoemission.[13, 14] Later, in 1981 Nobel prize was awarded to Kai Siegbahn for his contributions to the development of x-ray photoemission spectroscopy. Since those formative years of photoemission experiments ARPES of today has developed into a refined *k*-space probe, with orders of magnitude improvement both in energy and momentum resolving capabilities. In the following sections I describe quantum theory of the photoemission process, experimental considerations and current capabilities of state of the art ARPES setups. In the process, I also provide details of our own experimental setup at Cornell, and finally, describe analysis techniques commonly used to visualize and interpret ARPES data.

2.3 Theory of Photoemission

2.3.1 Kinematics and Energetics of ARPES

Photoemission is essentially a *photon in - electron out* process where, an incident photon is absorbed by an electron that in turns gets excited, and is emitted as a photoelectron, if the incident photon energy is more than the work function of the material surface. Work function of a material (ϕ), typically ranging between 3 - 5 eV, is a manifestation of the electric field present at the material surface that reduces the kinetic energy of the photoemitted electrons.[2, 15] Since photoemission is an energy conserving process, knowledge of the incident photon

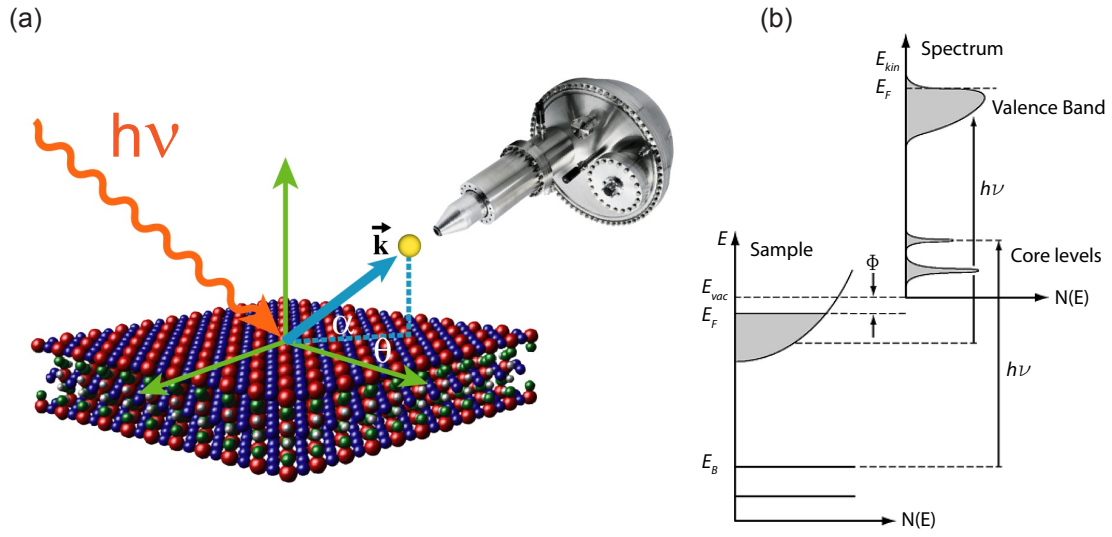

Figure 2.1: Schematic of the photoemission process. a) The measurement geometry is illustrated along with relevant kinematic angles. (*Figure courtesy Kyle M. Shen*) b) Energy diagram showing the initial states and the corresponding spectrum. Φ is the surface work function. Adapted from [15]

energy ($h\nu$) and work function (ϕ) of the material surface makes it possible to estimate the binding energy of the photoemitted electrons inside the solid, as is illustrated in Fig. 2.1

$$E_B = h\nu - E_{kin} - \phi \tag{2.2}$$

A clean flat ideal material surface preserves periodicity of the crystal along the in-plane (x,y) directions. Thus, in addition to energy conservation, as a consequence of Noether's theorem, the photoemission process must also conserve in-plane momentum within an in-plane reciprocal lattice vector **G**. As momentum of the incident photon can generally be neglected[15], the in-plane wavevector of the outgoing photoelectron $K_{\|}$ is related to the in-plane momenta $k_{\|}$ and the in-plane reciprocal lattice vector $G_{\|}$ as

$$K_{\parallel} = k_{\parallel} + G_{\parallel} \tag{2.3}$$

Therefore, from a knowledge of the experimental geometry in an angle resolved photoemission measurement in-plane momenta of electrons inside solids can be readily enumerated as

$$k_x = \sqrt{2m_e E_{kin}} sin\alpha cos\theta \tag{2.4}$$

$$k_y = \sqrt{2m_e E_{kin}} sin\alpha sin\theta \tag{2.5}$$

where angles are defined in Fig. 2.1.

However, determination of out of plane momenta k_z is tricky, as translation symmetry is broken along the surface normal resulting in k_z not being conserved during the photoemission process. But, because kinetic energy of the photoelectron (E_{kin}) is related to its wavevector ($\boldsymbol{k}$) $|\mathbf{k}| = \frac{1}{\hbar}\sqrt{2m_e E_{kin}}$, making use of kinematic constraints of the photoemission process and knowing what is known as inner potential V_0 [16], it is possible to obtain information about k_z

$$k_z = \sqrt{\frac{2m_e}{\hbar^2}(E_{kin} + V_0) - k_{\parallel}^2} \tag{2.6}$$

that can be written as

$$k_z = \sqrt{\frac{2m_e}{\hbar^2}(h\nu + V_0 - \phi) - k_{\parallel}^2} \tag{2.7}$$

using eqn. (2.2)

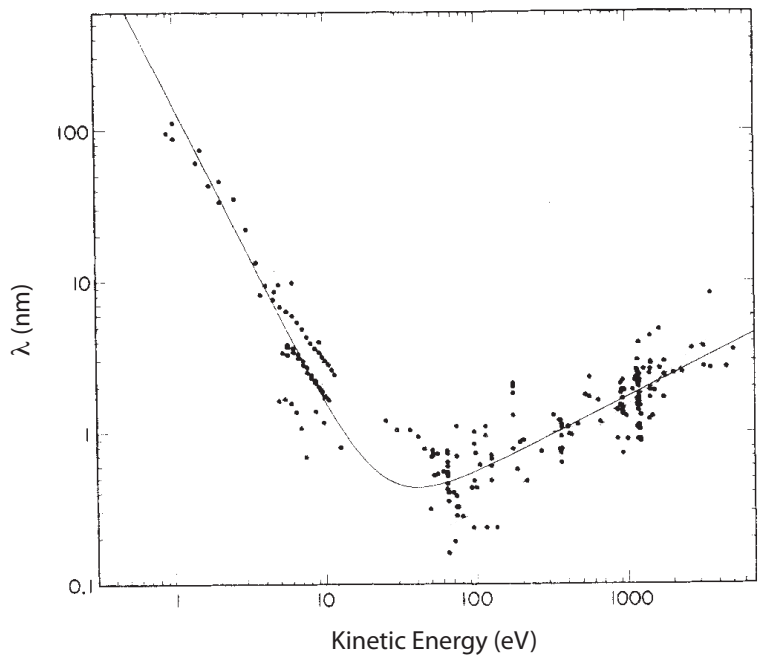

Figure 2.2: Universal Curve. A plot of the inelastic mean free path λ of electrons as a function of kinetic energy. Dots in black are experimentally measured data points while the smooth curve is a guide to eye. Adapted from [17]

V_0 can be given a physical meaning within a three-step model of the photoemission process, discussed in the next section. In practice, V_0 is determined by identifying how spectral features at a particular $k_{\|}$ repeat as incident photon energy is varied. From eqn. (2.7), it is immediately recognized that changing incident photon energy allows tuning of k_z, which should result in similar spectral features when identical k_z is accessed, knowing which V_0 can be calculated.

Electrons in solids interact strongly. As a result they are scattered easily leading to very short mean free path or electron escape depth, λ_{mfp} making the photoemission process extremely surface sensitive. Electron escape depths has been measured for many good metals and was found to depend strongly on incident photon energy as shown in the so-called *"universal curve"* in Fig. 2.2.[17] Thus,

ultra-clean pristine sample surface is required for photoemission, and accordingly photoemission measurements are done in ultra-high vacuum chambers with background pressure of the order of 10^{-11} torr. However, whether results of the empirical *"universal curve"* is 'universally' applicable to all materials (for example correlated complex oxides) is still an open question.

In addition, finite electron mean free path creates additional complication in determination of k_z, because it leads to intrinsic spectral broadening in accordance with Heisenberg's uncertainty principle. Broadening in k_z can be modeled with a Lorentzian profile with a full width at half-maximum (fwhm), $\Delta k_z = 1/\lambda_{mfp}$. This is a Fourier transform of a freely propagating waveform that has a step function at the sample surface and exponentially decays with a length scale λ_{mfp} into the solid. Therefore, experimentally measured photoemission intensity is the weighed average of the spectral function over the length scale, λ_{mfp} that can cover a significant fraction of the Brillouin zone under certain circumstances. To underscore this important aspect, simulated photoemission spectra from a free-electron like band is shown in Fig. 2.3 for different values of Δk_z. As can be clearly observed, when $\Delta k_z \ll \pi/c$ photoemission spectrum as a function of photon energy tracks the dispersion in k_z, while in the other limit $\Delta k_z \gg \pi/c$, simulated spectra does not show any k_z dispersion providing only the averaged spectrum irrespective of incident photon energy. In reality, ultra-violet ARPES falls in between these two extremes, but care needs to be taken while analyzing experimental data from three-dimensional materials that can be strongly modulated by final state effects.

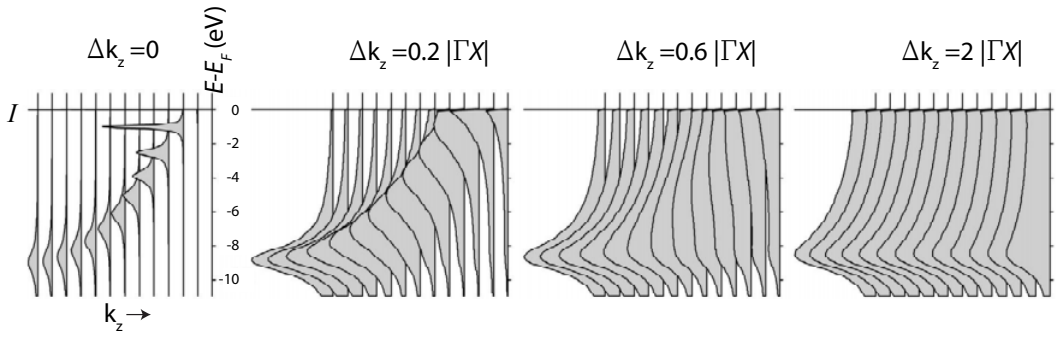

Figure 2.3: Simulated spectral function of a dispersive band for different intrinsic k_z broadening. For large δk_z values dispersion is washed out and the band appears to be two-dimensional in character. Adapted from [18]

2.3.2 The three-step Model

The process of photoemission involves absorption of a photon, emission of a photoelectron, and its subsequent detection. A rigorous description of the process is the so-called *one-step model* where all three processes are considered as a single coherent process. However, an analytical description of the process within such an approach is complex and extremely challenging. An alternate approach is the so-called *three-step model*[2, 10, 15] that has been shown to work very well in explaining experimental observations. The *three-step model* breaks up the photoemission process into three distinct steps.

The first step involves absorption of a photon that excites an electron within the solid in a *direct transition* to an excited state without a change in its crystal momentum k. (photon momenta can be neglected) leaves behind a hole. Actually, ARPES measures single hole spectral function of the material that can be significantly altered in presence of interactions making it a sensitive probe of correlations. Though negligible in magnitude compared to electron crystal

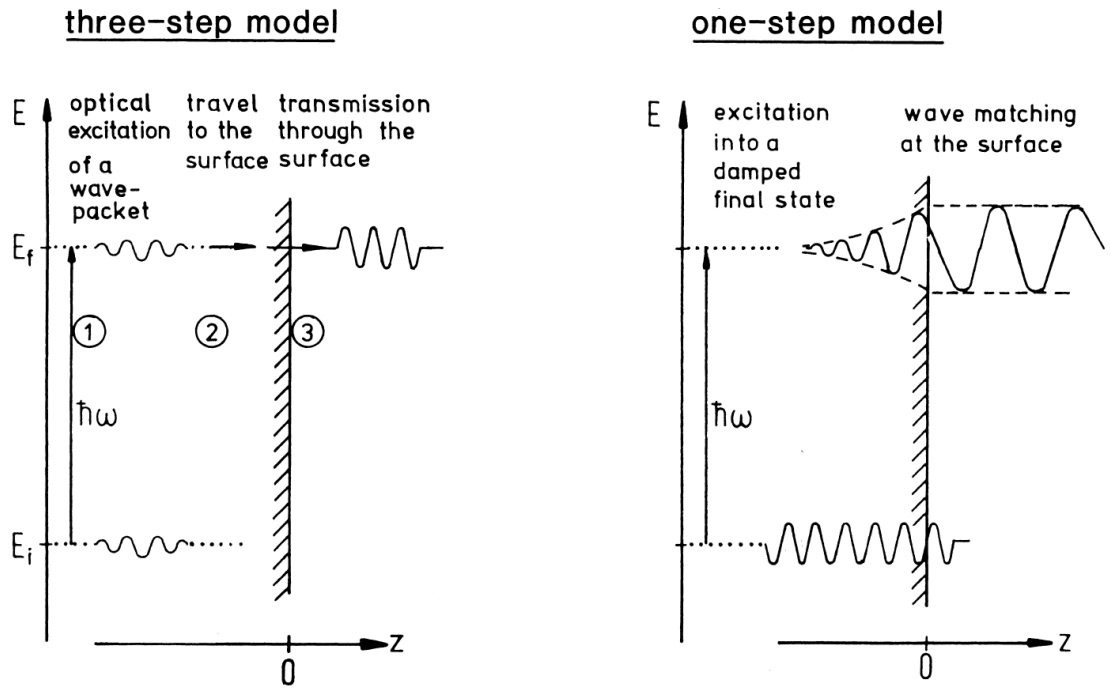

Figure 2.4: Illustration of the three-step and one step model used in understanding the photoemission process. Adapted from [2]

momentum, due to the involvement of photon momentum, the process obeys selection rules leading to polarization dependence of the measured spectrum. V_0, discussed in the previous chapter can now be understood as the energy offset describing the final state.

In the second step photo-excited electrons travel to the sample surface. In the process they can get scattered, probability of which is determined by the inelastic mean free path λ_{mfp}.

In the third step the electron escapes out of the sample into the vacuum and gets detected. During the process it has to overcome the electric field at the sample surface. (work function ϕ). In Fig. 2.4 description of the *one-step model* and *three-step model* is presented.

2.3.3 Fermi's Golden Rule and the sudden approximation

The first step described in the *three-step model* can be approximated using Fermi's golden rule that gives the photexcitation rate as[20]

$$\omega_{fi} = \frac{2\pi}{\hbar}|\langle\psi_f^N|H_{int}|\psi_i^N\rangle|^2\delta(E_f^N - E_i^N - h\nu) \tag{2.8}$$

where the N particle initial and final state energies can be written as $E_i^N = E_i^{N-1} + E_B^k$ and $E_f^N = E_f^{N-1} + E_{kin}$. The interaction hamiltonian capturing the excitation process can be written under certain approximations as

$$H_{int} = -\frac{e}{2m_e c}(\mathbf{A}.\mathbf{p} + \mathbf{p}.\mathbf{A}) = -\frac{e}{m_e c}(\mathbf{A}.\mathbf{p}) = -\frac{eA}{m_e c}(\hat{e}.\mathbf{p}) \tag{2.9}$$

where $\mathbf{p}$ is the electron momentum operator, $\hat{e}$ is the light polarization vector and $\mathbf{A}$ is the electromagnetic field potential due to the photon. Here, we have assumed that the intensity of the incident light is sufficiently low that non-linear effects such as two photon processes can be neglected and only terms linear in electromagnetic field potential $\mathbf{A}$ enters into the interaction hamiltonian. In addition dipole approximation is assumed to be valid i.e. $\mathbf{p}$ and $\mathbf{A}$ commutes as $\mathbf{A}$ is assumed to be constant over atomic dimensions, which is definitely true in the ultra-violet regime for bulk of the materials but may not necessarily hold at the material surface.

In order to be able to factorize the final state wavefunction ψ_f^N into the photo excited electron and the rest *sudden approximation* is commonly employed, that simplifies the description. This assumption entails that the process of photoexcitation happens so rapidly (*sudden*) that the time evolution of the excited state

with *(N-1)* electrons that is left behind, an eigenstate of *(N-1)*-particle hamiltonian is independent of that of the photoelectron. Thus, the emitted photoelectron is oblivious of any relaxation of the excited *(N-1)* electron state that might follow. Then the final state wavefunction ψ_f^N can be written as

$$\psi_f^N = \mathcal{A}\phi_f^{\mathbf{k}}\psi_f^{N-1} \tag{2.10}$$

where $\mathcal{A}$ is the anti-symmetrization operator, $\phi_f^{\mathbf{k}}$ is the wavefunction of the photoexcited electron with momentum $\mathbf{k}$ and ψ_f^{N-1} is the final state wave function of the (N-1) electron system that is left behind. Sudden approximation is ideally valid when photoexcited electrons have high kinetic energies when they should take negligible time to get emitted out of the sample with no post-excitation interaction. However, evidence of applicability of sudden approximation has been reported for photon energies as low as 20 eV in case of cuprate superconductors[21] and has been frequently used for laser based ARPES experiments using significantly low energy photons.[22] For simplicity, the initial state wavefunction ψ_i^N can be assumed as a single Slater determinant as within a Hartree-Fock formalism that allows the wavefunction to be written as a product state of a one electron orbital $\chi_i^{\mathbf{k}}$ (from which the photoelectron is excited) and an *(N - 1)* -particle term for the rest of the electrons of the material system

$$\psi_i^N = \mathcal{A}\chi_i^{\mathbf{k}}\psi_i^{N-1} \tag{2.11}$$

Now, ψ_i^{N-1} can also be written as $\psi_i^{N-1} = \hat{c}_{\mathbf{k}}\psi_i^N$ where $\hat{c}_{\mathbf{k}}$ is an annihilation operator for an electron with momentum $\mathbf{k}$. Thus, it is clear that ψ_i^{N-1} is not necessarily an eigenfunction of the *(N-1)*-particle hamiltonian but can be expanded

as sum of all possible eigenfunctions of the *(N-1)*-particle hamiltonian

$$\psi_i^{N-1} = \sum_m c_m^{\mathbf{k}} \psi_m^{N-1} \tag{2.12}$$

Combining everything together total photoexcitation rate for a particular momentum $\mathbf{k}$ is given by

$$\omega_{\mathbf{k}} = \sum_f \omega_{fi} = \frac{2\pi}{\hbar}(\frac{eA}{m_e c})^2 |M_{\mathbf{k}}|^2 \sum_m |c_m^{\mathbf{k}}|^2 \delta(E_{kin} + E_m - E_i - h\nu) \tag{2.13}$$

where $M_{\mathbf{k}} = \langle \phi_f^{\mathbf{k}} | \hat{\mathbf{e}}.\mathbf{p} | \chi_f^{\mathbf{k}} \rangle$ is the dipole matrix element of the transition, E_{kin} is the kinetic energy of the emitted photoelectron, E_m is the energy of the *(N-1)*-particle system left behind and E_i is the original ground state energy of the N-particle system. Photoemission only occurs when $E_{kin} + E_m = E_i + h\nu$, thus ensuring energy is conserved during the process. For a non-interacting system ψ_i^{N-1} is an eigenstate of *(N-1)*-particle system, hence the coefficient $c_m^{\mathbf{k}}$ is non-zero for a particular value of m. But, in case of interacting systems $c_m^{\mathbf{k}}$ for many different m values can be non-zero.

2.3.4 Single particle spectral function

One of the most powerful technique frequently used in the field of correlated electron systems is an approach based on Green's function formalism. Green's function method has been widely use to describe the response of a system to an external impulse. Time ordered one electron Green's function $\mathcal{G}(t - t')$ encapsulates the probability of finding an electron which was added or removed (impulse) at time t in a given state with momentum $\mathbf{k}$, in the same state at a later

time t'. [23] Applying a Fourier transform it is possible to write Green's function in energy-momentum space

$$\mathcal{G}(\mathbf{k},E) = G^{+}(\mathbf{k},E) + G^{-}(\mathbf{k},E) = \sum_{m} \frac{|\langle \psi_m^{N+1}|\hat{c}_{\mathbf{k}}^{\dagger}|\psi_i^N\rangle|^2}{E-(E_m^{N+1}-E_i^N)-i\eta} + \sum_{m} \frac{|\langle \psi_m^{N-1}|\hat{c}_{\mathbf{k}}|\psi_i^N\rangle|^2}{E-(E_m^{N-1}-E_i^N)-i\eta} \tag{2.14}$$

where, $G^{+}(\mathbf{k},E)$ and $G^{-}(\mathbf{k},E)$ are one-electron addition and one-electron removal Green's function respectively. From eqn.2.14 we obtain single particle spectral function $\mathcal{A}(\mathbf{k},E)$ as

$$\mathcal{A}(\mathbf{k},E) = -(1/\pi)ImG(\mathbf{k},E) = \mathcal{A}^{+}(\mathbf{k},E) + \mathcal{A}^{-}(\mathbf{k},E) =$$

$$\sum_m |\langle \psi_m^{N+1}|\hat{c}_{\mathbf{k}}^{\dagger}|\psi_i^N\rangle|^2 \delta(E - E_m^{N+1} + E_i^N) + \sum_m |\langle \psi_m^{N-1}|\hat{c}_{\mathbf{k}}|\psi_i^N\rangle|^2 \delta(E - E_m^{N-1} + E_i^N) \tag{2.15}$$

Comparing eqn.2.18 with eqn.2.13 and 2.8 it can be immediately appreciated that ARPES provides us information about one-electron removal spectral function that describe the propagation of one-hole or one-electron removal excitation in the many-body ground state. Thus, total photoexcitation rate in eqn.2.13 can be rewritten as

$$\omega_{\mathbf{k}} = \frac{2\pi}{\hbar}\left(\frac{eA}{m_e c}\right)^2 |M_{\mathbf{k}}|^2 f(h\nu - E_{kin})\mathcal{A}^{-}(\mathbf{k}, h\nu - E_{kin}) \tag{2.16}$$

where $f(E)$ is the Fermi-Dirac distribution added to explicitly take into account that electrons are photoexcited only from occupied states at a finite temperature.

Within a Green's function formalism a convenient way to account for the electronic correlations is by introducing the concept of electron self-energy $\sum(\mathbf{k},E) = \sum'(\mathbf{k},E) + \iota \sum''(\mathbf{k},E)$, where the real part encapsulates information

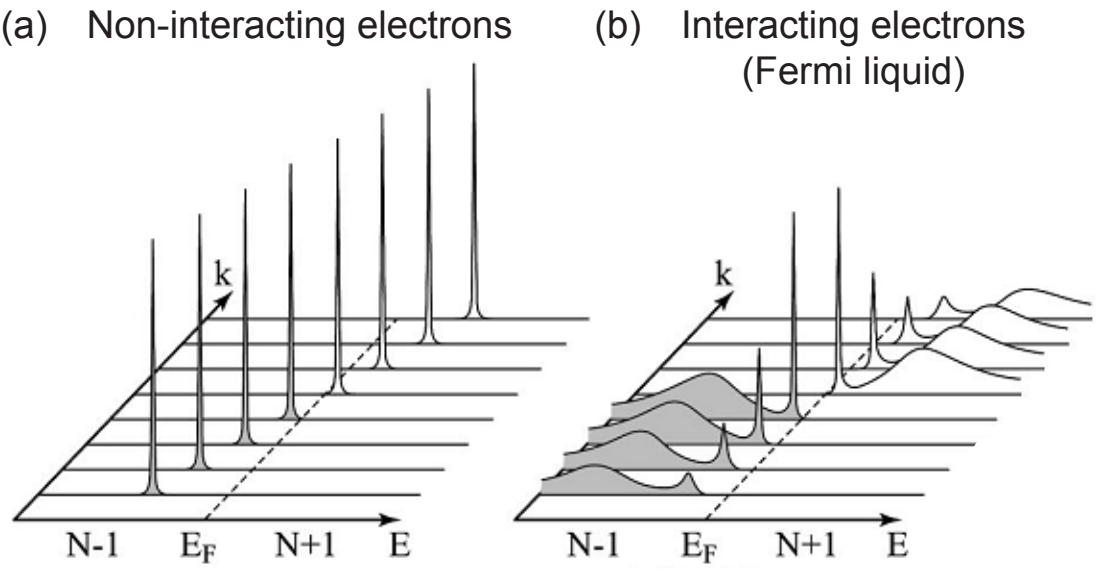

Figure 2.5: Expected spectral function for a parabolic band for the (a) non-interacting and the (b) interacting case. For the interacting case both the quasiparticle peak and the incoherent spectral weight can be seen. Adapted from [15]

about energy renormalization and the imaginary part about the lifetime of an electron with band energy $e_{\mathbf{k}}$ and momentum $\mathbf{k}$. In that case, Green's function and single particle spectral function can then be re-casted in terms of the electron self energy as[24]

$$G(\mathbf{k}, E) = \frac{1}{E - E_{\mathbf{k}} - \sum(\mathbf{k}, E)} \tag{2.17}$$

and

$$A(\mathbf{k}, E) = -\frac{1}{\pi} \frac{\sum''(\mathbf{k}, E)}{(E - E_{\mathbf{k}} - \sum(\mathbf{k}, E))^2 + \sum''(\mathbf{k}, E)^2} \tag{2.18}$$

A straightforward expectation from the above discussion is that in case of a non-interacting system, the spectral function would then be just made up of Dirac-delta functions that track the underlying bandstructure. But, for the interacting case the spectral function would develop an incoherent tail due to possible tran-

sitions into many different excited eigenstates corresponding to *(N-1)*-electron system as coefficients $c_m^{\mathbf{k}}$ for more than one m values are now non-zero as discussed earlier. Spectral function for both these cases is illustrated in Fig. 2.5. ARPES by providing direct experimental access to the single particle spectral function has emerged as an important spectroscopic tool to understand properties of correlated electron systems.

2.4 Experimental Considerations for ARPES

In this section we will describe key components that go into a typical ARPES setup and general requirements for performing successful experiments that are often demanding.

2.4.1 Light Sources

For performing photoemission experiments, a monochromatized high intensity light source is required to supply photons. Though experiments can be performed with photons both in the soft and hard x-ray regime, availability of photons with high resolving power that translates into much improved spectral bandwidth, often better than 1 meV has made ultra-violet photoemission an attractive and powerful tool. The results reported in this thesis has been obtained using a laboratory-based helium plasma lamp and at the "one-cube" ARPES endstation at beamline UE112 at the Berlin synchrotron (BESSY II). Some data has also been taken at now closed PGM ARPES endstation at the Synchrotron Research Center (SRC), Wisconsin Madison.

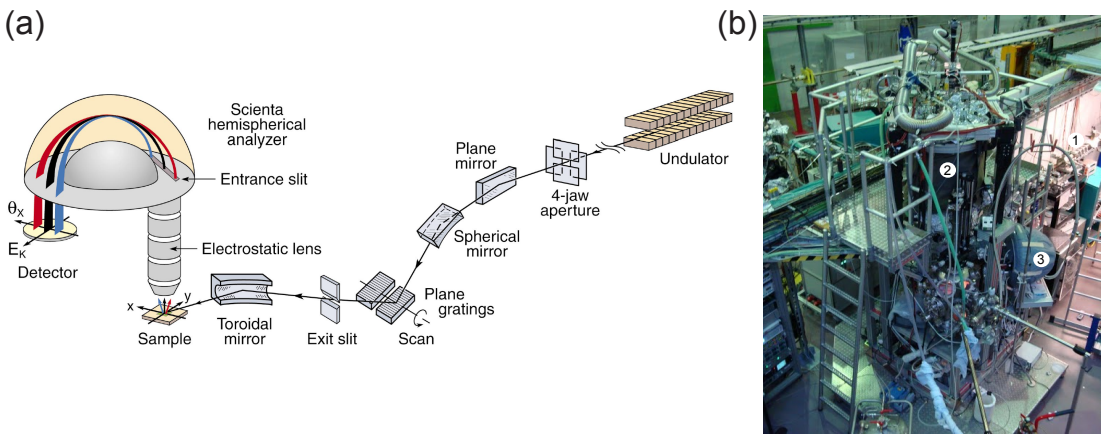

Figure 2.6: Synchrotrom ARPES (a)Schematic of an experimental photoemission set up at a synchrotron. Adapted from [15] (b) 1^3 ARPES end station at BESSY II. (1) shows the the beam path (2) shows the cryostat that enables sample temperature as low as 0.9 K (c) Scienta R4000 analyzer.

We use a VG Scienta VUV 5000 helium plasma lamp for lab based photoemission experiments described in this thesis. Microwaves generated by a microwave generator is fed into a small Helium filled cavity that can sustain a plasma of the gas emitting photons at characteristic frequencies associated with its atomic transitions. We generally use transitions at 21.2 eV (He Iα) and 40.8 eV (He IIα), as they are the brightest. We use a toroidal grating monochromator to isolate the characteristic transition lines and use a retractable glass capillary to direct the photon beam onto our sample that provides a spot size of $\approx$ 2mm. Due to high absorption of ultra-violet light the entire path from the lamp head into the chamber through the glass capillary is windowless. To minimize the background pressure in the chamber we use several narrow apertures along the beam path and differentially pump the entire line with three turbomolecular pumps in series. The narrow aperture of the glass capillary at the end also

provides high impedance on the gas load allowing us to maintain background pressure in the chamber of the order of 10^{-11} Torr while the microwave cavity is at 10^{-3} Torr pressure. Furthermore, we use ultra-high purity helium gas that is not expected to react strongly with the sample surface, thus not affecting sample lifetime in any significant manner. Measured integrated flux of our setup is $\approx 8.8\times10^{11}$ photons/sec at 21.2 eV and 3×10^{10} photons/sec at 40.8 eV

A major drawback of plasma lamps is that photon energy is not continuously tunable and is fixed at a discrete set of atomic lines. This disadvantage is mitigated by the ability to tune photon energies provided by synchrotrons. A schematic of a photoemission setup in a beamline is shown in Fig. 2.6 where highly polarized white light is produced by an undulator, then monochromatized and focussed on a sample. Different kinds of monochromator viz. PGM (Plane Grating Monochromator), SGM (Spherical Grating Monochromator), NIM (Normal Incidence Monochromator) are often employed at synchrotrons as per desired requirements that offer different advantages in terms of spectral range and spectral bandwidth. Another advantage of synchrotrons is easy tunability of light polarization that can help mitigate matrix element effects in certain situations as would be described in a later section.

2.4.2 Electron Analyzer

Perhaps the most complex instrumentation within an ARPES setup goes into making modern electron analyzers. In early days point-detectors were used and angle resolutions was achieved by moving either the sample or the detector. The major drawback in this approach was that at a given instant only a particular wavevector $\mathbf{k}$ was probed that led to long measurement times. In-

troduction of modern analyzers that uses electrostatic lenses to simultaneously detect electrons over a wide angular range using multiple angular channels has revolutionized the field by reducing detection times by more than two orders of magnitude. In our lab at Cornell and also at synchrotrons at BESSY and SRC we used a Scienta R4000 analyzer from VG Scienta capable of simultaneously recording 600 spectra over an angular spread of 30 degrees . A schematic of the analyzer is shown in Fig. 2.7. Once electrons enter into the analyzer nose cone, with analyzer in the *angle mode* electrostatic lenses physically separate electrons that came in at different emission angle and reduce their kinetic energy depending on the pass energy specified. Subsequently, the electrons after passing through an adjustable narrow slit enters into the hemispherical part of the spectrometer that consists of a positively charged inner hemisphere and a negatively charged outer hemisphere at an average radius of r. The bending radius of the electron's trajectory is determined by their kinetic energy so when they impinge on the detector they are spread along one axis according to their energy while they are already spread in the other axis by the lens system depending on their emission angle. The detector assembly comprises of a multi channel plate (MCP) that amplifies the photoelectron signal combined with a phosphor screen that is imaged by an out of vacuum CCD camera

In addition to the *angle mode*, where the analyzer multiplexes as a function of angle it can also operate in *transmission mode* multiplexing in real place providing a real space image of the emitted photoelectron intensity from the sample. This mode is very useful in identifying good spots on the sample.

The theoretical energy resolution of the detector depends on the pass energy

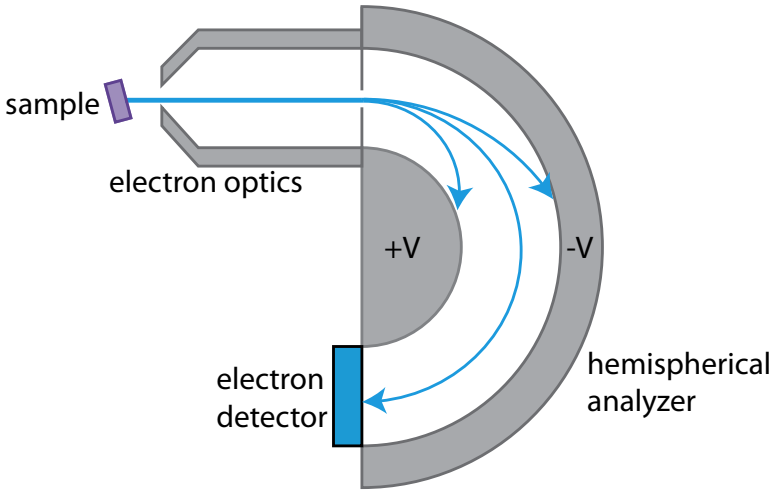

Figure 2.7: Schematic and working principle of a hemispherical analyzer. The electrons are accelerated and moves in an electric field created by a positively and negatively charged hemispheres. Only electrons of correct energy reaches the detector. Figure adapted from [19]

used and the entrance slit size which is given by

$$\Delta E \approx \frac{sE_p}{2r} \tag{2.19}$$

where s is the slit size, E_p is the pass energy of the analyzer and r is the average radius of the hemisphere. Scienta R4000 analyzers offers options to select slit widths from 0.1 - 2.0 mm and pass energies 1 - 200 eV and has an average hemisphere radius of 200 mm. Thus, the use of the smallest available slit size, s = 0.1mm results in a resolving power $\Delta E/E = 4000$, hence the name. This means theoretical best achievable energy resolution is 0.25 meV if one uses a pass energy of 1 eV and 0.1 mm slit. Of course, higher resolution comes at a cost of reduced spectral intensity as now less number of photoelectrons get into the detector. The overall instrumental resolution of our system is estimated by fitting the Fermi edge of a measured polycrystalline gold with the following function

$$I(E) = [(a + b(E - E_F)) \times f(E, T)] * G(E, \Delta E) + c \tag{2.20}$$

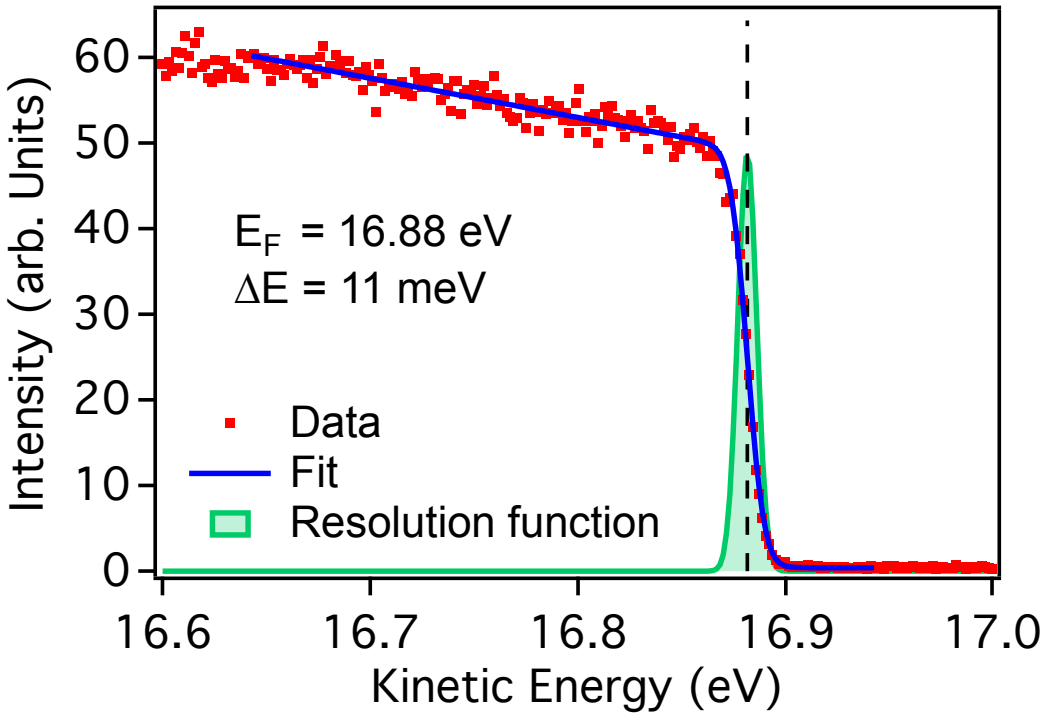

Figure 2.8: Fit to a Gold band edge by a functional form described in eqn. 2.20. Obtained resolution is given by the FWHM of the Gaussian shown in green.

which represents a linearly increasing density of states truncated by the Fermi-Dirac function f(E,T) and overall convolved with a Gaussian G, FWHM of which represents instrumental resolution. An example of a fit to a gold band edge is shown in Fig. 2.8

2.4.3 Sample Manipulator

Sample manipulator is an integral part of an ARPES system. There are primarily three considerations for designing a sample manipulator. It must hold the sample in place while providing access to the sample surface, cool down or heat

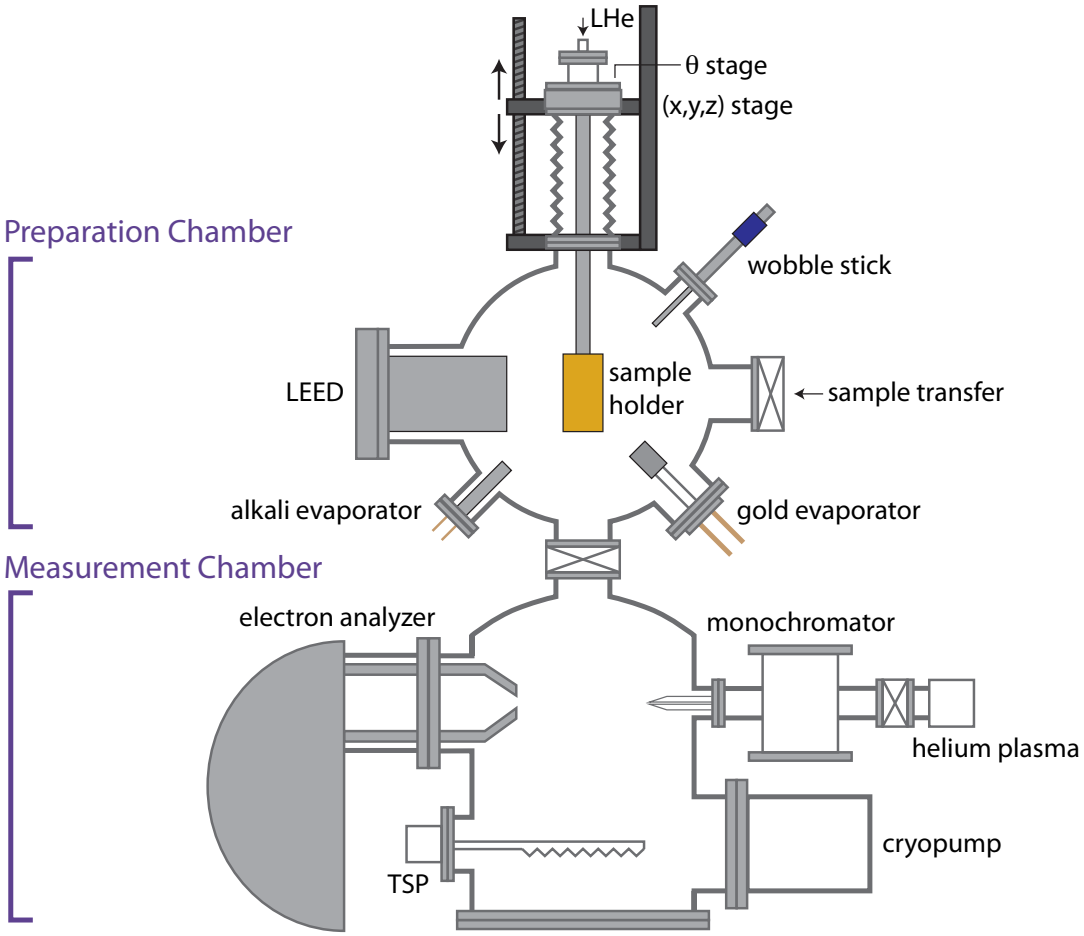

Figure 2.9: Dual chamber ARPES setup at Cornell University illustrating various components. Adapted from [19]

up the sample and move the sample around in vacuum so that a large area in the momentum space can be accessed. Large size of modern electron analyzers makes it increasingly prohibitive and clumsy to move them with any precision. Thus, in order to access a large momentum region a precise sample manipulator with a wide range of movement is the only option.

2.4.4 Maintaining Ultra high vacuum

As noted earlier ARPES being a surface sensitive technique requires ultra-clean surface that needs to be maintained throughout the measurement process. Even a sub-monolayer coverage can distort photoemission spectrum introducing serious artifacts in the measured data. At ambient pressure a monolayer can form on a sample surface almost instantaneously within a few nanoseconds. Thus, ARPES measurements needs to be performed under ultra-high vacuum conditions so as to be able to measure a sample with a pristine surface for an adequate amount of time. A rough idea of the vacuum requirement can be obtained estimating the time requirement for a monolayer formation at a given background pressure P. From the kinetic theory of gases, the rate of collision of gas molecules on the sample surface per unit area per unit time is given by

$$\frac{\delta N}{\delta A \delta t} = \frac{P}{\sqrt{2\pi MRT}} \tag{2.21}$$

where P is the gas pressure, M is the molecular weight of the gas, R is the universal gas constant, and T is temperature in Kelvin scale.[25] Assuming a sticking coefficient of 1, using the above equation one obtains monolayer formation time for a crystal with lattice constant 4Å, gas molecular weight $\approx$ 30 g/mol at room temperature to be 1 hour and 1 day for background pressures better than 5×10^{-10} torr and 2×10^{-11} torr, respectively. However, fortunately for most gases and material surfaces sticking coefficient is much lower than 1 that significantly relaxes the pressure requirement. Our ARPES chamber at Cornell uses a combination of turbo-molecular pumps, cryo pumps, ion pumps and sublimation pumps that are all *dry pumps* reducing exposure of our system to contaminants and achieves a background pressure of better than 4×10^{-11} torr. A schematic of the ARPES setup is shown in Fig. 2.9

2.5 Interpretation and Analysis of ARPES spectra

2.5.1 Energy and Momentum Distribution Curves

In a typical ARPES experiment with the use of multiplexing lenses it is possible to collect electrons ejected at different emission angles simultaneously that can be used to generate energy-momentum maps as shown in Fig. **??**. While these maps are extremely useful to understand overall electronic structure, often times quantitative analysis is done by slicing these images into one-dimensional plots representing energy dependence of the spectral weight at a fixed momentum (Energy Distribution Curves - EDC) or plots representing momentum dependence of the spectral weight at a fixed energy (Momentum Distribution Curves - MDC). Energy and Momentum Distribution Curves thus obtained can be analyzed using analytical expressions derived from the spectral function formula in eqn. 2.18. For energy values ω near the pole energy $E^*_{\mathbf{k}} = \epsilon_{\mathbf{k}} - \sum'(\mathbf{k}, E^*_{\mathbf{k}})$, real part of the self energy can be written using Taylor expansion as

$$\omega - \epsilon_{\mathbf{k}} - \Sigma'(\mathbf{k}, \omega) \approx \frac{1}{z_{\mathbf{k}}}(\omega - E^*_{\mathbf{k}}) \tag{2.22}$$

where $z^{-1}_{\mathbf{k}} \approx 1 - \delta_\omega \sum'(\mathbf{k}, \omega)|_{\omega = E^*_{\mathbf{k}}}$ Then, the spectral function at $\mathbf{k}$ becomes

$$\mathcal{A}(\mathbf{k}, \omega) = z_{\mathbf{k}} \frac{\Gamma_{\mathbf{k}}/\pi}{(\omega - E^*_{\mathbf{k}})^2 + \Gamma^2_{\mathbf{k}}} + \mathcal{A}_{incoh} \tag{2.23}$$

where $\Gamma_{\mathbf{k}} = z_{\mathbf{k}}|\sum''(\mathbf{k}, E^*_{\mathbf{k}})|$ Thus, from eqn. 5.6 Energy Distribution Curves (EDCs) can be analyzed using a lorentzian lineshape with integrated spectral weight $z_{\mathbf{k}}$ known as quasiparticle residue and linewidth $\Gamma_{\mathbf{k}}$ representing quasiparticle lifetime together respresenting the coherent part of the spectral function. The non-lorentzian contribution due to correlation effects is encapsulated in the incoherent spectrak weight $\mathcal{A}_{incoh}$ On the other hand for analyzing Momentum

Distribution Curves, particularly near the Fermi level for a fairly wide band linear approximation for the electronic dispersion $\epsilon_{\mathbf{k}} = v_F \cdot (k - k_F)$ is quite accurate when the spectral function becomes

$$\mathcal{A}(k,\omega) = -\frac{1}{\pi}\frac{\Sigma^{''}(k,\omega)/v_F^2}{[k - k_F - (\omega - \Sigma^{'}(k,\omega)/v_F]^2 + [\Sigma^{''}(k,\omega)/v_F]^2} \tag{2.24}$$

where v_F is the Fermi velocity Thus, under the above assumptions MDCs for a given ω has a Lorentzian lineshape centered at

$$k_m = k_F + (\omega - \Sigma^{'}(k,\omega))/v_F \tag{2.25}$$

with full width at half-maximum given by

$$\Delta(k) = 2|\Sigma^{''}(k,\omega)/v_F| \tag{2.26}$$

The above equations can be solved to obtain an estimate of the self energy

$$\Sigma(\mathbf{k},\omega) = \Sigma^{'}(\mathbf{k},\omega) + \iota\Sigma^{''}(\mathbf{k},\omega) = \omega - v_F \cdot (k_m - k_F) + \iota|v_F \cdot \Delta(k)/2| \tag{2.27}$$

Though linear approximation is used in most of the cases for analysis of ARPES data, it is also possible to use a quadratic approximation in appropriate cases to derive equations similar to eqns. 2.25,2.26 and 2.27[26]

2.5.2 Background Estimation and Matrix Element Effects

Though ARPES directly access the single particle spectral function, actual measured intensity can be modulated by the matrix element effect $|M_{\mathbf{k}}|^2$ (eqn. 2.16), inelastically scattered electron and finite energy and momentum resolution of the experimental setup. ARPES intensity is thus modelled as

$$I(\mathbf{k},\omega) = \int d\tilde{\omega} d\tilde{\mathbf{k}} I_0(\tilde{\mathbf{k}}, \nu, \mathbf{A}) f(\tilde{\omega}) A(\tilde{\mathbf{k}}, \tilde{\omega}) R(\omega - \tilde{\omega}) Q(\mathbf{k} - \tilde{\mathbf{k}}) + B \tag{2.28}$$

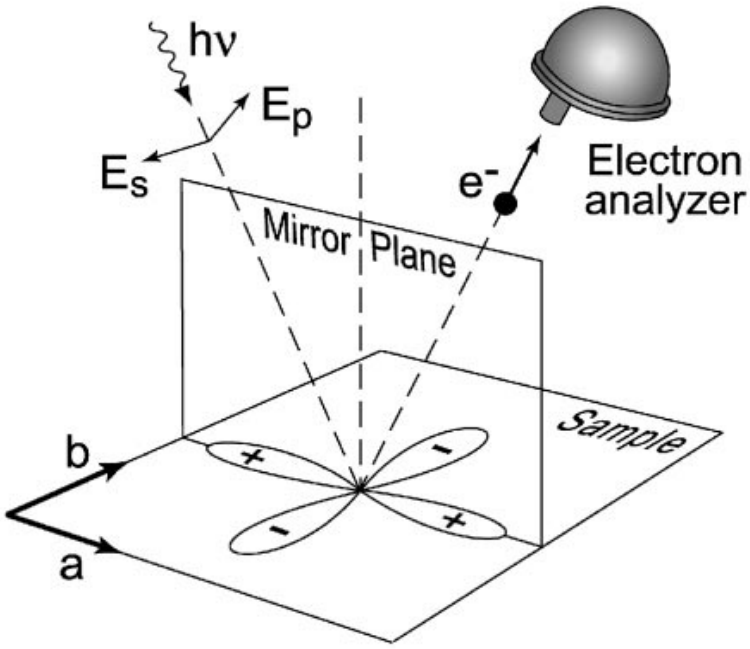

Figure 2.10: Illustration showing a sample geometry used to explain matrix element effects in the photoemission process, as described in the text. Figure adapted from [15]

where R and Q are the energy and momentum resolution functions typically modelled as a Gaussian. B represents the background function accounting for inelastically scattered electrons and also contributions from higher order light for synchrotron measurements. Inelastically scattered electrons is generally modelled using a Shirley function $B_{Shirley} \propto \int_{\omega}^{\mu} d\omega' P(\omega')$ where $P(\omega)$ that allows extraction of elastically scattered contribution from the measured photocurrent intensity $I(\omega) = P(\omega) + c_{Shirley} B_{Shirley}$, $c_{Shirley}$ being the free parameter obtained from fits.[27]

The term $I_0(\tilde{\mathbf{k}}, \nu, \mathbf{A})$ in eqn. 2.28 is proportional to $|M_{\mathbf{k}}|^2$ magnitude of which can be influenced by incident photon energy, initial and final states involved in the photoemission process and the experimental geometry. Because quanti-

tative estimation of the matrix elements in photoemission experiments is extremely complicated this is considered a nuisance in ARPES data analysis. However, if used properly this can provide valuable information about wavefunction from symmetry and parity arguments. By using, commutation relation $\hbar\mathbf{p}/m = -\iota[\mathbf{x}, H]$, matrix elements can be written as

$$|M_{fi}^{\mathbf{k}}|^2 \propto |\langle \phi_f^{\mathbf{k}} | \epsilon \cdot \mathbf{x} | \phi_i^{\mathbf{k}} \rangle|^2 \tag{2.29}$$

where ϵ is the unit vector along the vector potential $\mathbf{A}$ of the incident light. In an experimental geometry shown in Fig.2.10 where the experimental geometry acts as a mirror plane, as the final state has to be even about the mirror plane so as not to vanish at the detector, it implies $(\epsilon \cdot \mathbf{x})|\phi_i^{\mathbf{k}}\rangle$ also has to be even. For initial state wave function with even symmetry as in $d_{x^2-y^2}$ orbitals, photoemission process is symmetry allowed for the polarization vector ϵ to be either even or in-plane and vanish for it being odd or out of plane. For a generic situation this can be summarized as

$$\langle \phi_f^{\mathbf{k}} | \mathbf{A} \cdot \mathbf{p} | \phi_i^{\mathbf{k}} \rangle \begin{cases} \phi_i^{\mathbf{k}} \; even \; \langle + | + | + \rangle \;\; \Rightarrow \;\; \mathbf{A} \; even \\ \phi_i^{\mathbf{k}} \; odd \; \langle + | - | - \rangle \;\; \Rightarrow \;\; \mathbf{A} \; odd \end{cases} \tag{2.30}$$

CHAPTER 3

THE KONDO LATTICE: HEAVY FERMIONS AND MIXED VALENCE

3.1 Introduction

The term *'Kondo Lattice'* describes a class of inter-metallic compounds that contain certain rare earth elements (e.g. Ce, U, Yb etc.) with a partially filled f shell in a periodic arrangement (*lattice*), where strong interaction between the localized spin moments at the rare earth sites and the delocalized electrons (*Kondo effect*) brings about a profound alteration in their physical properties.[28, 29] Since early 1970s, when they were first identified, a great many materials have been discovered that are classified as Kondo lattice systems often hosting exciting emergent ground states such as heavy Fermi liquid[30, 31, 32], unconventional superconductivity[33, 34, 35, 36, 37, 38, 39], hidden order[40, 41] etc. Often, these ground states can further be tuned by modest perturbations using magnetic field and pressure, thereby providing experimental access to quantum phase transitions.[42, 43, 44]

The common theme that unites all these materials is the emergence of carriers with very high effective mass that can be even two or three orders of magnitude *heavier* than in conventional metals.[28] Within Landau's Fermi liquid framework linear specific heat coefficient that encapsulates electronic contribution to specific heat is directly proportional to the quasiparticle density of states and therefore, to its effective mass.[45]

$$\gamma = \frac{\pi^2 k_B^2}{3}\rho^* = \frac{k_F k_B^2}{3\hbar^2}m^* \tag{3.1}$$

for a band with quadratic dispersion, $E_{\mathbf{k}} = \hbar^2 k^2/2m^*$

While, in conventional metals linear specific heat coefficient varies between 1 - 10 mJ /molK^2 (for example, silver (Ag) - 1, sopper (Cu) - 1.39, rubidium (Rb) - 1.22, lithium (Li) - 2.17; all in units of mJ /molK^2), for Kondo lattice systems this can be orders of magnitude higher[28] as is shown in Fig. 3.1. This provides an indication of the *heaviness* of the charge carriers in these materials and hence, are known as *heavy fermions*. Though technically, materials are strictly in the *heavy fermion* regime, when all charge fluctuations have been frozen out and only spin degrees of freedom survive. However, in many compounds with similar enhanced carrier effective mass such as $YbAl_3$, SmB_6 etc., valence fluctuations survive even at the lowest temperatures. In such situations the rare earth valence valence fluctuates between two almost degenerate valence configurations leading to an average non-integral rare earth valence and are known as *mixed-valence systems*.[47]

The underlying mechanism primarily responsible responsible for interesting exotic properties in these materials is the remarkable quantum interaction known as the *Kondo Effect*. It describes the mechanism by which free magnetic moments at high temperatures gets quenched by the conduction electron spins in the Fermi sea forming singlet scattering centers at temperatures below a characteristic temperature known as the Kondo temperature T_K. When this happens in materials with a lattice of spin moments, the very same interaction results in dissolution of spins into the conduction sea leading to emergent quasiparticles with radically enhanced effective mass.[46] In the following sections we will discuss the Kondo effect in isolation and also its impact when occurring in crystals with an ordered array of spin moments.

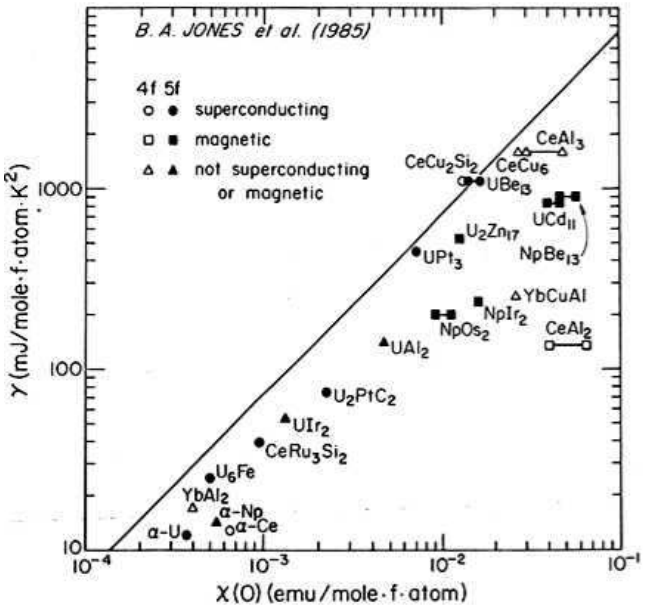

Figure 3.1: Linear specific heat coefficient (γ) for different materials belonging to the *Kondo Lattice* family that can be orders of magnitude higher than normal metals indicating *heaviness* of their carriers. It is plotted against magnetic susceptibility (χ) to highlight scaling relation (Wilson' ratio, w = χ/γ)[59] observed in Kondo lattice systems that takes a constant value of ≈ 2 for many compounds. Adapted from [46]

3.2 The Kondo Effect

3.2.1 Formation of Local Moments

Signatures of the Kondo effect was first identified by de Haas *et. al.*[48] in early 1930s at Leiden when they identified an upturn in resistivity at low temperatures in many simple metals including copper, silver, gold etc. About three decades later this was linked to the presence of magnetic impurities in those metals.[49, 50] In particular, in 1962, Clogston, Mathias and co-workers at Bell Labs showed that the resistivity response of magnetic iron impurities in Nio-

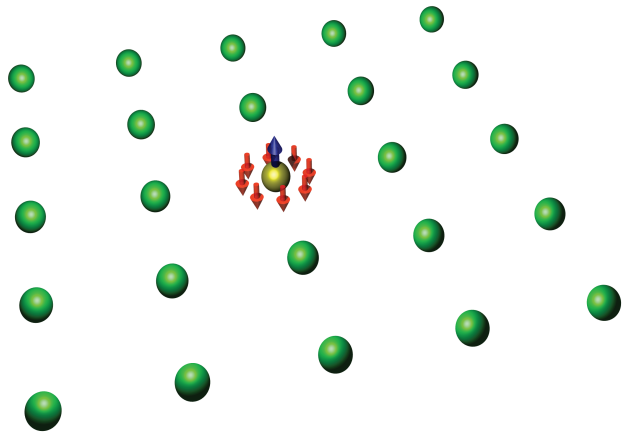

Figure 3.2: Illustration of a magnetic impurity (in yellow) in a metallic host. *Figure Courtesy: M. H. hamidian*

bium can be tuned by alloying it with Molybdenum, as illustrated in Fig. 3.3 a).[49]

An explanation of this phenomenon had its origins in a microscopic model proposed by Anderson,[52] known as Single Impurity Anderson Model where he recognized the importance of on-site Coulomb repulsion U for the survival of magnetic moments in the Fermi sea and can be written as

$$H = \sum_{\mathbf{k},\sigma} \epsilon_{\mathbf{k}} n_{\mathbf{k},\sigma} + \epsilon_f n_f + \sum_{\mathbf{k},\sigma} V(\mathbf{k})[c^{\dagger}_{\mathbf{k}\sigma} f_{\sigma} + f^{\dagger}_{\sigma} c_{\mathbf{k}\sigma}] + U n_{f\uparrow} n_{f\downarrow} \tag{3.2}$$

where the first two terms describe delocalized conduction electrons and energy states of the impurity ion, respectively. The third term captures the hybridization process between the local moment and the conduction electrons and finally, the last term is due to the strong coulomb repulsion at the impurity site.

For an impurity ion in the atomic limit (neglecting the hybridization term)

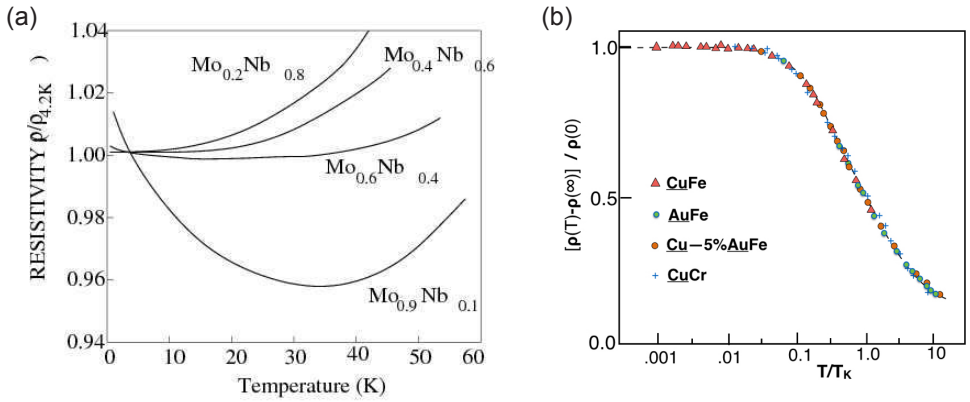

Figure 3.3: Experimental signatures of the Kondo Effect. a) Evolution of the low temperature *"resistivity upturn"* with increasing Molybdenum content in a molybdenum-niobium (Mo-Nb) alloy. Adapted from [50] (b) Universal scaling behavior observed in Kondo impurities from which the energy scale of the Kondo problem can be identified, given by the Kondo temperature (T_K). Adapted from [51]

to be in a magnetic state it needs to be in a doublet ground state, where the f orbitals are singly occupied $|f^1,\uparrow\rangle$ and $|f^1,\downarrow\rangle$. Furthermore, charge fluctuations into a doubly-occupied $|f^2\rangle$ or a non-occupied $|f^0\rangle$ state should be energetically prohibitive that gives us the following condition

$$U/2 > |\epsilon_f + U/2| \tag{3.3}$$

On the other hand in the opposite limit including the hybridization term and neglecting Coulomb repulsion U, f electrons are expected to form a resonance[53] as they hybridize with the conduction electrons with a resonance width

$$\Delta = \pi V^2 \rho \tag{3.4}$$

where V^2 is the average hybridization strength and ρ is the density of states of the conduction electrons at the Fermi level (Fig. 3.4).

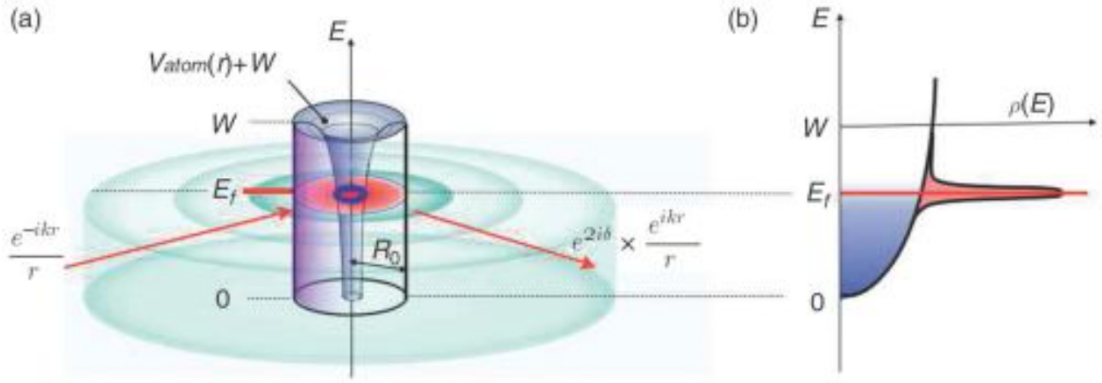

Figure 3.4: a)Illustration of an electron in an impurity potential interacting with the conduction sea b) Virtual hopping processes involving the impurity electron gives rise to an impurity resonance seen as a peak in the density of states, sometimes known as Anderson-Friedel resonance. Adapted from [54]

In presence of both the competing terms in the microscopic hamiltonian describing the system, Anderson showed a mean-field treatment provides the following condition for the survival of local moments[52]

$$U > U_c \approx \pi\Delta \tag{3.5}$$

The above condition explains experimentally observed(Fig. 3.3 a)) local moment formation of iron impurities with increased alloying of niobium (Nb) with molybdenum (Mo). As molybdenum has a smaller value of Δ compared to niobium, molybdenum content in niobium - molybdenum alloy beyond a critical Mo concentration satisfies eqn. 3.5 leading to resistivity upturn characteristic of local moments.

In the regime where the local moment is stabilized virtual charge fluctuations leads to an effective super-exchange in the spin channel that leads to an antiferromagnetic coupling between the local spin moments and the spin density of

the delocalized states that can be written as[55, 56]

$$H_I = J\psi^\dagger \sigma \psi \cdot S_f \tag{3.6}$$

It was a third order perturbative expansion of this term that led Jun Kondo to predict a scattering rate $(1/\tau)$ of electrons that grew logarithmically at low temperatures[57, 58] thus, finally providing an explanation for 'resistivity upturn' observed in experiments.

$$\frac{1}{\tau} = [J\rho + 2(J\rho)^2 ln\frac{D}{T}]^2 \tag{3.7}$$

where D is the band width and ρ is the density of states of the conduction electrons. This also gives a temperature scale of the physical process, the Kondo temperature T_K

$$T_K = De^{-1/(2J\rho)} \tag{3.8}$$

below which the perturbation approach breaks down as the corrections become as large as the original contribution itself. It was development of renormalized group approach at Cornell by Ken Wilson that provided a first unified description of the Kondo effect both at high(weak coupling) and low(strong coupling) temperature limits.[59]

Salient properties of Kondo effects can be summarized as

1) Localized moments showing Curie-Weiss susceptibility $\chi = 1/T$ at high temperatures form screened Kondo singlets at low temperatures that exhibit paramagnetic susceptibility $\chi = 1/T_K$

2) A free spin S=1/2 moment has a spin entropy of $Rln2$ per mole. At low temperatures as the spin moment can be thought to get entangled with conduction electrons forming local singlets the spin entropy is lost and accordingly lzero temperature specific heat coefficient is given by $\gamma = \frac{C_V}{T}(T \to 0) \approx Rln2/T_K$

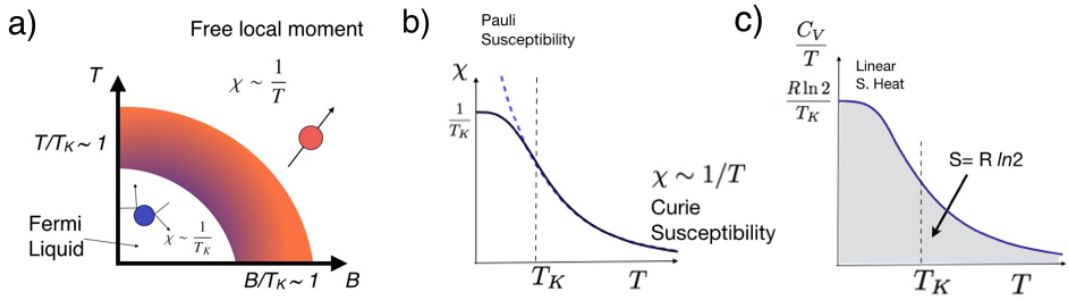

Figure 3.5: Influence of the Kondo interaction on the physical properties. a) A temperatue-field phase diagram is shown, where at temperatures and fields smaller compared to the Kondo temperature T_K, the local moment is screened by the conduction electrons b) As a result, at temperatures above T_K the material exhibits a Curie-Weiss susceptibility as expected from the presence of free moments which gradually crosses over to a Pauli paramagnetic behavior as the moments get screened at low temperatures c) Enhanced Kondo screening forms local spin singlets. As a result the material loses spin entropy associated with the free moment, which for a spin 1/2 system is of the order of Rln2. As the crossover width is of the order of T_K, zero temperature specific heat coefficient should be $\approx$ Rln2/T_K. Adapted from [60]

3)T_K is the only energy scale in the problem. Accordingly, resistivity that displays contributions from scattering of electrons off local moments show a scaling behavior. (Fig. 3.3 b))

4)The Kondo effect also profoundly alters f electron spectral function. Scattering off the Kondo singlets gives rise to the so-called Abrikosov-Suhl resonance or Kondo resonance which is resonantly confined at thhe Fermi level with the resonance width being determined by the Kondo temperature (T_K)

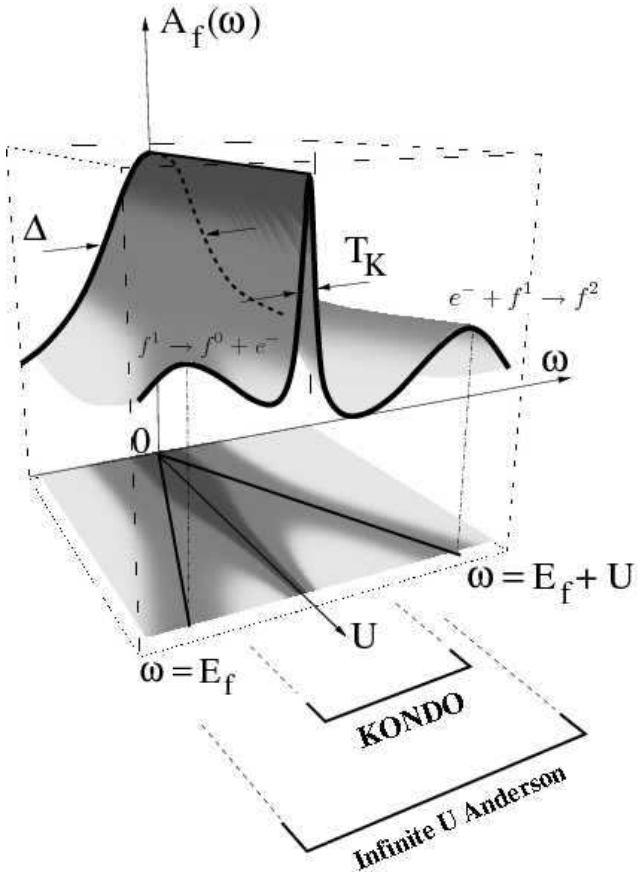

Figure 3.6: Illustration of Abrikosov-Suhl/Kondo Resonance. It can be understood as arising out of Anderson-Friedel resonance in the non0-interacting limit under an adiabatic evolution on addition of strong on-site correlations U. Most of the spectral weight is transferred to the upper and the lower Hubbard band resulting in a sharp resonance pinned at the Fermi level. Adapted from [46]

3.2.2 The Kondo Resonance

In this section we will discuss the Kondo resonance [61, 62], a truly remarkable many-body manifestation of the Kondo effect in a little more detail particularly because, ARPES, the primary experimental technique used in this thesis can directly visualize its emergence.

One way to understand is emergence is by using the adiabatic approach, where starting from the non-interacting limit strong correlations encapsulated in on-site Coulomb repulsion is gradually turned on. In the non-interacting limit, magnetic ion within an environment of itinerant carriers can create virtual bound states leading to a Friedel-Anderson resonance.[53] The localized f electrons can tunnel out of their core and hybridize with the Bloch states resulting in a broadening in their density of states that is given by the resonance width described in eqn. 3.4 and is illustrated in Fig. 3.4.

An easy way to understand the effect of interaction is to study the evolution of the f electron spectral function as described in the previous chapter

$$A_f(\omega) = \frac{1}{\pi} Im G_f(\omega + \iota\eta) \tag{3.9}$$

where, the f charge of the ion is determined by the integrated spectral weight below the Fermi level

$$\langle n_f \rangle = 2 \int_{-\infty}^{0} d\omega A_f(\omega) \tag{3.10}$$

Fig. 3.6 shows how f electron spectra function when the interactions (U) is adiabatically added. The f electron spectral function in the non-interacting limit consists of a Lorentzian resonance peak of width Δ. Adding interaction, while paying attention to maintain the correct occupancy of the f states results in the appearance of three peaks in the spectral function, where the two peaks associated with valence fluctuations are at at energies $\omega = \epsilon_f$ and $\omega = \epsilon_f + U$. And there is a central peak which we will call the *Kondo Resonance* peak associated with spin fluctuations of singly occupied f orbital. Such three peak struc-

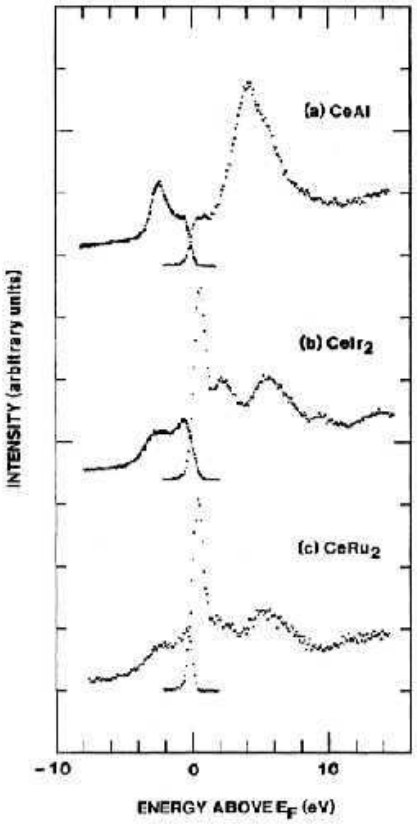

Figure 3.7: Measured one electron removal and one electron addition spectral function of Ce intermetallic compounds containing partially filled 4*f* shell using x-ray photoemission spectroscopy (XPS). Three peak structure can be identified as expected from theory. CeAl is antiferromagnetic and does not show a Kondo resonance peak. Adapted from [63]

ture (Fig.3.7) has been observed by a combination of photoemission and inverse photoemission[63, 64], that directly access single particle spectral function providing some evidence for the theory.

Due to the adiabatic invariance of the f spectral weight at the Fermi level determined by the scattering phase shift δ_f[65, 66], survival of the Kondo resonance peak is guaranteed even in the regime when $U \geqslant \Delta$. However, the total spectral weight $\int_{-\infty}^{\infty} A_f(\omega) = 1$ is also conserved and in the large U limit most of the spectral weight is expected to get transferred into the lower and upper

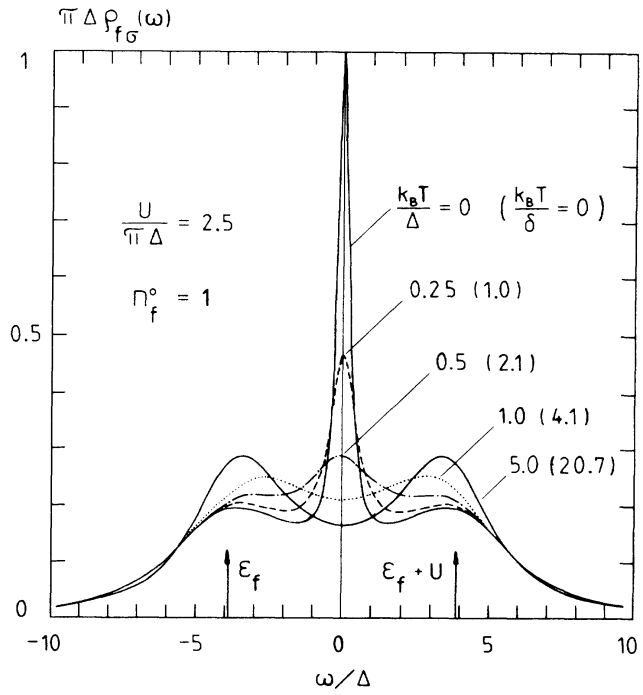

Figure 3.8: Evolution of Kondo resonance peak with temperature as calculated within a single impurity Anderson model (SIAM) for the particle-hole symmetric case. Adapted from [67]

Hubbard bands.Thus, a small residual spectral weight $z \leqslant 1$ remains under the Kondo resonance peak. As the height of the spectral peak is fixed at $\approx 1/\Delta$, to maintain constancy of spectral weight resonance width must be of the order of $z\Delta$ where the scale is set by the Kondo temperature $T_K \approx z\Delta$. A detailed calculation of the spectral weight within Single Impurity Anderson model provides a quantitative evolution of the Kondo resonance peak as is shown in Fig. 3.8 for the particle-hole symmetric case.[67]

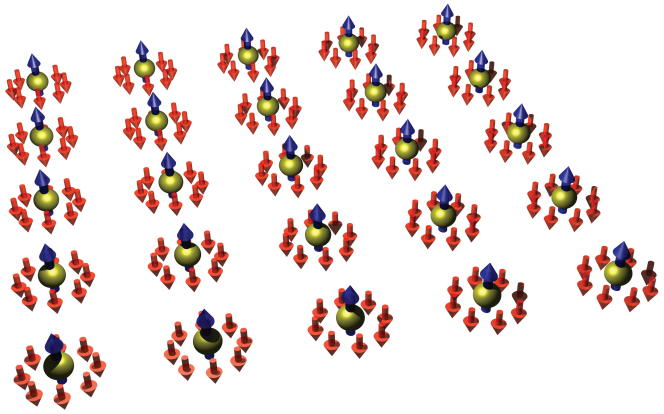

Figure 3.9: Illustration of a Kondo lattice system. Such a system can though to have local spin moments at each lattice sites. *Courtesy M.H. Hamidian*

3.3 The Kondo Lattice

3.3.1 Doniach's Phase Diagram

Discovery of rare-earth intermetallic compounds containing partially filled f shell with very high effective mass prompted Doniach to propose an extension of the Kondo effect to explain their electronic and magnetic properties.[68] He envisaged that in these materials Kondo effect is occurring at each of the rare earth lattice sites that contain localized spin moments. Such a *Kondo Lattice* has two novel features absent in the single impurity case discussed in the previous section.

Because of the additional translation symmetry due to the lattice the elastic scattering off Kondo singlets can now conserve momentum and can lead to emergence of coherence that should result in a rapid decrease of resistivity.

This can be explicitly seen in resistivity measurements of La doped $CeCu_6$

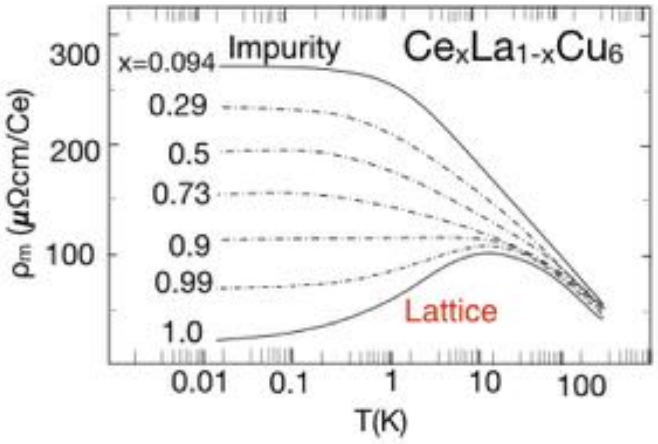

Figure 3.10: Evolution of low temperature resistivity from dilute impurity limit to the Kondo lattice limit highlighting the importance of additional translational symmetry in Kondo lattice. Scattering at individual lattice sites can develop coherence for the Kondo lattice case leading to dramatic drop in low temperature resistivity. Adapted from [30]

where cerium (Ce) contains one electron in its f shell that acts a spin moment localized at the Ce sites. Lanthanum (La) is iso-electronic to Ce, but for the occupation of the f shell which is empty in this case. Thus in the limit when most of the Ce atroms are replaced by La it can be thought of as the dilute impurity Kondo limit, whereas in the other limit $CeCu_6$, with no La atoms is a Kondo lattice. As is shown in Fig. 3.10, as the system goes towards the Kondo limit with decreasing La concentration resistivity starts to develop a coherence maxima and at low temperatures drops to very low values exhibiting a T^2 Fermi Liquid behavior.[30]

Additionally, the local moments at different rare-earth sites can now interact with each other through the induced spin-polarization of the conduction electrons around them.[69, 70, 71] Sharp discontinuity in occupation of the conduction electrons determined by the Fermi energy (E_F) gives rise to what is called Friedel oscillations in their induced spin density that decay as

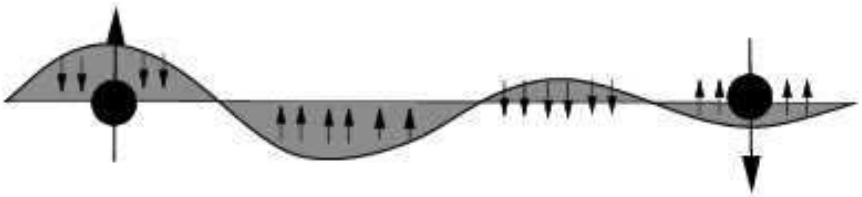

Figure 3.11: Illustration showing RKKY interaction between two adjacent spin moments due to local polarization of the conduction electrons near the spin moments. RKKY interaction between the spin moments is another novelty of the Kondo lattice compared to the dilute impurity limit.

$$\langle \sigma(\mathbf{r}) \rangle = -J\rho \frac{cos2k_F r}{|k_F r|^3} \tag{3.11}$$

This results in a net anti-ferromagnetic RKKY type interaction between two localized spin moments

$$J_{RKKY}(r) = -J^2\rho \frac{cos2k_F r}{k_F r} \tag{3.12}$$

Thus, Doniach proposed that there are two energy scale in the Kondo lattice problem, the single ion Kondo temperature T_K and T_{RKKY}, given by

$$T_K = De^{-\frac{1}{(2J\rho)}} \tag{3.13}$$

$$T_{RKKY} = J^2\rho \tag{3.14}$$

It is then possible to draw a universal phase diagram for Kondo lattice systems as proposed by Doniach, shown in Fig. 3.12 where, when $J\rho$ is small T_{RKKY} is the dominant energy scale and the ground state is expected to be antiferromagnetic. While, when $J\rho$ is large T_K becomes the dominant energy scale melting the long range magnetic order and stabilizing a many body Kondo ground state. When the two energy scales become comparable it could even be possible to stabilize a quantum critical ground state.

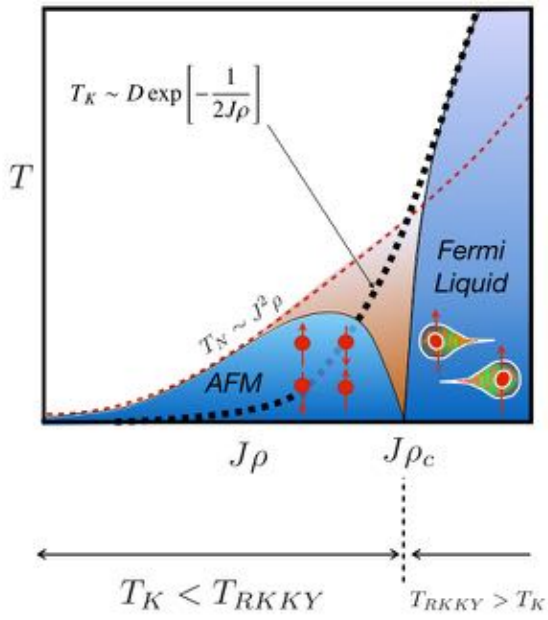

Figure 3.12: Phase diagram of a Kondo lattice system as drawn by Doniach in presence of both Kondo and RKKY interaction. Adapted from [60]

3.3.2 Emergence of hybridized *heavy* bands

In light of the above discussion the Kondo lattice as proposed by Doniach can then be thought of as the limiting case of a lattice extension of the Anderson impurity model known as the Periodic Anderson Model. Very simply the hamiltonian can be written as[28]

$$H_{PAM} = \sum_{i,\sigma} \epsilon_f f^\dagger_{i,\sigma} f_{i,\sigma} + U \sum_i f^\dagger_{i,\uparrow} f_{i,\uparrow} f^\dagger_{i,\downarrow} f_{i,\downarrow} + \sum_{\mathbf{k},\sigma} \epsilon_{\mathbf{k}} c^\dagger_{\mathbf{k},\sigma} c_{\mathbf{k},\sigma} + \sum_{i,\mathbf{k},\sigma} (V_{\mathbf{k}} e^{-i\mathbf{k}\cdot\mathbf{R_i}} f^\dagger_{i,\sigma} c_{i,\sigma} + V^*_{\mathbf{k}} e^{i\mathbf{k}\cdot\mathbf{R_i}} c^\dagger_{i,\sigma} f_{i,\sigma}) \tag{3.15}$$

where the first two terms describe localized f electrons, next term describe delocalized Bloch states and the last term encapsulates the hybridization between the two. As we are in a lattice, the hybridization term $V_{\mathbf{k}}$ is multiplied by a phase factor $e^{i\mathbf{k}.\mathbf{R_i}}$ where $\mathbf{R_i}$ is the position vector of the lattice site i

To understand the implication of the model we will use effective Hartree-Fock formalism to construct single particle Green's function which can be written in the energy - momentum space as

$$\begin{bmatrix} \omega - \mu - \epsilon_{f,\mathbf{k}} - \sum_{\sigma}(\omega, \mathbf{k}) & -V_{\mathbf{k}} \\ -V_{\mathbf{k}} & \omega - \epsilon_{\mathbf{k}} \end{bmatrix} \begin{bmatrix} G^{ff}_{\mathbf{k},\sigma} & G^{cf}_{\mathbf{k},\sigma} \\ G^{fc}_{\mathbf{k},\sigma} & G^{cc}_{\mathbf{k},\sigma} \end{bmatrix} = I \tag{3.16}$$

that follows from a diagrammatic expansion in powers of the Coulomb interaction U and the hybridization $V_{\mathbf{k}}$. μ is the chemical potential, $\epsilon^{f}_{\mathbf{k}}$ is the unrenormalized energy level of the f state and $\sum_{\sigma}(\omega, \mathbf{k})$ is the proper self-energy capturing two-body interaction between the f states. The self-energy is zero for U = 0, when the Green's function for the f and c electrons can be written as

$$G^{ff}_{\mathbf{k},\sigma}(\omega) = \frac{1}{\omega - \mu - \epsilon_{f,\mathbf{k}} - |V_{\mathbf{k}}|^2|/(\omega - \epsilon_{\mathbf{k}})} \tag{3.17}$$

$$G^{cc}_{\mathbf{k},\sigma}(\omega) = \frac{1}{\omega - \epsilon_{\mathbf{k}} - |V_{\mathbf{k}}|^2|/(\omega - \mu - \epsilon_{f,\mathbf{k}})} \tag{3.18}$$

We can add the effect of correlations for cases with finite U through the self-energy term. We can expand $\sum(\omega, \mathbf{k})$ in a Taylor's series about a point on the Fermi surface with $\omega = \mu$ and $\mathbf{k} = \mathbf{k_F}$ and write it as

$$\sum(\omega, \mathbf{k}) = \sum^{'}(\mu, \mathbf{k}_F) + (\mathbf{k} - \mathbf{k}_F) \cdot \nabla \sum^{'}(\mu, \mathbf{k})_{k=\mathbf{k_F}} + (\omega - \mu)(\frac{\delta \sum^{'}(\omega, \mathbf{k}_F)}{\delta\omega})_{\omega=\mu} + ... \tag{3.19}$$

Following results due to Luttinger we assume $\sum^{''}(\omega, \mathbf{k}_F) \approx (\omega - \epsilon_F)^2$ in regions around the Fermi surface. Neglecting second order terms in $(\omega - \mu)$ and $(\mathbf{k} - \mathbf{k}_F)$ we can define renormalized Green's function

$$\tilde{G}^{ff}_{\mathbf{k},\sigma}(\omega) = \frac{1}{\omega - \mu - \tilde{\epsilon}_{f,\mathbf{k}} - |\tilde{V}_{\mathbf{k}}|^2|/(\omega - \epsilon_{\mathbf{k}})} \tag{3.20}$$

$$\tilde{G}^{cc}_{\mathbf{k},\sigma}(\omega) = \frac{1}{\omega - \epsilon_{\mathbf{k}} - |_{\mathbf{k}}|^2|/(\omega - \mu - \tilde{\epsilon}_{f,\mathbf{k}})} \tag{3.21}$$

Thus, the result of addition of interaction is that near the chemical potential $G^{ff}_{\mathbf{k},\sigma}(\omega) = z_{\mathbf{k}_F}\tilde{G}^{ff}_{\mathbf{k},\sigma}(\omega)$ while $G^{cc}_{\mathbf{k},\sigma}(\omega) = \tilde{G}^{cc}_{\mathbf{k},\sigma}(\omega)$. Now, the renormalized f level

energy can be written as

$$\tilde{\epsilon}_{f,\mathbf{k}} = z_{\mathbf{k}_F}(\epsilon_f - \mu + \sum(\mu, \mathbf{k}_F) + (\mathbf{k} - \mathbf{k}_F) \cdot \nabla \sum^{'}(\mu, \mathbf{k}_f)) \tag{3.22}$$

where

$$z_{\mathbf{k_F}} = (1 - (\frac{\delta \sum^{'}(\omega, \mathbf{k}_F)}{\delta\omega})_{\omega=\mu})^{-1} \tag{3.23}$$

The poles of the renormalized Green's functions as in eqns. 3.20 and 3.21 satisfy the quadratic equation

$$(\omega - \mu - \tilde{\epsilon}_{f,\mathbf{k}})(\omega - \epsilon_{\mathbf{k}}) - |\tilde{V}_{\mathbf{k}}|^2 = 0 \tag{3.24}$$

that gives two hybridized bands as its solution, whose dispersion can be written as

$$E^{\pm}_{\mathbf{k}} = \frac{\mu + \tilde{\epsilon}_{f,\mathbf{k}} + \epsilon_{\mathbf{k}} \pm \sqrt{(\mu + \tilde{\epsilon}_{f,\mathbf{k}} - \epsilon_{\mathbf{k}})^2 + 4|\tilde{V}_{\mathbf{k}}|^2}}{2} \tag{3.25}$$

The obtained dispersion shown in Fig. 3.13 is the heavy fermion band structure that derive its large effective mass from the flattening of the dispersion near the chemical potential as dressed f electrons hybridize with the delocalized states. Consequently, effective mass of the carriers grows substantially as the *heavy* quasiparticles are born. Hybridized branches of the renormalized band structure leads to a direct hybridization gap of size $2|\tilde{V}_{\mathbf{k}}|$ that is often referred to in the heavy fermion literature. One can also define an indirect hybridization gap $\Delta_g \approx |\tilde{V}_{\mathbf{k}}|^2$ which can be largely dependent on the underlying dispersion of the renormalized f states and is truly defined when the two hybridization-split branches do not cross. Evidence for existence such a gap has been claimed from optical spectroscopy[72], photoemission[73] and tunneling spectroscopies[74], however, the precise nature of it needs to be well understood as it has a significant bearing on the emergent properties as will be discussed in this thesis.

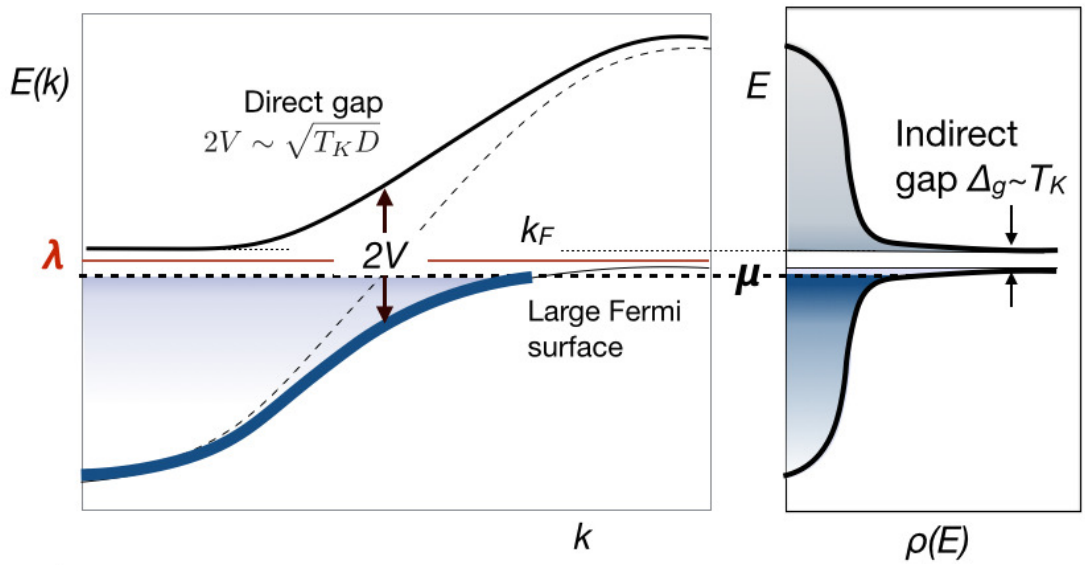

Figure 3.13: A solution of the periodic Andersion model, used to describe Kondo lattice systems predicts the emergence of hybridized heavy bands at low temperatures that is widely used in literature. Correspondingly a a) direct and b) indirect hybridization gap can be defined, as described in the text. Such a treatment cannot correctly capture the crossover as it artificially breaks the local gauge symmetry, hence predicts a phase transition. Nevertheless, the prediction is generally assumed to be valid in the low and high temperature limit. Adapted from [54]

3.3.3 Two fluid model of the Kondo Lattice

In the previous sections we have outlined expectations from simple models that try to capture the physics of the Kondo lattice systems. Though they have been successful in explaining broad general trends and provide a good starting point to understand these materials they have failed to produce a consistent framework and simple phenomenological description of them within which one can understand various emergent properties observed in different materials belonging to the *Kondo Lattice* family including onset of anti-ferromagnetic ordering, emergence of heavy Fermi liquid, onset of superconductivity and its relation

to quantum criticality, hidden-order phases. Much of the difficulty lies in our lack of understanding of the nature of the strongly correlated f states and the influence of the crystal environment on them that play a strong role in their interaction with the delocalized Bloch states from which various non-trivial behavior emerge.[75]

In this section we will discuss remarkable scaling relations exhibited by *Kondo lattice* systems and a phenomenological two-fluid model that has been used to describe them, which might lead to a proper microscopic theory for these materials. Appreciating the inherent dichotomy of the f states in the *Kondo Lattice* systems where they undergo a transition from a mostly localized to an itinerant character, Nakatsuji *et.al.*[76] first suggested a scaling behavior for heavy fermions using a two-fluid description that was later extended by Yang and Pines.[77, 78] The two fluid description comprise of a Kondo liquid comprising of itinerant emergent heavy-electrons characterized by an order parameter *f(T/T*)* that increases as the temperature is decreased and scales with T*, while the other component can be thought of as a hybridized spin liquid with order parameter *1 - f(T/T*)* that are made up of weakly interacting spin moments similar to the case of a collection of non-interacting Kondo impurities that are very weakly interacting with each other via a RKKY interaction. An analysis of the bulk susceptibility and fits to the experimental temperature dependent specific data within this model leads to the order parameter being described as

$$f(T/T^*) = f(0)(1 - \frac{T}{T^*})^{3/2} \tag{3.26}$$

and

$$m^*_{KL} = m_h(1 + ln\frac{T*}{T}) \tag{3.27}$$

where m_h is the quasiparticle effective mass at T*. From the above two equations one can then obtain an expression for density of states of the Kondo liquid as a

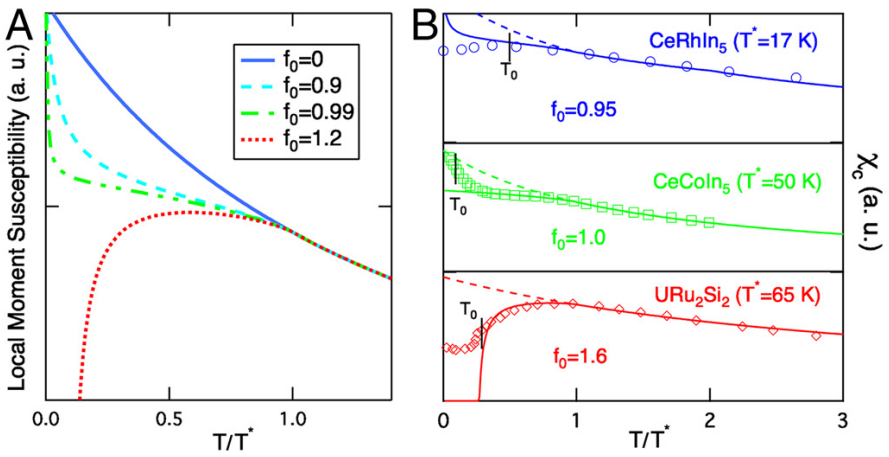

Figure 3.14: a) Predicted temperature dependence of static magnetic susceptibility as a function of *hybridization effectiveness - f_0)*, a parameter used in the two-fluid description and is described in the text. b) Fits to experimentally observed susceptibility variation in real materials, including $CeRhIn_5$, $CeCoIn_5$, and URu_2Si_2, from which an estimate of f_0 can be obtained. Adapted from [79]

function of temperature given by

$$\rho_{KL} = (1 - \frac{T}{T^*})^{3/2}(1 + ln\frac{T*}{T}) \tag{3.28}$$

Such a scaling behavior is found to be well reproduced by experimental data on Knight shift[80], anomalous Hall effect, calculated density of states within a DFT+DMFT approach etc.[77, 78] in the temperature range between T* and another lower temperature where some other order sets in such as antiferromagnetism and superconductivity. The energy scale for the emergence of Kondo liquid is given by T* that is distinguished form the single-ion Kondo temperature (T_K) discussed earlier in the sense that while T_K sets the scale for local hybridization T* captures the collective coherent behavior due to feedback from many different local hybridization channels in a lattice, leading to the emergence of a Kondo liquid that has no counterpart in the single-ion Kondo problem. Further-

more, meaning can be ascribed to the functional form in eqn. 3.26 if we consider the pre-factor $f(0)$ as representing *hybridization effectiveness*. The underlying idea being that for materials for which $f(0)$ is less than one an antiferromagnetic order is likely to emerge out of the two-fluid regime as the ground state at low temperatures while for compounds with $f(0)$ greater than one, some other kind of order is likely to emerge such as superconductivity, hidden order, fermi liquid etc. $f(0)$ can be estimated from static spin susceptibility assuming that below T* magnetic susceptibility in Kondo lattice systems is entirely determined by the hybridized spin fluid component whose dynamic spin susceptibility can be written as

$$\chi_l(q,\omega) = \frac{f_l \chi_0}{1 - zJ_Q f_{l0} - \iota\omega/\gamma_l} \tag{3.29}$$

where f_l is the order parameter fro hybridized spin liquid, χ_0 is the local susceptibility of a f spin moment, z is the coordination number, γ_l is the local relaxation rate and J_q is the RKKY coupling strength. We further assume above T* χ_0 is C/T with C being the Curie constant which takes a Curie Weiss form $\chi_l(0,0)$ = C/(T+θ), where $\theta = CzJ_{q=0}$.

In Fig. 3.14 fitting results to the experimental susceptibility data are shown with the functional form in eqn. 3.29 where θ/T^* is the only free parameter. Results for a few of the prominent Kondo lattice systems is summarized in Table 3.1, reproduced from [79], including URu_2Si_2 and $YbAl_3$, compounds that are investigated in this thesis.

Table 3.1: Hybridization effectiveness and low-temperature order

Materials	T*(K)	$T_{N/L/c}$(K)	f_0	Order
Local-moment order				
$CePt_2In_7$	41	5.6	0.4	AFM
$CePb_3$	16	1.1	0.5	AFM
UPd_2Al_3	60	14.3	0.8	AFM
$CeRhIn_5$	17	3.8	0.95	AFM
Kondo liquid order				
$CeCoIn_5$	50	2.3	1.0	SC
UPt_3	25	5	1.4	SC
$YbAl_3$	160	38	1.5	FL
URu_2Si_2	65	17.5	1.6	HO
UNi_2Al_3	120	39	1.8	SDW

AFM: antiferromagnetism; SC: superconductivity; FL: Fermi liquid; HO: hidden order; SDW: spin-density wave antiferromagnetism

3.4 Conclusions and Outlook

In this chapter we have discussed a broad framework within which fascinating properties of *Kondo Lattice* systems can be understood. Unifying experimental signatures of these systems have been identified and can be broadly understood in terms of the theoretical framework describing emergence of *heavy* hybridized bands at low temperatures as a gradual crossover. However, in many cases serious discrepancies remain between theory and experiments and for certain compounds we do not yet have a correct description of their ground state. It

is increasingly being realized that the subtleties involved in the emergence of *heavy* itinerant carriers holds the key to gain an insight into the underlying microscopic mechanisms at play. Advanced spectroscopy tools such as ARPES and SI-STM because of their unique *r*-space and *k*-space resolving capabilities along with high energy resolution can potentially play a crucial role providing novel information, thus significantly advancing our understanding of these materials. In this thesis we will employ ARPES to understand the nature of the *hidden-order* phase in URu_2Si_2[81] and elucidate the connection between *k*-space and *r*-space electronic structure in mixed valence systems by investigating a prototypical mixed valence compound $YbAl_3$[32].

CHAPTER 4

HIDDEN ORDER IN URu_2Si_2

4.1 Introduction

URu_2Si_2 is an actinide inter-metallic compound with a modest enhancement in the effective mass of its carriers (γ = 110 mJ / molK^2) [83] and becomes superconducting below a transition temperature (T_C) of 1.5 K.[84] But, perhaps the most intriguing and fascinating aspect of this compound that continues to challenge researchers to this date is the nature of the ordering that it undergoes at T_{HO} = 17.5 K.[41, 85, 83] Interestingly, 'hidden-order' appears to be a precursor phase for superconductivity in this material as destruction of the hidden order phase on application of pressure (magnetic field) that stabilizes large moment anti-ferromagnetic (LMAF) phase (other not well-characterized phases) also destroys superconductivity.[86, 87, 88, 89, 90, 91] (Fig. 4.1)

From transport and thermodynamic measurements including specific heat, magnetic susceptibility, Hall resistivity etc. it is clear that the phase transition occurring at 17.5 K is of a second-order variety. But it's the underlying order parameter that has remained enigmatic and thus, has come to be known as 'hidden-order' phase transition.[81] Understanding this phase is further complicated because the paramagnetic phase, from which the 'hidden-order' phase emerges is still not well understood. Largely, at the heart of this difficulty is our inadequate knowledge of the correct description of the strongly correlated Uranium 5f states. Though, it was traditionally thought to undergo a crossover at around T* $\approx$ 60 - 70 K,[92] below which coherent heavy bands are expected to emerge (as described in the previous chapter), we will show that the generic

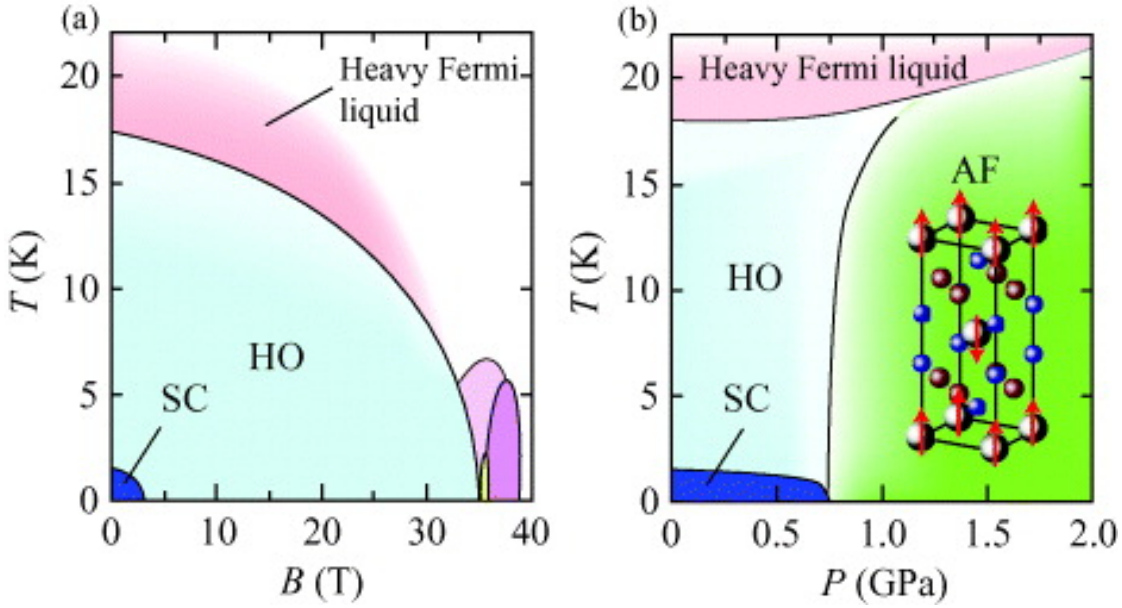

Figure 4.1: a)Temperature-Magnetic field and b)Temperature-Pressure phase diagram in URu_2Si_2. Note that though it is widely assumed that the phase above the *hidden-order* temperature can be characterized by a Heavy Fermi liquid, recent experiments has revealed that this phase is characterized by incoherent *f* states[82, 74], neither it shows behavior expected of a typical Fermi liquid.[153]

picture for heavy fermions is not exactly applicable in URu_2Si_2 but, is more involved. Over the past years many theoretical and experimental efforts has been made to explain the 'hidden-order' phenomenon assuming either an itinerant or a localized approach with various degrees of success but none has yet been able to completely demystify the 'hidden-order' phase. In this chapter I will briefly describe and evaluate the current status of our understanding of the 'hidden-order' phase.

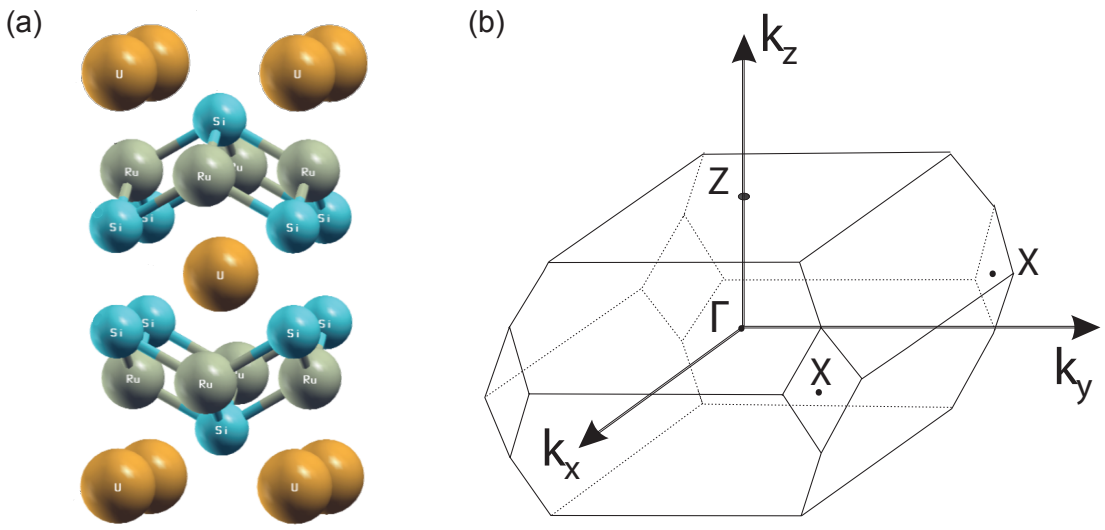

Figure 4.2: a) Crystal Structure and b) Brillouin Zone of URu_2Si_2

4.2 Electronic Structure of the Paramagnetic phase

URu_2Si_2 crystallizes in a body-centered tetragonal structure in the paramagnetic phase having a space group I4/mmm (139) with in-plane and out-of-plane lattice constants $a = b = 4.12$ Å and $c = 9.12$ Å, respectively. Crystal structure and corresponding Brillouin zone is shown in Fig. 4.2. Each layer in the lattice has a single element, with U and Si having similar sub-lattice periodicity of $a_0 = 4.12$ Å, while the Ru atoms have a spacing of $a_0/\sqrt{2} = 2.19$ Å.[93]

In the paramagnetic state, electronic structure in URu_2Si_2 has been probed in some detail employing ARPES and was compared with LDA calculations. It was found that the valence band in URu_2Si_2 mostly comprise of contributions from Ru $4d$ and Si $3p$ states that agree fairly well with predictions from DFT based methods. However, significant disagreements were observed in the the near E_F features.[16, 94] This is not surprising as renormalized f states near the Fermi level are known to significantly modify low energy electronic structure in

Kondo lattice systems, such as in URu_2Si_2 that LDA type calculations often fail to reproduce owing to their inability to appropriately take into account strong correlations of the f states.

Uranium in URu_2Si_2 can be either in U^{4+} valence state with a $5f^2$ configuration corresponding to the localized picture for the f electrons or as U^{3+} with $5f^3$ configuration when the f electrons are itinerant. In the localized picture lowest lying multiplet is supposed to be $J = 4$ with a ninefold degeneracy. In a tetragonal environment the multiplet degeneracy is expected to be lifted giving seven crystal electric field (CEF) states where five of them are singlets while two are doublets. Observation of CEF excitations in neutron scattering or Schottky anomaly in magnetic entropy are the most common experimental techniques to establish the presence of localized CEF split states.[95] Early inelastic neutron scattering experiments claimed to have observed four broad CEF transitions of the f states in URu_2Si_2 in the energy range 5 - 159 meV, and another small peak in the inelastic scattering spectrum at 363 meV that was assigned to inter-multiplet transition.*Schlabitz:1986* However, such a claim has been contested by later neutron scattering measurements.*Wiebe:2007* Furthermore, in the same experiment similar peak at 363 meV has also been observed for for which no such CEF transition of the f states is expected. Crystal field states were also not observed in STM measurements.[97, 74] Specific heat measurements in URu_2Si_2 show a maximum in C/T at ≈ 70 K which has sometimes been taken as an indication of the presence of CEF states.*Schlabitz:1986* But, again observation of a similar peak in C/T in calls that interpretation to question.[98] Sometimes the specific heat peak has also been taken as an indication of Kondo crossover.[92] But, strong Ising anisotropy exhibited by URu_2Si_2 in both its transport and thermodynamic response such as resistivity, specific heat, magnetic susceptibility etc. finds a

ready explanation in the localized model of the f states.[99, 100] However, a DFT based work recently has claimed to be able to explain such an anisotropy in physical properties starting form an itinerant f states.[101] It also must be noted that magnetic susceptibility of URu_2Si_2 does not exhibit a Curie-Weiss behavior at $\approx$ 70 K but only commences above $\approx$ 150 K.[92] From the above discussion, it thus appears that there is no compelling experimental evidence for the localization of the f states in URu_2Si_2.

On the other hand, assumption of an itinerant character for the f states is also not well established. Most claiming an itinerant character draws support from an apparent good correspondence between ARPES and itinerant DFT results that, as we will later discuss leaves much to be desired.[102, 103] However, observation of itinerant spin excitation in neutron scattering and weakly dispersive f states in ARPES does indicate that at least in the 'hidden-order' phase f electrons acquire some itinerant character.[96] One might therefore expect in reality probably some aspects of both features is present that is, the f electrons in URu_2Si_2has a dual character that is somewhat intermediate between the completely localized and completely itinerant viewpoint.

Progress has recently been made to estimate the effective uranium valence in the paramagnetic phase. Resonance x-ray emission spectroscopy (RXES) at the uranium L_{III} edge reported an average $4f$ occupancy n_f = 2.87 ± 0.08 with no temperature dependence between room temperature and 10 K within their experimental resolution.[104] This is in agreement with electron energy-loss experiments that report an effective uranium f occupation of n_f = 2.71 ± 0.1 in URu_2Si_2. More importantly, a spin-orbit analysis of the $N_{4,5}$ EELS spectra puts URu_2Si_2 in the intermediate coupling regime (where neither J, nor L,S are good

quantum numbers) underscoring the complexity of this system.[105] Finally, Knight shift measurements by Shirer et.al. revealed a remarkable correspondence of the shift with expectations from a two-fluid model (discussed in the previous chapter) indicating the presence of both types of carriers.[80] Development of a microscopic theory explaining such a scaling behavior would be immensely enlightening in understanding the mysterious 'hidden-order' phase in URu_2Si_2.

4.3 Signatures of the 'Hidden-order' phase : Early experiments

Thermodynamic measurements as early as in 1985 first reported signatures of the second order phase transition now commonly known as the 'hidden-order' transition at T_{HO}= 17.5 K in URu_2Si_2 (Fig. 4.3).[41, 83, 85]

Initially the phase was variously assigned be a weak type antiferromagnet,[41] a static charge density wave or spin density wave[83] and a local U moment antiferromagnet[85] all three of which is now known to be incorrect. Such measurements and observed jump in resistivity at 17.5 K also indicated gapping of the Fermi surface at the transition that is further supported by optical measurements. The change in entropy at the transition temperature is approximately *0.2Rln2*, which would indicate development of large magnetic moment if the origin of the phase was magnetic. However, the moment size found in neutron scattering measurements was only 0.04 μ_B, that too was later shown to be extrinsic with subsequent improvement in crystal quality.[106, 107, 108] Consequently, over the last decades an intense search has been undertaken, both with theoretical and experimental approaches to uncover the ordering at the second

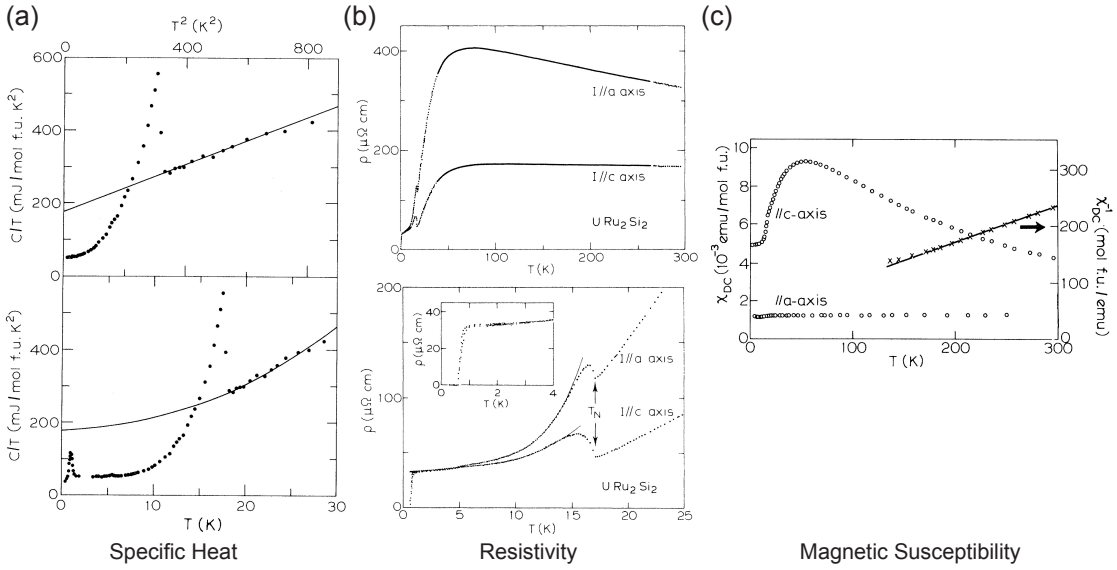

Figure 4.3: Temperature dependence of a) specific heat b) resistivity and c)magnetic susceptibility illustrating signatures of the 'hidden-order' phase in URu_2Si_2. Note strong anisotropy in the 'hidden-order' phase.

order phase transition that has remained 'hidden'.

4.4 Theoretical Proposals for the 'Hidden-order' in URu_2Si_2

Theoretical proposals for the 'hidden-order' phase can be separated into two different classes - one that starts from a localized description of the U 5*f* states - among them a large number predict multi-polar order of some kind of the Uranium ion. On the opposite extreme, a great many proposals start from the itinerant description of the 5*f* states where they from dispersive states near the Fermi level and consider instabilities of the Fermi surface that induces a charge gap at T_{HO}. In Table 4.1 we list prominent proposals belonging to both classifications. None of them are discussed in any length as they fall outside the scope

of this thesis. Interested readers are directed to the relevant references.

4.5 Symmetry Breaking in the *hidden-order* phase

In order to narrow down the search for the possible explanation of the hidden order phase a rewarding approach might be identification of the broken symmetries at T_{HO}. In this regard three symmetries that are claimed to be broken are:

a) translational symmetry along the c-axis that doubles the unit cell along that direction thus changing the crystal structure from body-centered tetragonal to simple tetragonal

b) four fold rotational symmetry that reduces the symmetry of the system from C4 to C2 and associated orthorhombic distortion

c) time reversal symmetry

Each one of these has been controversial with conflicting reports and are yet to be conclusively established. Once established this will greatly help to isolate relevant theoretical proposals for the URu_2Si_2 case, as different proposals rely on different symmetry breaking. Here, I will very briefly describe each of these proposed symmetry breaking aspects.

Main experimental support for translational symmetry breaking along the c-axis in URu_2Si_2 comes from quantum oscillation (Subinkov - de Hass (SdH) and de Haas - van Alphen (dhVA)) measurements. It was observed that the angular dependence of various cyclotron branches remains unchanged with applica-

tion of pressure when the LMAF phase is stabilized.[91] As, in the LMAF phase translational symmetry is clearly broken it was assumed that such symmetry breaking should also happen in the 'hidden-order' phase. But, it should be noted that quantum oscillation only access a small portion of the Brillouin zone. So, as most portion of the Brillouin zone remains unaffected by such a symmetry reduction it should not be surprising if quantum oscillation measurements fail to detect any change on symmetry reduction under pressure. Observed cyclotron branches were also found to agree with itinerant DFT calculations albeit with different effective mass (m^*) that led to the belief that this is due to dynamic magnetic fluctuation that makes adjacent Uranium ions in the neighboring basal plane different thus, reducing the symmetry.[122] However, recent inelastic neutron and x-ray scattering experiment has mapped out both magnetic and lattice excitation spectrum over the whole Brillouin zone confirming that they obey body-centered tetragonal brillouin zone with no indication of spatial symmetry reduction in the 'hidden-order' phase. They also reveal that the measured excitation spectrum do not agree with calculated Fermi surface from DFT with f electrons either as itinerant or localized. Furthermore, their inferred cross-sectional Fermi surface from the measured excitation spectrum is compatible with quantum oscillation results as zone folding would not change extremal orbits for the inferred Fermi surface topology.[128] Another claim of translational symmetry breaking has come from ARPES results that is incredibly tenuous[102, 103] and put into perspective in the next chapter.

Evidence for four fold rotational symmetry breaking has primarily come from magnetic torque measurements.

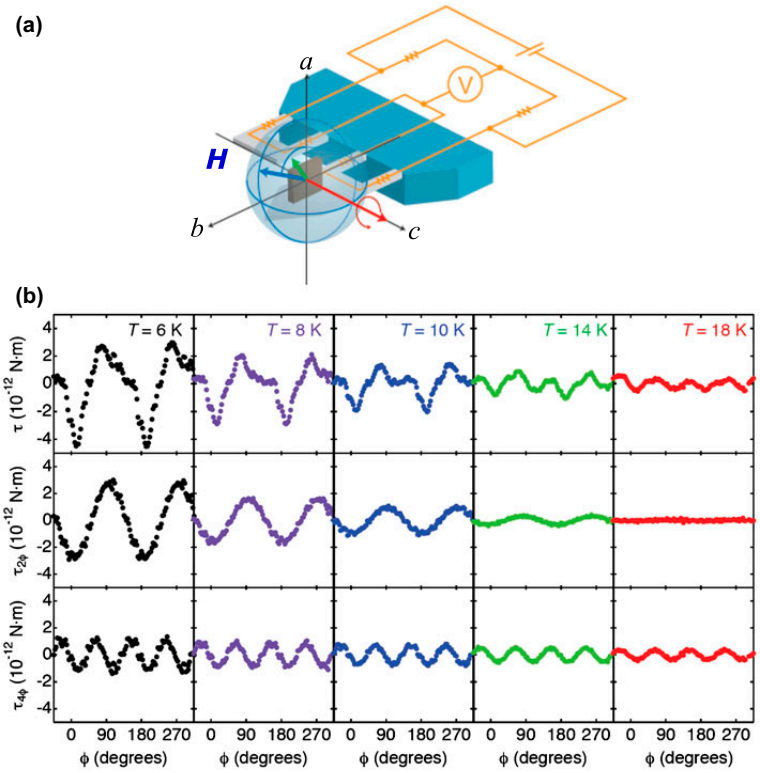

Figure 4.4: Torque magnetometry measurements, as described in the text, indicating C4 symmetry breaking in the 'hidden-order' phase in URu_2Si_2. a) The experimental setup used for the measurement. b) in addition to the 4-fold component to the magnetic torque that respects the lattice symmetry a 2-fold component can also be identified below the 'hidden-order' phase indicating symmetry breaking.

Another symmetry that divides many theoretical proposals is the time reversal symmetry with one group of theories claiming it is broken while others do not require any such symmetry breaking. Early neutron scattering experiments observed tiny magnetic moment along the c-axis which has later been proved to be extrinsic.[81] Furthermore, no in-plane magnetic moment has been observed neither in recent neutron scattering data or in bulk magnetization measurements as predicted by a recent theory of hastatic order.[136, 137, 138, 100] However, an increase in linewidth on entering the 'hidden-order' phase is seen

in recent ^{29}Si NMR[139], muon spin rotation[140] that can be taken as evidence for time reversal symmetry breaking. Because, such a broadening is consistent with the additional hyperfine internal field at the Si sites due to multipolar ordering at the U sites that break time reversal symmetry. Temperature dependence of the additional line width broadening follows closely observed orthorhombicity from x-ray diffraction studies indicating similar origin of the two phenomena. However, the observed line width broadening is much less in better quality single crystals again raising the question of it being of a parasitic nature dependent on crystal quality. Moreover, polar Kerr effect (PKE) measurements do not detect any indication of time reversal symmetry breaking in the 'hidden-order' phase, while they find it is broken in the superconducting phase[141]. This can be reconciled by noting that while PKE is sensitive to net ferromagnetic magnetization, NMR is a local probe. Thus presence of micron size domains with compensating magnetization can lead to a null result in a PKE measurement. But, this still needs further experimental verification.

4.6 Conclusion

From the above discussion it is clear that URu_2Si_2 poses a significant theoretical and experimental challenge with ample indication of competing orders being intertwined, perhaps a signature of strong correlations. But even with complexities of the 'hidden-order' and superconducting phases kept aside aspects of the Kondo physics and the nature of the *heavy fermion* character in URu_2Si_2 is still not well understood. Most work relies on transport and thermodynamic signatures, which for URu_2Si_2 indicates a Kondo temperature of $T_K \approx 60 - 70K$ and it is generally assumed that below the crossover temperature itinerant hybridized

heavy f states (as discussed in Chapter 2) are formed. However, such measurements provide momentum averaged information of the low energy carriers and are often strongly influenced by factors such as crystal field effects that are difficult to separate. Thus, in multi-band systems such as URu_2Si_2, k-resolved information of the low energy electronic structure, as described in the next chapter, is essential to understand the nature of the electronic states from which the heavy fermion states emerge that might hold the key to solve the 'hidden-order' problem

Table 4.1: Selected Theoretical Proposals for the *hidden order* phase in URu_2Si_2

Authors	Year	Order
Local 5*f* picture		
Nieuwenhuys	1987	dipole(2^1) order[109]
Santini and Amoretti	1994	quadrupolar(2^1) order[110]
Okuno and Miyake	1998	CEF and quantum fluctuations[111]
Chandra et. al.	2002	orbital currents[112]
Kiss and Fazekas	2005	octupolar(2^3) order[113]
Haule and Kotliar	2009	hexadecapolar(2^4) order[114]
Cricchio et. al.	2009	dotriacontapolar(2^5) order[115]
Harima et. al.	2010	antiferro quadrupolar order[116]
Thalmeier and Takimoto	2011	E(1,1)-type quadrupole[117]
Ikeda et. al.	2012	E^--type dotriacontapole[119]
Chandra et. al.	2013	Hastatic order[100]
Kung et. al.	2015	Chirality density wave[120]
Itinerant 5*f* picture		
Viroszek et. al.	2002	unconv. spin density wave[121]
Elgazzar et. al.	2009	dynamic symmetry breaking[122]
Dubi and Balatsky	2011	hybridization wave[123]
Pepin et. al.	2011	modulated spin liquid[124]
Riseborough et. al.	2012	unconv. spin-orbital density wave[125]
Das et. al.	2012	spin-orbital density wave[126]
Hsu and Chakravarty	2013	singlet-triplet *d*-density wave[127]

CHAPTER 5

EMERGENCE OF A COHERENT HEAVY FERMION LIQUID AT THE HIDDEN ORDER TRANSITION IN URu_2Si_2

5.1 Introduction

Spectroscopic probes that provide information about electronic structure in a momentum and spatially resolved manner offer invaluable insights into identifying and distinguishing contributions from disparate electronic states in multiband systems, such as in URu_2Si_2 that might lead to a microscopic understanding of its properties. ARPES and STM are two such probes that stand out in this regard providing complementary information as they can directly access momentum and spatially resolved single particle spectral function, respectively. Moreover, using novel quasi-particle interference scattering (QPI) technique STM can also provide indirect information about the momentum space structure under certain assumptions of the underlying band structure.[74] In the last chapter we reviewed various aspects of the intriguing nature of the *hidden order*(HO) phase in URu_2Si_2. In this chapter we will describe our efforts to understand the electronic structure in URu_2Si_2, both in the *hidden order* and the paramagnetic phase from which the *hidden order* phase emerges. In particular, using ARPES we will show how a coherent heavy fermion liquid emerges in the 'hidden-order' phase in URu_2Si_2 via a phase transition and discuss its implications on the hidden-order parameter. We will also discuss new perspectives gained from our experiments particularly, in context of other similar measurements employing ARPES and STM.

Part of the work described in this chapter has been published in S. Chatterjee *et. al., Phys. Rev. Lett. 110, 186401 (2013)*

Early photoemission measurements had already indicated that the valence band in URu_2Si_2 primarily comprise of electronic states with Ru 4*d* and Si 3*p* character. Evidence was also found for the presence of non-dispersive states in the paramagnetic phase presumably of U 5*f* character close to the Fermi level.[94, 16] However, to gain an understanding of the implications of its electronic structure on the observed physical properties one needs to characterize low energy excitations in this material with high energy resolution and improved temperature control that would allow investigation of its electronic structure both sufficiently below and above the *hidden-order* transition temperature (T_{HO}). This was lacking in earlier experiments which were performed only in the paramagnetic phase and with low energy resolution. However, recent improvements both in energy and momentum resolution and temperature control has made possible to perform experiments with much higher precision that has greatly aided our understanding of its electronic structure as is described below.

Most of the experiments presented here were performed at the 1^3-endstation on beamline UE112-PGM2 at the Berlin Synchrotron BESSY II with an overall energy resolution better than 7 meV (We would like to note that calibration of the energy resolution was difficult in the beamline because fresh gold was not available to measure the fermi edge. *In situ* argon sputtering to clean gold surfaces exposed to atmosphere did not work well. We made our own gold evaporator and measured gold surfaces evaporated in low vacuum condition that is not ideal. However, from an analysis of the sub-optimal gold spectra we can put an upper bound on the energy resolution at 7 meV. However, best fits to our data suggest that instrumental resolution is around 3 meV) and a base temperature lower than 2K. Some of the experiments were also performed at the PGM beamline of now closed Synchrotron Radiation Center (SRC) at Wisconsin, Madison

with an overall energy resolution of 12 meV and a base temoerature of 32 K. In both the cases a Gammadata R4000 anlyzer was used. The Fermi energy was determined by measuring a polycrystalline gold film in thermal contact with the sample. Single crystals of URu_2Si_2 were cleaved *in situ* at a base pressure of better than 4×10^{-11} torr, which yielded flat shiny surfaces parallel to the crystallographic *ab*-planes. None of the features reported in the following showed any dependence on sample or cleavage unless mentioned otherwise. The polarization of the incident photon beam was set to Linear Vertical (LV) unless mentioned otherwise.

5.2 General Electronic Structure

In Fig. 5.1, we show ARPES spectra along the (0,0) - (π,0) direction deep within the HO phase at a variety of different photon energies. The spectra in Fig. 5.1 a)-e) exhibit a dramatic dependence on the incident photon energies, revealing a multitude of electronic states near ($k_x = 0, k_y = 0$). We emphasize that at no single photon energy are we able to clearly distinguish all five features, thus underscoring the importance of photon energy dependent measurements in revealing and disentangling the complete electronic structure of URu_2Si_2. A compilation of these different features is shown in Fig. 5.1 f). Feature 1 has been previously shown to be of surface origin, while feature 2 corresponds to a light hole-like band which has been attributed to a bulk state [144, 143] and has also been found to be robust to surface doping.[144] Feature 3 exhibits an 'M'-shaped dispersion also reported at 7 eV [145, 146], and is connected to a relatively flat band (feature 4) ostensibly of predominantly U $5f$ character. Finally, hole-like states (feature 5) that cross the Fermi level E_F at $k_x \approx 0.54\ \pi/a$ form propeller-shaped

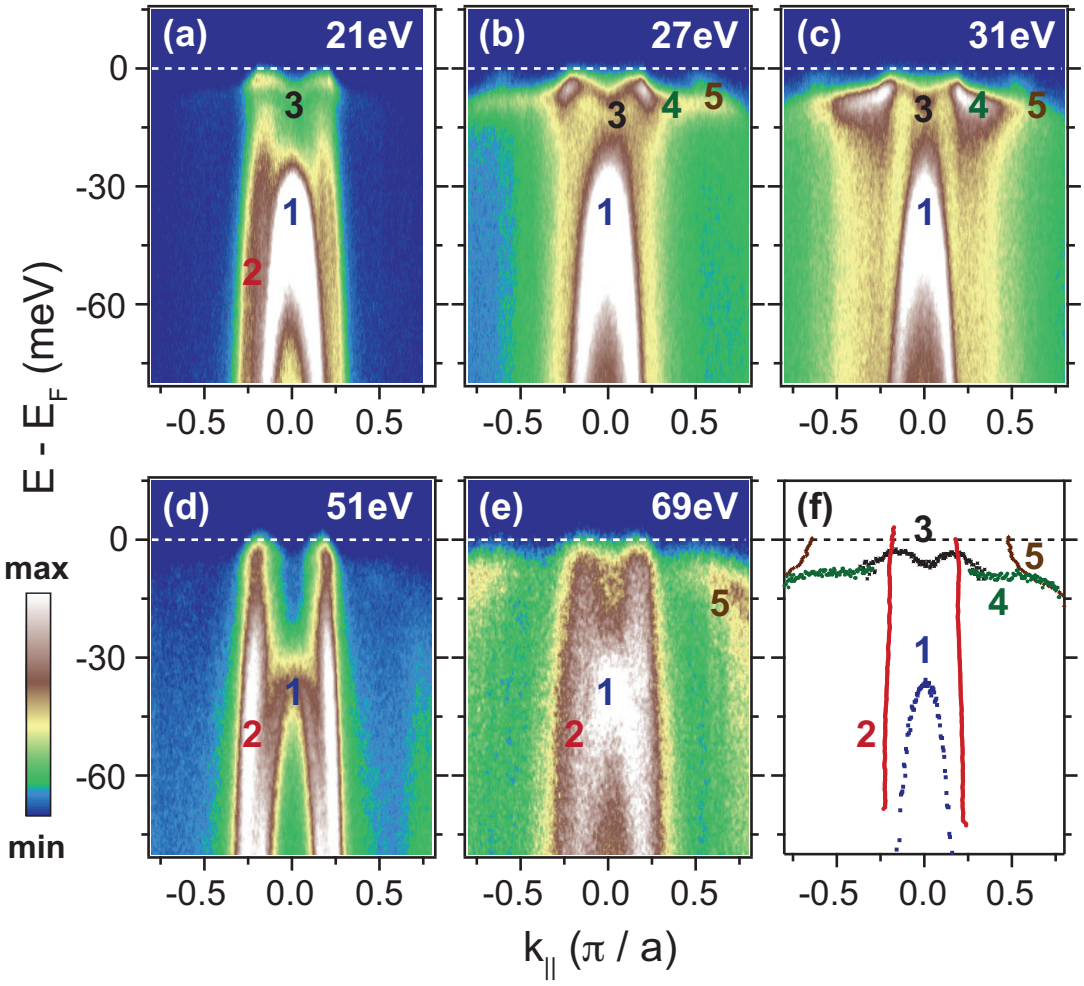

Figure 5.1: (a-e) ARPES spectra along the $(0,0)$ - $(\pi,0)$ for different excitation energies (noted in the top right of each image) measured at 2 K, deep inside the hidden order (HO) phase. (f) Dispersions of all the different features obtained from fits to corresponding EDC/MDCs.

Fermi surface (FS) sheets, also observed in quantum oscillation measurements [149, 148].

By changing photon energy, we can probe different values of k_z along the (001) direction and can therefore determine the electronic dispersion perpendicular to the Ru_2Si_2 planes. We do not observe any appreciable dispersion along

k_z for features 2, 3, and 4, while feature 1 has already been ascribed to a surface-derived origin and feature 5 is apparent at only very few photon energies, but found to be weakly dispersive. Features 3 and 4, primarily of U 5*f* character is expected to have a weakly dispersive character in agreement with our experimental observation. For feature 2 the light hole band, two reported FS sheets by Shubnikov-de Haas (SdH) oscillations [149, 150, 152] exhibits an extremal k_F close to that of feature 2. One is a relatively ($m^* = 11m_e$) heavy hole like band, known as the α branch, and another is a light ellipsoidal electron like band, known as the ϵ branch. However, from the quantum oscillation measurements both these branches also appear to be closed along the (001) direction.

At face value, this strong k_z dependence appears inconsistent with our observation of lack of significant dispersion of the hole pocket in k_z. However, this could be resolved by the fact that our measurements are performed in absence of a magnetic field, whereas the α and ϵ branches are seen only above a field of 3 T and 21 T, respectively. While it can be argued that 3 T is a relatively small field strength, it is known that in heavy fermion systems even a small field can dramatically alter their low energy excitations due to tiny energy scale associatd with these materials.[151] So, this possibility cannot be entirely ruled out. Furthermore, our measurements reveal that temperatures at which quantum oscillation measurements have been performed the hole like band via hybridization with the *f* states is transformed into a heavy band with effective mass $m^* \approx 25\ m_e$. This is consistent with other measurements [74, 83, 41] that do not correspond with the estimated effective mass of either of the observed pockets. While we cannot definitively ascertain the provenance of this pocket, it is also possible that the heavy branch emerging out of the hole pocket is missed in the sdH measurements as electronic bands with large effective mass are in gen-

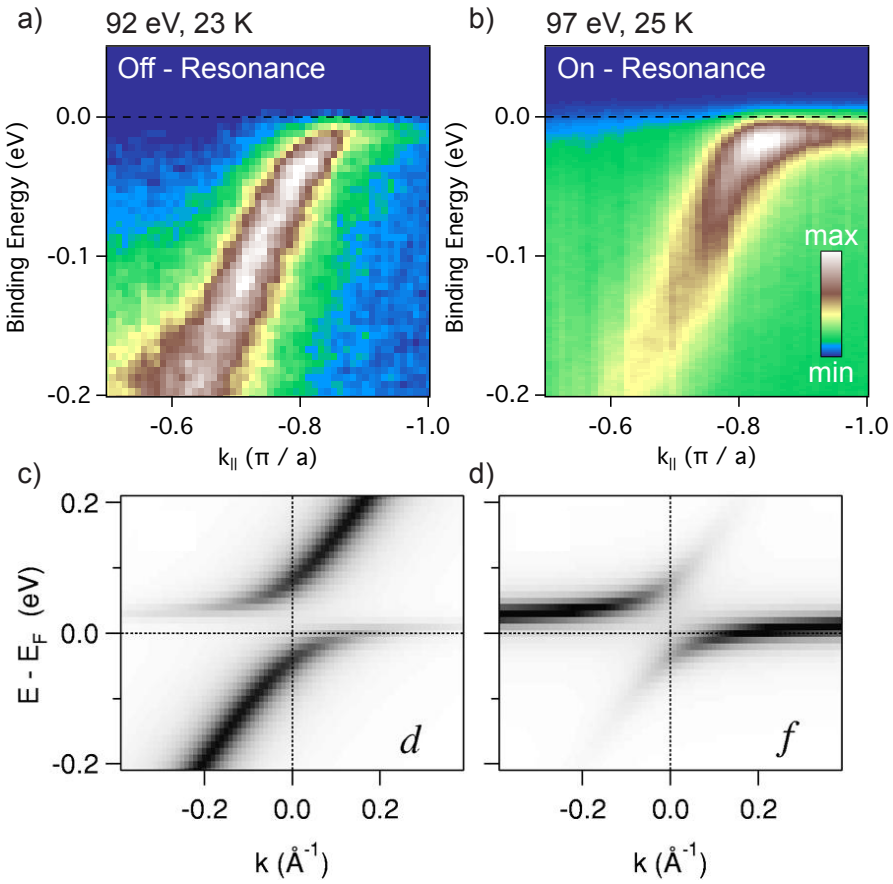

Figure 5.2: Electronic Structure at the X point in Uru_2Si_2 a) and b) Heavy hybridized bands can already be seen at the X point at 23 K, above T_{HO}. On resonance at 97 eV the $5f$ spectral weight is enhanced. Spectral images are obtained using Linear Horizontal (LH) polarized photons c) and d) Observed dispersion and the orbital character is found to be in excellent agreement with the expectations from a periodic Anderson model. Existence of hybridized heavy bands above T_{HO} at the X point has also been reported earlier at temperatures as high as 100 K. [16] Simulation figures are adapted from [16]

eral harder to detect in quantum oscillation measurements using low magnetic fields. Another aspect to consider is that the body centered tetragonal crystal structure of URu_2Si_2 has a fairly large c - axis lattice constant 9.12 Å and therefore, a much smaller extent of the irreducible Brillouin zone along k_z. Thus, π/c is not much larger than $\delta k_z = 1/\lambda_{mfp}$ for photon energies between 20 -100 eV as obtained from the Universal curve. (Fig. 2.2). Hence, for weakly dispersive bands it is possible that such effects would be washed out due to intrinsic experimental uncertainty in k_z resulting in the experimentally observed bands appearing to be two-dimensional in character, as is the case here. The main effect of varying photon energies in our measurements is to strongly modulate the photoelectron matrix elements of these different features, suggesting that these states have substantially different orbital character.

We will concentrate primarily on features 2, 3 and 4 in Fig. 5.1, all three of which undergo dramatic modifications across T_{HO}. The lack of obvious k_z dispersion makes it difficult to definitively assign these features to bulk states. Nevertheless, their strong temperature dependence as is described in the next section allows us to state conclusively that they are tied to the onset of HO in the bulk. Moreover, the absence of feature 3 in Rh-doped samples where the HO state is destroyed [145] further supports the assignment to bulk-derived states. This is further contrasted with the lack of temperature dependence of the electronic states around the X point that we will show is of surface origin.

In Fig.5.2 we show spectral map taken at (π,π) above T_{HO} (23 K), both at *off-resonance* (92 eV) and *on-resonance* (97 eV) corresponding to $5d + 5/2 \rightarrow 5f$ that is expected to enhance features with $5f$ character. Observed spectral features and their intensity modulation at off and on-resonance is in excellent corre-

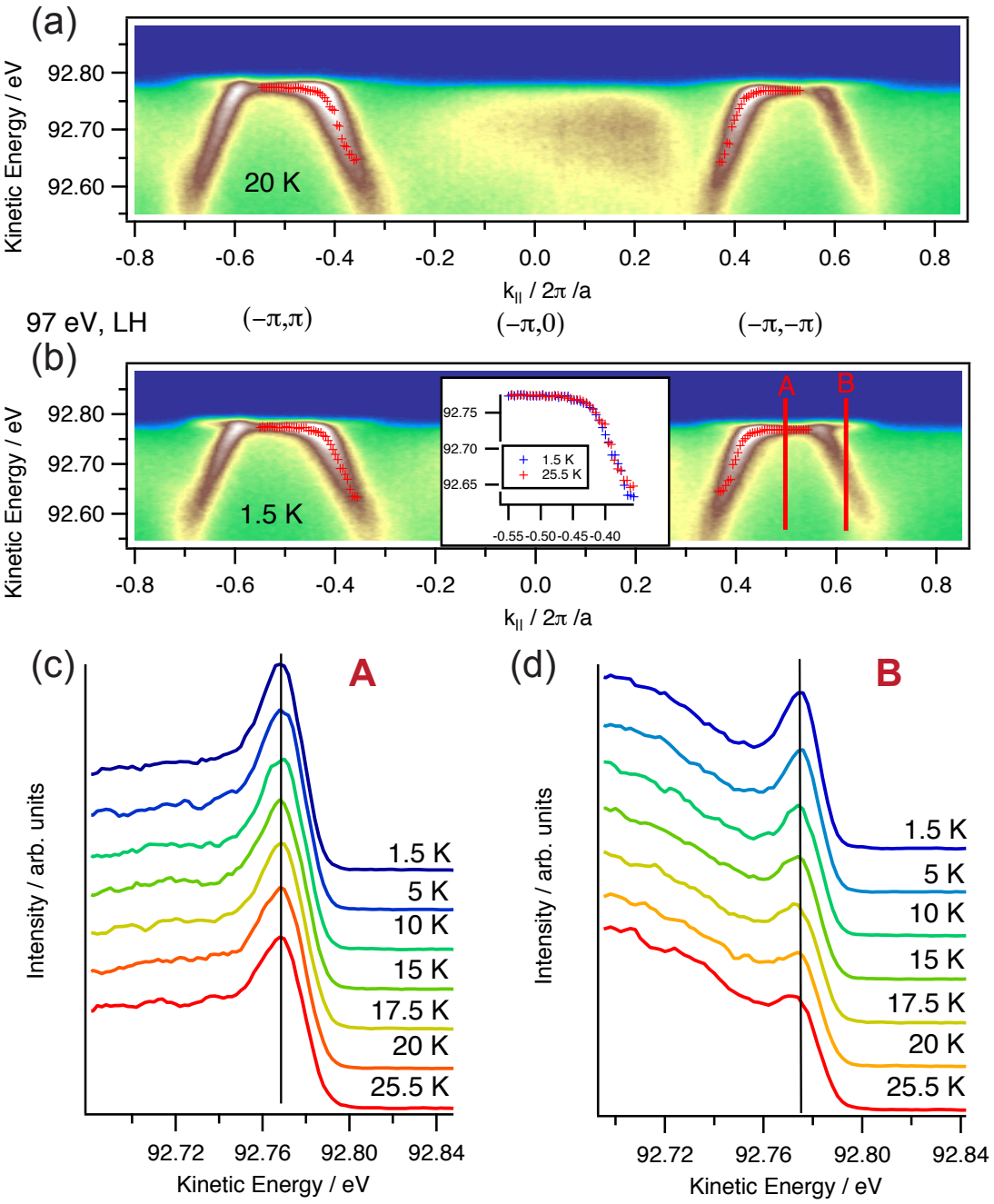

Figure 5.3: a) and b) Temperature dependence of the surface states at the X point showing no change in dispersion above and below T_{HO}. EDC cuts at A and B reveal no shift in binding energy of the surface state with temperature. Absence of any temperature dependence across the 'hidden-order' phase transition of the surface states at the X point is in sharp contrast with the behavior observed for the features 2,3 and 4 as discussed in the text. *Figure Courtesy: Jan Trinckauf*

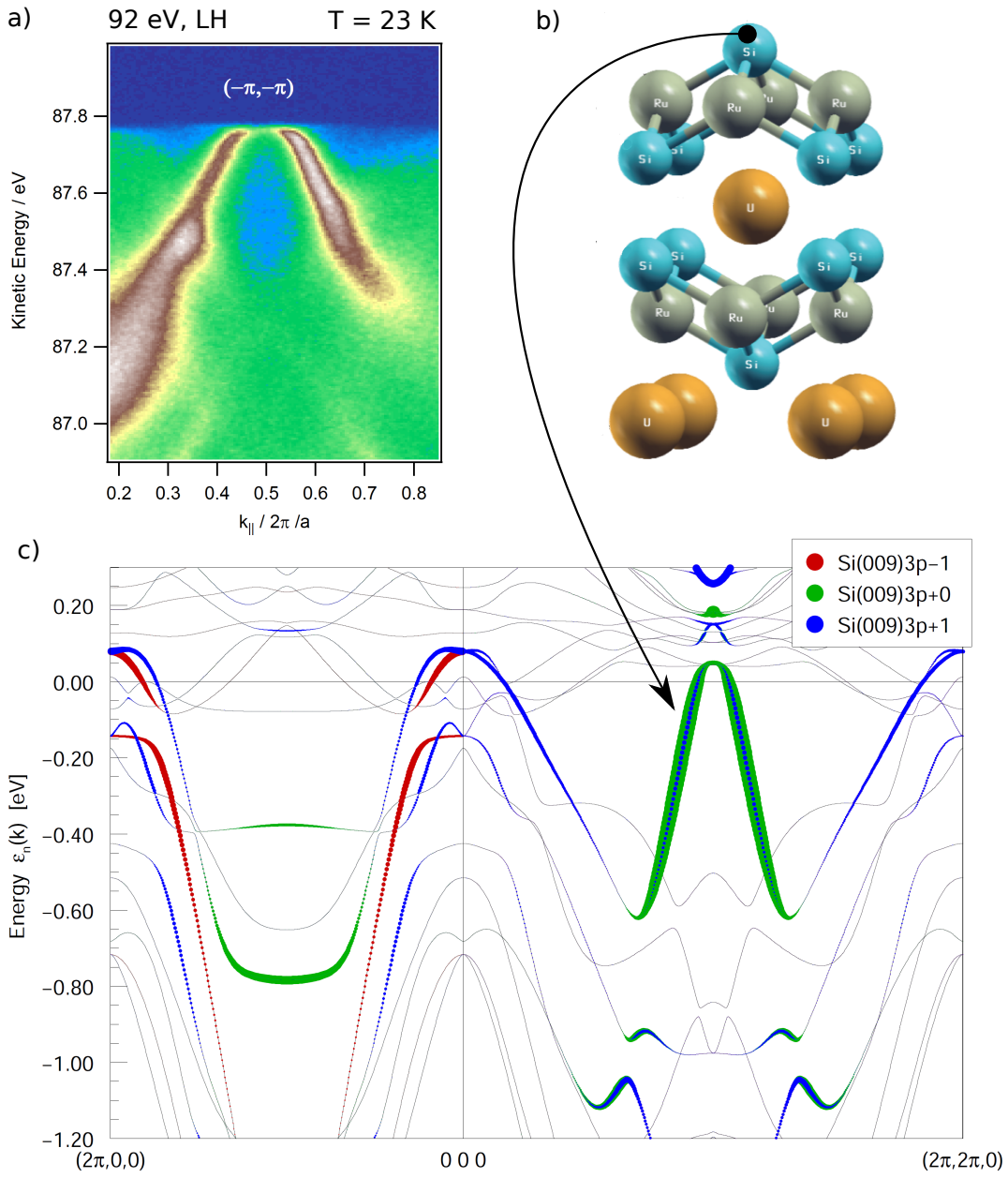

Figure 5.4: Surface origin of the hole like band at the X point in URu_2Si_2 a) The hole like band can be seen at the X point (π,π). The spectral map is taken using 92 eV photon energy with Linear Horizontal (LH) polarization. b) and c) Slab calculation with a Si terminated surface shows that the observed hole pocket at (π,π) is a surface state due to Si dangling bonds at the cleaved surface with Si termination. Dramatic shift in binding energy can be observed by treating the cleaved surface with hydrogen that saturates the dangling bonds.[142] *Figure and DFT calculation from Jan Trinckauf*

spondence with a mean field solution of the Anderson lattice model describing heavy bands of mixed orbital character emerging out of a hybridization process between the light hole like *d* band and flat *f* states. Thus, we find existence of hybridized heavy bands already at the X point above T_{HO} in agreement with earlier photoemission results.[16] Furthermore, as shown in Fig. 5.3 the spectral features at the X point are remarkably insensitive to the hidden-order phase showing no change across T_{HO}.

This contrasting temperature dependent response is reconciled by noting that the hole pocket at the X point has a surface origin resulting from the dangling Si bonds at the cleaved Si terminated surface. Surface treatment by hydrogen that saturates the Si dangling bonds results in a dramatic shift in binding energy of these states at the X point.[142] Furthermore, such a hole like band, that is not present in bulk DFT calculations can be reproduced in a super-cell calculation with a Si terminated surface, further confirming their surface origin.(Fig. 5.4) Contrasting temperature dependence of the electronic states at the X and at the Γ / Z points (topic of the present study described in this chapter) has also been observed in a recent ARPES study, where failure to appreciate the surface origin of the hole pocket has led them to erroneously consider this behavior as suggestive of an anisotropic 'hidden-order' parameter.[103] Thus in conclusion, though cannot be ascertained for certain dramatic response of the electronic states 2, 3 and 4 to the 'hidden-order' phase strongly suggests they are of bulk-origin or at the least are useful in identifying electronic fingerprint of the 'hidden-order' parameter.

5.3 Emergence of coherence and opening of Hybridization Gap at T_{HO}

Having identified the electronic states of interest we now address their evolution across T_{HO}. In what follows we will refer to the states corresponding to feature 3 ('M' shaped band) and feature 4 (flat band) as heavy fermion states and to feature 2 as the conduction band.

To investigate the heavy fermion states, we set $h\nu = 31\,\text{eV}$ (close to the Z point), a photon energy at which these states can be easily tracked. As shown in Fig. 5.5, above T_{HO} only diffuse spectral weight is observed close to the Fermi level, indicating large scattering rates. As the temperature is lowered below T_{HO}, a well-defined heavy fermion band forms, which becomes progressively sharper and more dispersive upon cooling. This development is even more apparent in the lower panels of Fig. 5.5, where the corresponding spectrum taken at 25 K has been subtracted. In more conventional Kondo lattice systems, coherent heavy fermion bands develop only gradually below the Kondo temperature T_K, which is generally assumed to be around 70 K for URu_2Si_2. In contrast, we observe only incoherent, localized states, consistent with recent optical spectroscopy measurements [153], which suddenly gain coherence below T_{HO}.

To better quantify this temperature dependence we have analyzed the energy distribution curves (EDCs) at the momentum indicated (red arrow) in Fig. 5.5 a). EDCs were fitted to a lorentzian plus a temperature-independent Shirley background [27], multiplied by a Fermi-Dirac function and finally convolved with the instrumental resolution. As can be observed in Fig. 5.6 b), the scattering rate obtained from the width of the lorentzian exhibits a sharp drop

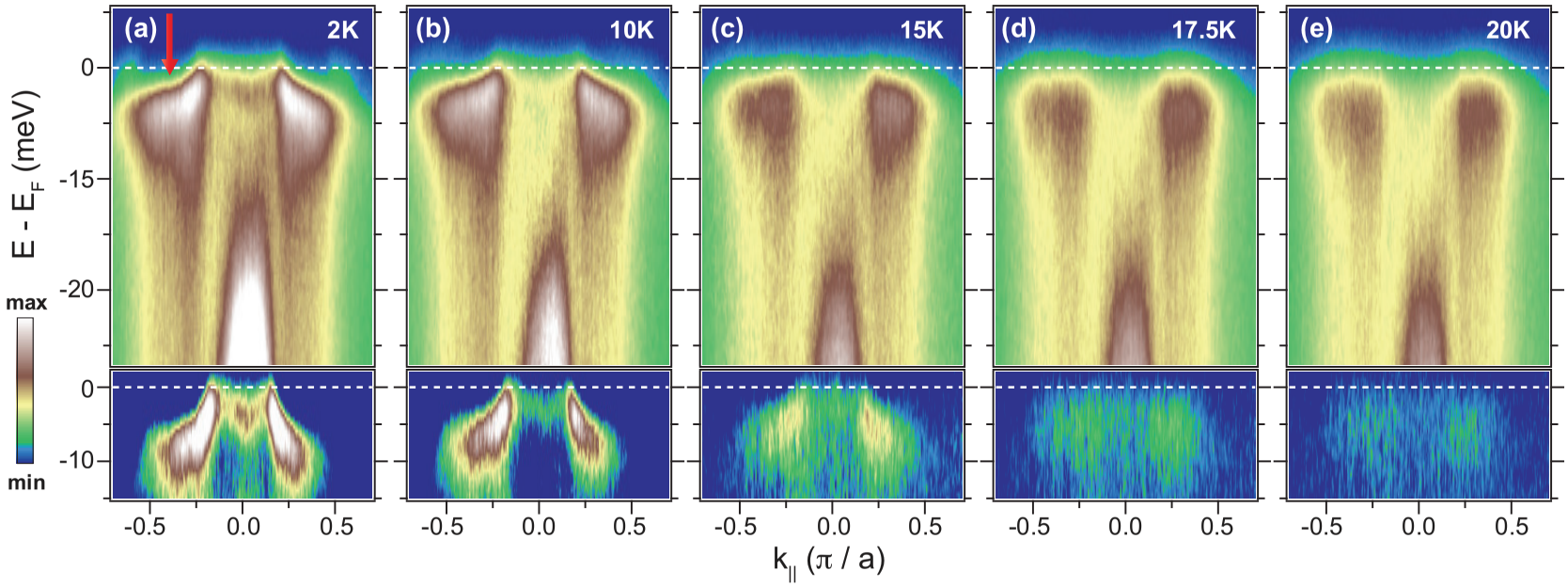

Figure 5.5: (a-e) Temperature evolution of the ARPES intensity plots of URu_2Si_2 measured along (0,0) - (π,0) at 31 eV photon energy over the temperature range 2-20 K. In the lower panel ARPES spectral maps obtained after subtracting the corresponding intensity map at 25 K is shown. Color scale has been adjusted to show only the positive part of the subtracted spectrum. Note that all the spectral maps in the lower panel are plotted keeping the range of the color scale fixed. Below T_{HO}, a coherent heavy fermionic band rapidly emerges that simultaneously becomes sharper and more dispersive as the sample is cooled down. The red arrow in (a) indicates the momentum at which the EDCs are taken, shown in Fig. 5.6.

precisely at T_{HO}. A similar temperature dependence has been observed in inelastic neutron scattering measurements, where the intensity of low energy spin excitations is greatly diminished upon entering the hidden order phase[96]. This indicates that the observed behavior stems from the same states that are probed here, another indication of their bulk-origin. Moreover, a decrease in the electronic relaxation rate upon entering the HO phase has also been reported in recent pump-probe experiments [154].

The development of dispersion is reflected in the shift in EDC peak position by approximately 4 meV (Fig. 5.6 c), which is consistent with optical spectroscopy [155, 156], transport [157, 158] and tunneling measurements [97]. We note that this energy shift tracks the typical temperature dependence of an order parameter, supporting the notion that the observed changes in the electronic structure are directly related to the hidden order parameter. Indeed, this suggests that the changes in the electronic density of states at the HO transition, which is often referred to as the hidden order gap is actually associated with the hybridization that gives rise to the heavy fermion states.

We now turn to the temperature dependence of the conduction band states across T_{HO}. For this purpose we set $h\nu = 49$ eV, where the signal from the conduction band is strongly enhanced. In Figs. 5.7 a-b), we compare spectra measured at 2 K and 20 K, revealing very strong changes in the conduction band across T_{HO} due to the hybridization between the conduction band and the incoherent U $5f$ states as they develop coherence. Our ARPES results are closely consistent with recent Fourier-transform scanning tunneling spectroscopy measurements that track quasiparticle interference patterns [74, 159]. This is established clearly in Fig. 5.7 c), where the difference between the spectra measured

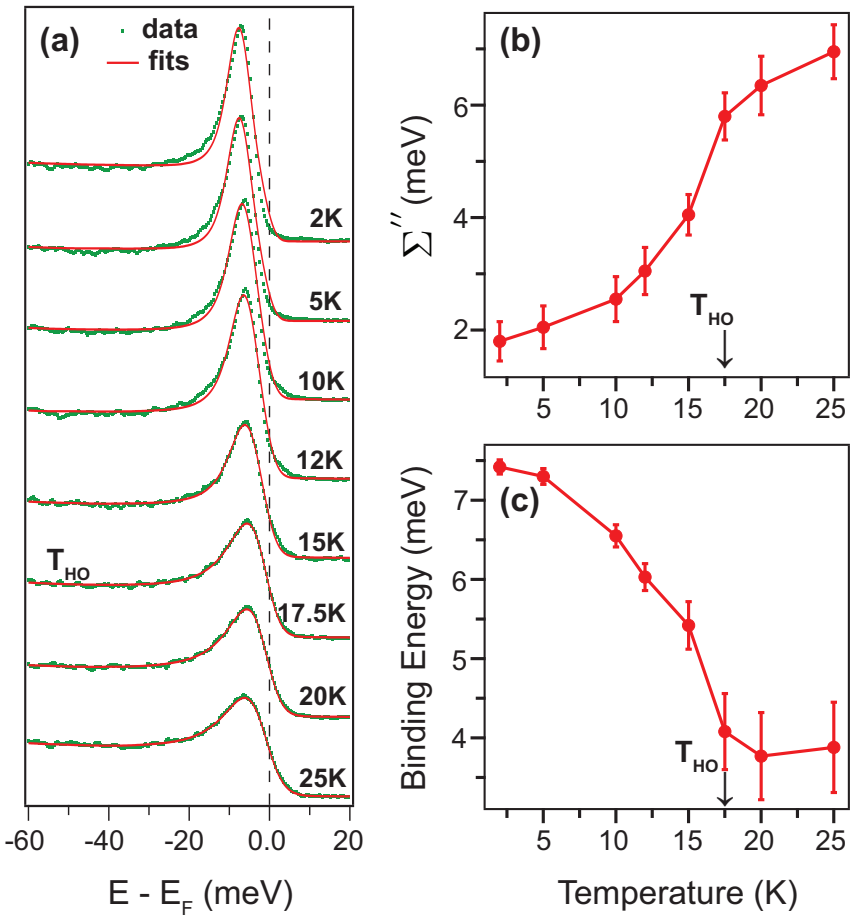

Figure 5.6: (a)Temperature dependence of the EDCs taken at the red arrow in Fig. 5.5(a), with corresponding fits (solid red lines). An instrumental resolution of 6 meV was used in the fits, as obtained from a gold reference. (b) Change in the imaginary part of the spectral function Σ'' and (c) quasiparticle binding energy with temperature as extracted from fits in **a**. A sharp drop in magnitude observed across T_{HO} shown in **b,** indicates a dramatic enhancement of the lifetime of the quasiparticles on entering the hidden order phase.

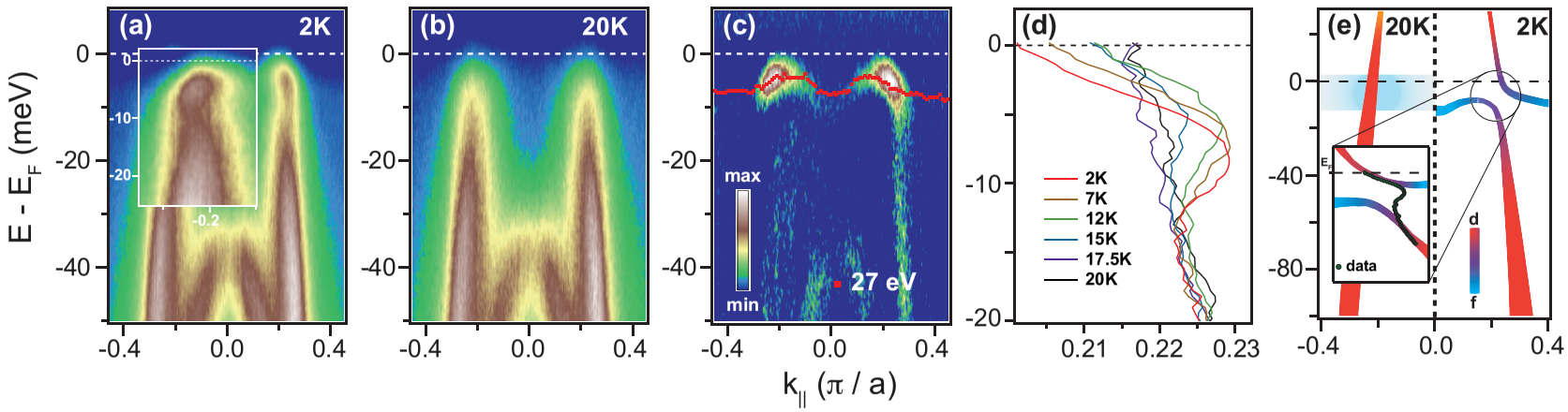

Figure 5.7: Direct obervation of opening of hybridization gap in the 'hidden-order' phase in URu_2Si_2. (a) Angle resolved spectra along the $(0, 0)$ to $(\pi, 0)$ direction for 49 eV photon energy below (a) and above (b) T_{HO}. Below T_{HO}, a break appears in the dispersion, shown more clearly in the inset of (a). (c) Spectral map obtained after subtracting data in (b) from (a)clearly shows additional spectral weight appears below T_{HO} as the conduction band hybridizes with U 5f states. Dispersion of the 'M' shaped feature as observed with 27 eV excitation energy (cf. Fig. 5.1 (b)) is plotted on top of the subtracted spectrum showing the additional spectral weight follows exactly the dispersion of the 'M' shaped feature. (d) Temperature dependence of the MDC derived dispersion of the conduction band. The kink feature progressively gets stronger and shifts towards higher binding energy as temperature is lowered below T_{HO}. (e) A schematic illustrating the changes in the electronic structure taking place across T_{HO}. Inset shows how a kink appears in the dispersion as the bands develop mixed orbital character.

at 2 K and 20 K is presented. The additional spectral weight below T_{HO} tracks exactly the dispersion of the 'M'-shaped feature establishing that the formation of the coherent heavy fermion liquid goes hand in hand with the hybridization of the conduction band. This situation is summarized schematically in Fig. 5.7 e), illustrating how variations in the photoelectron matrix elements due to rapidly changing orbital characters can give rise to an apparent dispersion anomaly as the bands hybridize.

Although the dispersion anomaly in Fig. 5.7 a) resembles a kink feature, we believe it is *not* related to the coupling of the quasiparticles to a bosonic excitation. Apart from the arguments given above, there are a number of additional reasons why electron-boson coupling is unlikely to be responsible for the observed kink in the dispersion. First, the 'kink' energy is characteristic of the boson energy, but is shown to be highly temperature dependent in Fig. 5.7 d), vanishing above T_{HO}. Second, the ratio of the band velocity at higher binding energies to that at E_F i.e v_{HBE}/v_{E_F} would be representative of the electron-boson coupling and mass renormalization, but the value of $v_{HBE}/v_{E_F} \approx 4.0 \pm 0.2$ at 2 K would signify an unphysically large value of the coupling strength, particularly for such a soft mode.

The emergence of the 'M' - shaped feature observed here at $h\nu$ = 49, 27, and 21 eV agrees well with previous laser ARPES studies at $h\nu$ = 7 eV [145, 146], and also with another recent experiment performed at BESSY by the same group[147]. There emergence of this feature is interpreted in terms of a symmetry reduction and the resulting zone folding in the HO phase. However, we would like to point out that the spectral weight arising from zone folding is typically much weaker than the original bands, whereas we observe that at certain

photon energies (e.g. 49 eV) the 'M' feature becomes as strong as the conduction band and the surface state. In addition, we have shown that this feature coincides with the dispersion of the coherent heavy fermion band below T_{HO}. Our experiments therefore indicate that the emerging 'M' feature is due to the formation of the heavy fermion liquid at T_{HO} arising from the hybridization, and not from zone folding. This again highlights the stark contrast in temperature dependence between the electronic states described here and the surface states around the X point that are insensitive to the *hidden order* transition in the bulk.

Because, a few contemporary ARPES measurements have claimed that their data support the notion of zone folding at T_{HO} we provide a critical evaluation of their data at this point. The claim is that the zone folding arises due to the reduction in translation symmetry along the c-axis as U atoms in the neighboring basal plane becomes inequivalent. This would result in a change in unit cell of URu_2Si_2 from body-centered tetragonal to simple tetragonal with a resultant reduction in the irreducible Brillouin zone, where in particular, high symmetry Γ and Z points of the original Brillouin zone would be expected to fold onto each other and become equivalent. This is what has been claimed to be happening at T_{HO}. In Fig. 5.8a) - d) we present data from Yoshida et. al., where they show spectral map along (0,0 - π,π) direction at the Γ (19 eV) and Z points (34 eV) both above and below T_{HO}. They identify the 'M'-shaped feature below T_{HO} for both the high symmetry momentum regions, but observe incoherent *f* spectral weight and contributions from feature 5 using a photon energy of 34 eV (close to the Z point) much more clearly than for a photon energy of 19 eV (close to the to Γ point) due to matrix element effect as we have described above and misconstrues it as an indication of the presence of an electron pocket at the Z point but not at the Γ point above T_{HO}. This leads them to propose an incor-

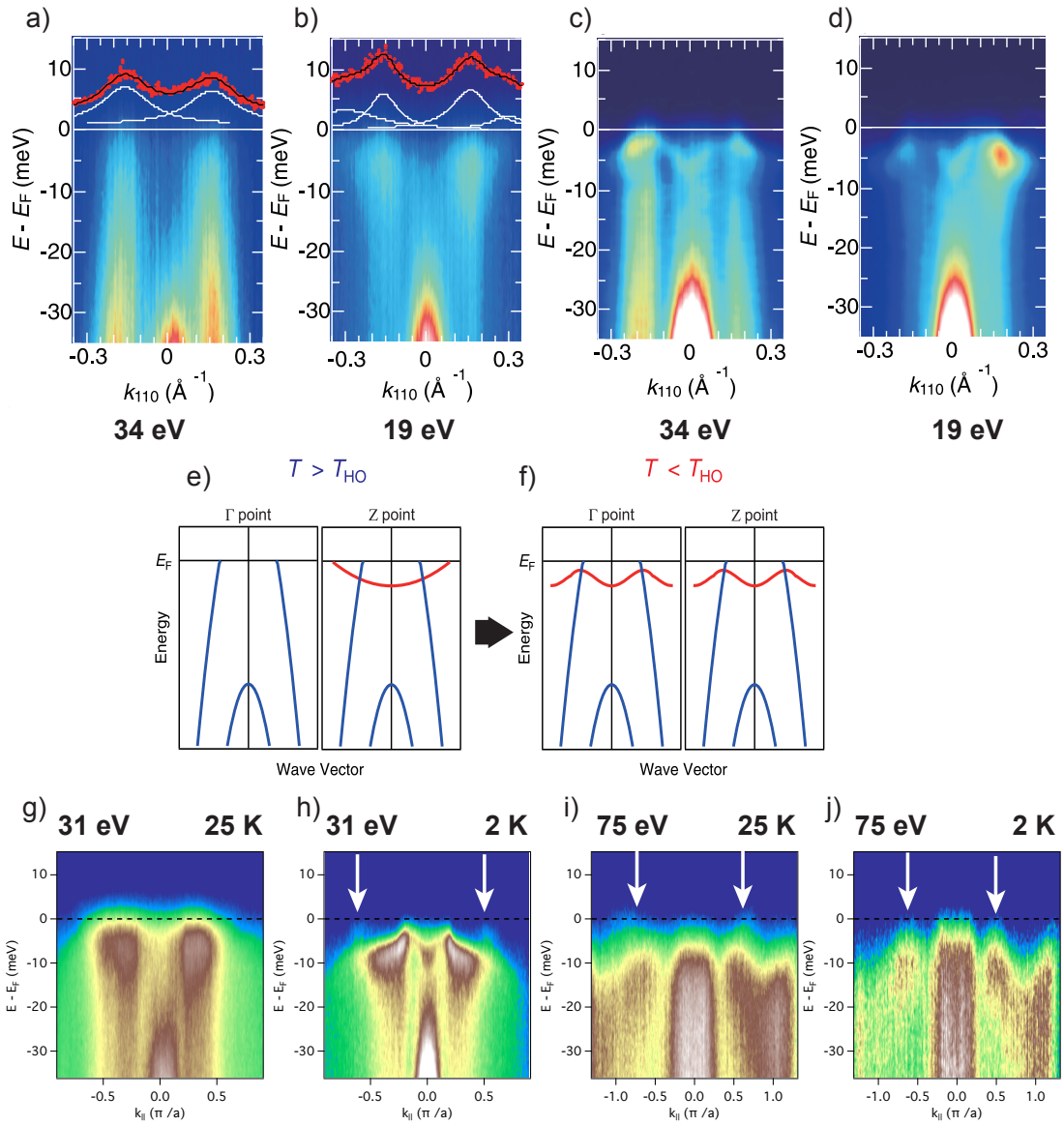

Figure 5.8: Absence of electron pocket at the Z point in URu_2Si_2 a)-d) Spectral intensity map along (0,0) - (π,π) as obtained in [147] for different excitation energies and temperature a) 34 eV, 20K b) 19 eV, 20K c)34 eV, 2 K d) 19 eV, 2 K. Proposed model by *Yoshida et al.* for the electronic structure around the Z point in URu_2Si_2 e) above T_{HO} f) below T_{HO}. Spectral intensity map along (0,0) - (π,0) taken at g) 31 eV 25 K h) 31 eV 2 K i) 75 eV 25 K j) 75 eV 2 K. Fermi crossings are identified by white arrows. Panels a) - f) adapted from [147]

rect model of the electronic structure changes at T_{HO}, illustrated in 5.8e) - f). In Fig. 5.8 g) - j) we show our own data along (0,0 - π,0) both above and below T_{HO} for photon energies 31 eV and 75 eV, both close to the Z point. Note in [147], electron pocket above T_{HO} at the Z point is not clearly observed at all. (Fig. 5.8 b)) Evidence for the presence of an electron pocket is taken from observation of a Fermi crossing at $k_{\|} \approx 0.3\text{Å}^{-1}$, which we show is due to the feature 5. Using spectral maps taken at excitation energy of 75 eV, which also corresponds to the Z point, shown in Fig. 5.8 i) and j), we clearly establish that the Fermi crossings identified by *Yoshida et. al.* is not due to an electron-like pocket centered at (0,0) but is due to the feature 5, a hole-like pocket centered around (π,0). Note, that at temperatures below T_{HO} the Fermi crossings are at smaller $k_{\|}$ values indicating increase in size of the hole pocket below T_{HO}, which again is an indication of the onset of hybridization below T_{HO}. Spectral maps using a photon energy 31 eV (close to the Z point) shows very similar features both above and below T_{HO} as is observed by *Yoshida et al.* But, a careful analysis also brings out the feature 5 in Fig. 5.8 j), (which should be the case as we are probing similar momentum region in k_z) but is weak in intensity due to matrix element effects. Thus above T_{HO}, for energies close to 31 eV feature 5 is not clearly identified, in contrast to 75 eV photons (Fig. 5.8 i)). Our measurements unambiguously establish that there is no evidence of a reduction in translational symmetry in the photoemission spectrum at the *hidden-order* phase transition in URu_2Si_2.

5.4 Discussion

Our experiments reveal that in URu_2Si_2, the formation of the coherent heavy fermion liquid occurs via a thermodynamic phase transition into the HO state,

in contrast to a gradual crossover below T_K, as is believed to be the case for other Kondo lattice systems. This indicates that there may exist multiple pathways to the formation of heavy fermionic quasiparticles, necessitating further studies of the electronic structure of additional f-electron systems. Furthermore, our measurements reveal that the putative hidden order gap observed in the electronic density of states by various probes is in fact associated with the hybridization which gives rise to the coherent heavy fermion quasiparticles. Our work reveals that the HO phenomenon is directly tied to the hybridization between the $5f$ states and the conduction band, an interaction which is blocked above T_{HO} and only becomes active inside the HO phase. Finally, the abrupt drop observed in the quasiparticle scattering rate through the HO transition suggests that the single particle electronic excitation spectrum is directly sensitive to fluctuations above T_{HO} and is indicative of an order-disorder transition.

CHAPTER 6

EPITAXIAL GROWTH OF $YbAl_3$ AND $LuAl_3$

6.1 Introduction

Kondo lattice systems are fascinating quantum materials that can host many different, and sometimes exotic ordered ground states, such as antiferromagnetism, hidden order phase, and unconventional superconductivity, as has been discussed in this thesis. Such ordered states can often be tuned by modest perturbations involving magnetic field and pressure, thus providing experimental access to a quantum critical point, for example in $YbRh_2Si_2$.[42] Ordered ground states in these systems emerge out of a complex Kondo screened many body state that is formed due to enhanced Kondo coupling between the rare earth *f* moments and the conduction electrons at low temperatures. In mixed valence systems, this also results in a change of the local rare earth valence.[47] But, the impact of this change in valence on low energy electronic structure and Fermi surface topology, which are crucial to gain insight into their emergent properties and *k*-space susceptibilities, has remained enigmatic. In this thesis, we attempt to answer this question. For this purpose, we have chosen to study a simple prototypical mixed valence system $YbAl_3$. In the next few sections, we describe general properties of $YbAl_3$ and the need to undertake an experimental approach that combines the techniques of Molecular Beam Epitaxy (MBE) and ARPES. In this chapter we provide a brief overview of MBE and describe our growth process of $YbAl_3$ thin films, achieved for the first time.

Much of the work described in this chapter has been published in S. Chatterjee *et. al., J Appl. Phys. 120, 035105 (2016)*

6.2 $YbAl_3$: A paradigmatic mixed valence compound

$YbAl_3$ is a binary compound having a cubic $AuCu_3$ - type structure with a modest mass enhancement (γ = 45 mJ /molK^2). Both core level spectroscopy and high energy photoemission measurements have established $YbAl_3$ to be in the mixed valence regime, where Yb valence is intermediate between Yb^{2+} (f^{14}) and Yb^{3+} (f^{13}).[160, 161, 162, 163, 164] Though absolute value of the Yb valence varies depending on the probe used, all such measurements predict that Yb valence decreases by $\approx$ 0.05 from room temperature to temperatures below $\approx$ 45 K. This is believed to be due to the enhanced Kondo screening of the Yb nuclear charge at lower temperatures.[28] In accordance with the strong mixed valence character shown by $YbAl_3$, the estimated best-fit single-ion Kondo temperature is predicted to be $T_K \approx 670K$, which is relatively much higher than most Kondo lattice systems.[165, 166] However, it should be noted that single-ion Anderson impurity model fails to satisfactorily reproduce observed temperature dependence of the physical properties in $YbAl_3$, including susceptibility, specific heat and resistivity, and also its photoemission spectrum, for any chosen parameter set, indicative of the importance of the lattice effects in this system.[32, 167] This is further established by the observation of another low temperature energy scale in this compound. In Fig.6.1 pronounced anomalies can be seen in the temperature dependence of both specific heat and magnetic susceptibility below T* $\approx$ 30 - 40 K, when $YbAl_3$ becomes a Fermi liquid.[32, 168] Furthermore, such anomalies can be suppressed above a critical field B* $\approx$ 40 T, which sets the low temperature energy scale as $k_BT^* = \mu_BB^* \approx$ 3 - 4 meV.[169] Such anomalous temperature dependence in thermodynamic quantities observed in the parent compound is readily suppressed by doping with Lu that disrupts the

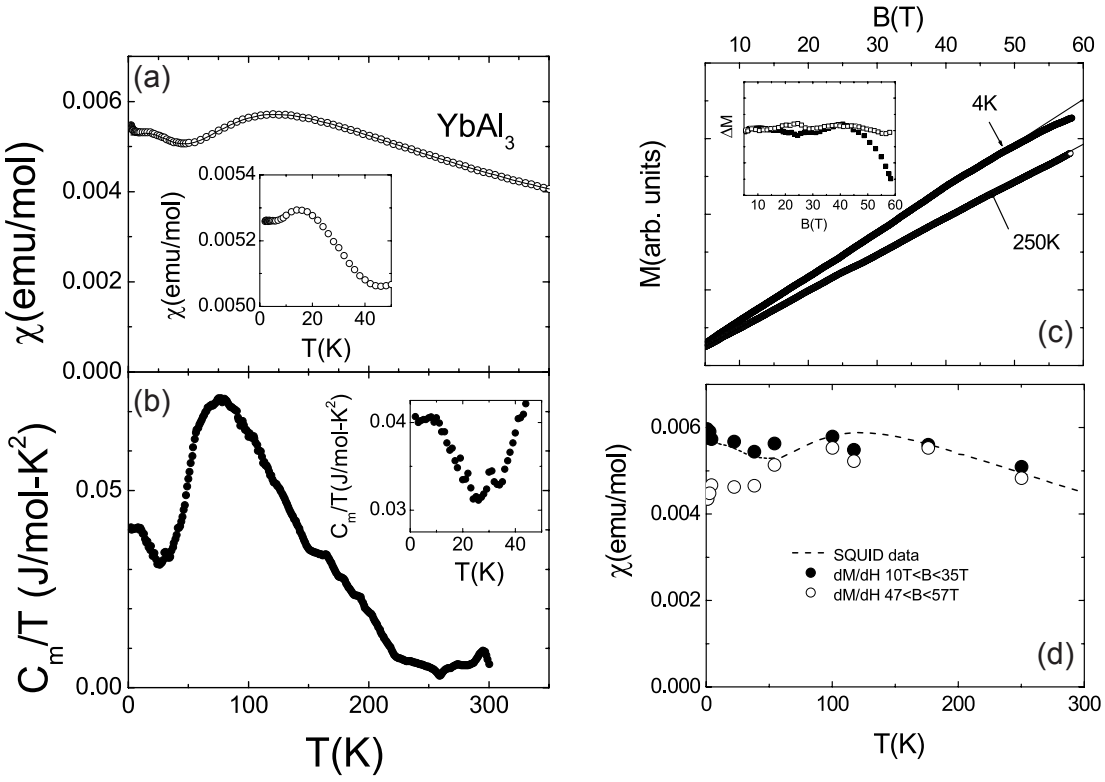

Figure 6.1: Signatures of the emergence of coherence in $YbAl_3$. Temperature dependence of a) susceptibility, b) specific heat, c) magnetization, and d) susceptibility in $YbAl_3$. Adapted from [32]

Yb sub-lattice in $YbAl_3$.[168] Accordingly, such anomalous temperature dependent properties are attributed to the development of coherence in Yb 4*f* states, and T* is known as the coherence temperature. Incredibly, effective masses of several quantum oscillation branches is reduced by a factor of 2 above the critical field B*, indicative of modification of the low energy excitations, probably accompanied with a change in Fermi surface topology, at the critical field strength.[169] It is noted that because of high Kondo temperature, field induced polarization effects are assumed to be negligible even at a field of 40 T. Attempts has been made to reconcile Fermi surface branches, as measured from deHaas-van Alphen at low temperatures, with the predictions from electronic structure

calculations. It was found that in order to achieve a fair agreement between the calculation and the experiment, Yb 4*f* states are required to be artificially shifted closer to the Fermi level leading to dispersive states with 4*f* character that contributes significantly to the Fermi surface and completely alters the Fermi surface topology.[170] Thus, experimental evidence suggests possible temperature dependent changes in the low energy electronic structure in $YbAl_3$ with significant involvement of the Yb 4*f* states.

6.3 Motivation for thin film growth

In the previous section, we discussed that $YbAl_3$ is strongly in the mixed valence regime. It has a simple crystal structure. Anti-ferromagnetic correlations in $YbAl_3$ are weak, with no reported long range magnetic order at any temperature. Energy scales in $YbAl_3$ are also much higher than other mixed valence compounds, with reported single ion Kondo temperature $T_K \approx 670$ K and a coherence temperature T* $\approx$ 34 - 40 K, below which it becomes a Fermi liquid.[166, 32] Thus, $YbAl_3$ is an ideal material system to investigate the subtle effects of Kondo screening and associated changes in the local Yb valence in the momentum space, and to gain a microscopic insight into its emergent properties, discussed in the previous chapter.

Angle-resolved photoemission spectroscopy (ARPES), being a direct probe of the momentum resolved electronic structure is an ideal tool for this purpose. However, lack of access to pristine sample surface due to difficulty in cleaving $YbAl_3$ single crystals have thus far precluded such measurements. In addition, attempts to measure fractured or scraped single crystals have been complicated

due to the presence of multiple crystallographic faces[171] and poor surface quality, coupled with a propensity of the $YbAl_3$ surface to form oxides.[172] One way of circumventing this difficulty is to synthesize phase pure, epitaxial thin films, and to measure their electronic structure *in situ* employing ARPES. In this chapter, we describe our efforts at epitaxial growth of $YbAl_3$ and its conventional metal analogue $LuAl_3$, making the first progress along this direction.[175] In $LuAl_3$, Lu $4f$ orbitals are fully occupied with zero net $4f$ moment and has a lattice constant (4.19 Å) similar to $YbAl_3$ (4.2 Å). Thus, $LuAl_3$ serves as an ideal reference compound to understand the properties of $YbAl_3$ emerging out of the Kondo interactions between the Yb $4f$ moments and the conduction electrons.

Furthermore, growing Kondo lattice systems in a thin film form opens up new avenues for dimensional confinement and strain engineering of the Kondo lattice[176], investigation of proximity effects,[177] and creation of tunable electronic states via artificial superlattice.[178] Due to the presence of carriers with strong spin-orbit coupling, heavy fermion thin films in general and $YbAl_3$, in particular because of its high Kondo temperature, are an attractive material system for potential spintronic applications. Additionally, $YbAl_3$ is also an intriguing candidate material for thermoelectric applications due to its high Seebeck coefficient of 90 μV / K, and the highest ever reported electrical power factor of 340×10^{-6} $Wcm^{-1}K^{-2}$ at 80 K. Unfortunately, its high thermal conductivity limits its zT factor, which is an order of magnitude lower than the best available thermoelectric materials.[179] Exploiting interfacial phonon scattering by synthesizing superlattices of $YbAl_3$ with another compound might be one possible way to increase its thermoelectric efficiency.

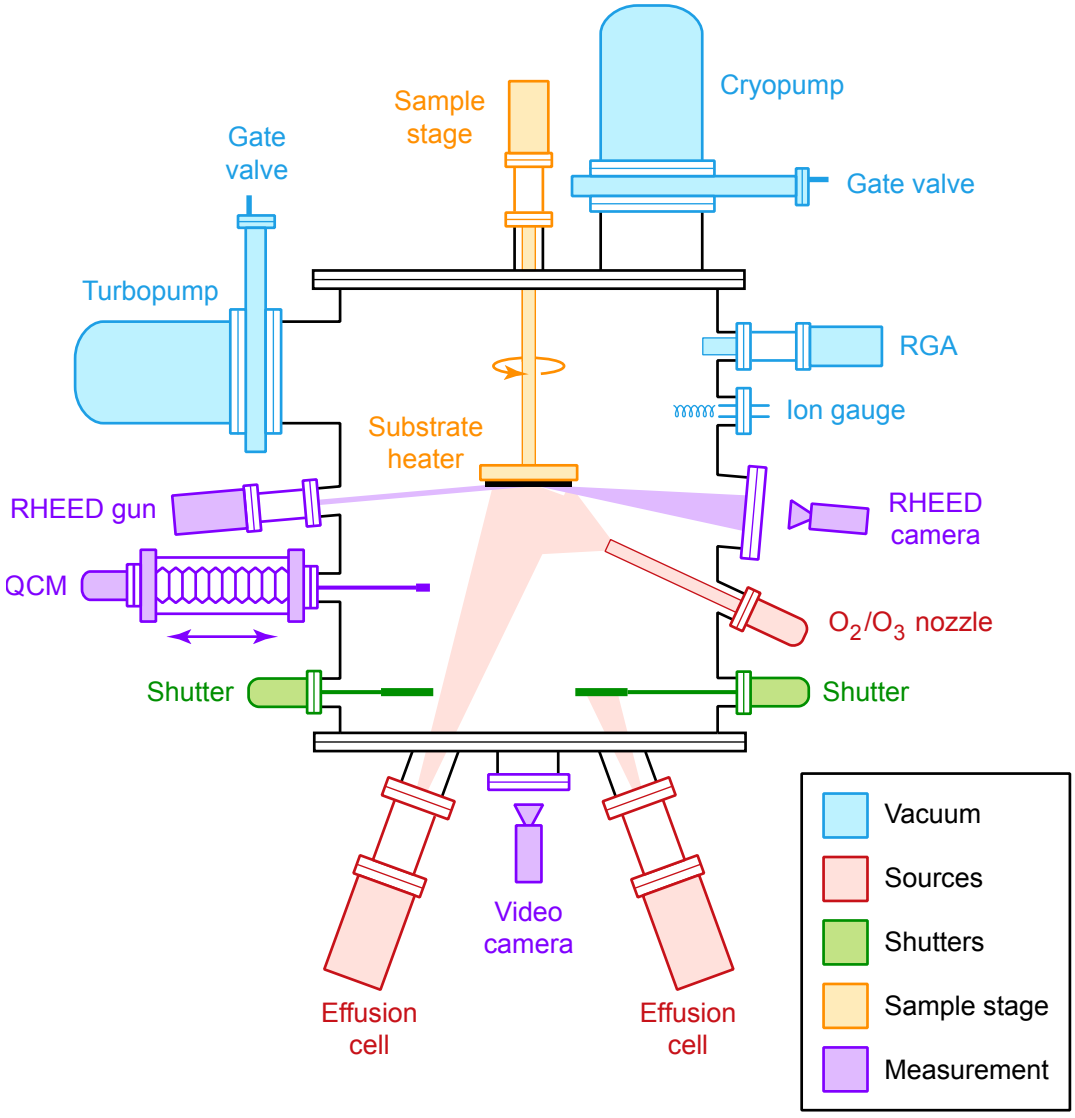

Figure 6.2: Schematic of the MBE system at Cornell University showing various components used during the growth process described here. Adapted from [180]

6.4 Introduction to MBE

We have grown thin films of both $YbAl_3$ and $LuAl_3$ using the technique of Molecular Beam Epitay (MBE). This technique allows fabrication of very high qual-

ity crystalline thin films with atomic layer precision in a bottom-up approach. Molecular beams in the ballistic regime are generated usually by thermal evaporation of constituent elements (for high vapor pressure elements energetic electron beam can be used) under ultra-high vacuum conditions, and are deposited on a heated substrate. Deposited elements rearrange themselves in registry with the underlying substrate forming high quality crystalline epitaxial layers.

The technique was developed by J.R. Arthur and A.Y. Cho at Bell laboratories in 1960s[181] to grow semiconductor thin films, which has now been extended to metals, oxides, chalcogenides etc.[182, 183, 184] Since its early years MBE has had significant impact both in the advancement of science and technology, including discovery of fractional quantum Hall effect[185], high electron mobility transistors[186], solid state lighting,[187] to name a few. In Fig.6.2, a schematic of the MBE equipment used for the current work is shown. In addition to components that are required to maintain vacuum, a typical MBE consists of source materials necessary for growth, and components necessary for *in situ* monitoring of growth or calibration of source fluxes. Though not used for $YbAl_3$ growth, our MBE chamber is equipped with a pure ozone source used for growing oxide thin films. Sample is heated with a silicon carbide heater than can reach temperatures in excess of 1000 °C and is resistant to oxidation. Our MBE chamber also has a cryoshroud that can be cooled using liquid N_2 to achieve lower background pressures during growth. It is particularly useful for growing metallic layers, such as $YbAl_3$, as it minimizes impurity concentration leading to high quality thin films.

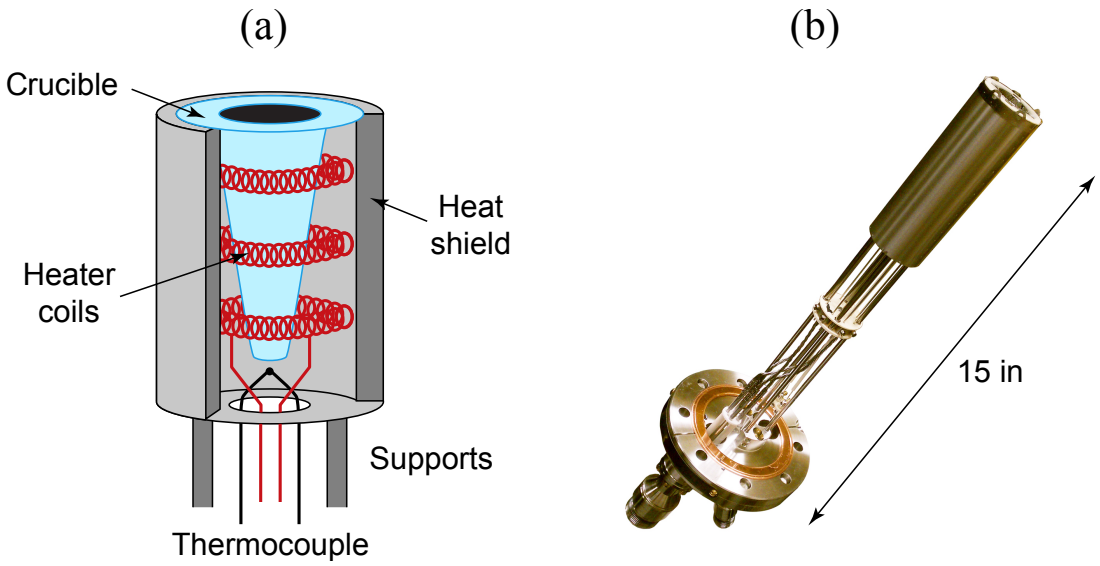

Figure 6.3: a)Schematic of a Knudsen effusion cell showing the heater coils, thermal shielding and the crucible that contains the source materials b) A Knudsen effusion cell from Veeco. Adapted from [180]

6.4.1 Knudsen effusion cell

Quality of the thin films grown by MBE is largely influenced by stability of the atomic sources and uniformity of flux distribution over the substrate surface area. Other desirable qualities are reproducibility, and lower operating temperature, so as to minimize outgassing. Effusion cells, both Knudsen[188] and Langmuir type, meets these requirements and are universally used in most MBE applications.[189, 190] These cells generally contain a conical crucible with a large exit aperture containing the element that is evaporated. The crucible is heated radiatively by tungsten or tantalum filaments, while its temperature is monitored by a thermocouple (Fig. 6.3). For higher flux stability, often dual filament cells are used, with heaters heating the evaporant element both at the base of the cell and also at the lip. Heater output is controlled by a PID loop that

uses temperatures recorded by the thermocouples as feedback. The operating temperature range for a particular element that can be used during growth, depends on its vapor pressure. As there is hardly any one-to-one correspondence between an element's vapor pressure and its melting temperature, a few of the elements are in a molten state at their growth temperatures. In Table. 6.1, melting point and growth temperatures for the elements used to grow $YbAl_3$ and $LuAl_3$ thin films are listed.

Table 6.1: MBE source temperatures

Element	Melting Point (°C)	Growth temp. (°C)
Aluminum (Al)	660.3	1035
Ytterbium (Yb)	818.8	450
Lutetium (Lu)	1663	1415

6.4.2 Quartz Crystal Microbalance

Quartz crystal microbalance (QCM) is used to calibrate source fluxes before starting film growth. A QCM uses an oscillating quartz crystal, the frequency of which is determined by its mass. Therefore, when atoms from the beam flux stick onto the QCM, it causes a frequency shift from which the rate of change of its mass can be determined, and can be directly related to the flux of the atomic beam. Geometrical factors causing a partial blockage in the line of sight of the beam or less than unity atomic sticking coefficient can lead to erroneous estimation of the flux value. However, these factors can be accounted for by es-

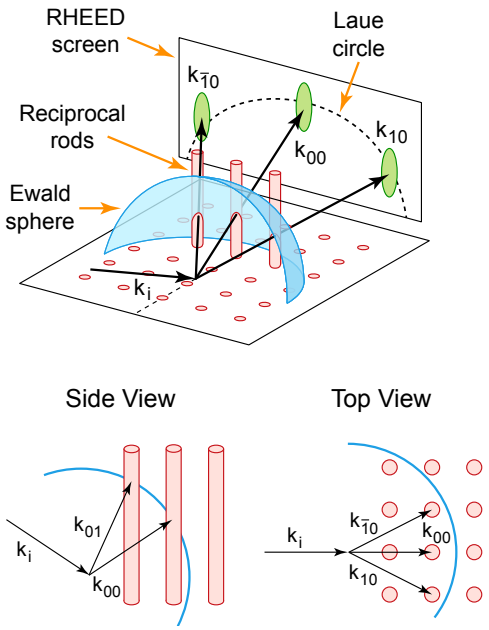

Figure 6.4: Schematic of the RHEED process

tablishing a *'tooling factor'*, which is determined based on atomic concentration mismatch between the measured value in a test film and that calculated from QCM.

6.4.3 Reflection High Energy Electron Diffraction

Reflection High Energy Electron Diffraction (RHEED) is a powerful *in situ* characterization technique that provides real-time information of the surface morphology during the growth process. Our MBE system is equipped with a RHEED setup containing an electron gun operating at 10 KeV, and a phosphor screen where the diffracted electrons are detected and imaged *ex situ* with a CCD camera. The setup, along with its principle of operation is illustrated in Fig. 6.4. The electron beam is diffracted from the sample surface at grazing incidence (typically $\approx 5°$) that results in surface sensitivity, as the electrons are now

diffracted only from the top-most layers. Therefore, in the reciprocal space it is expected to form features that are sharply resolved in (q_x, q_y), but not q_z, along which it forms long streaks. However, due to kinematic constraint imposed by the diffraction process, diffraction spot is obtained only when the Bragg rods intersect the Ewald sphere. Therefore, RHEED pattern in a perfect crystal should still show sharp spots that fall on the so-called *Laue circle*. In a real material, however, due to crystal imperfection, Bragg rods gets broader. Moreover, Ewald sphere is broadened due to finite divergence and energy spread of the electron beam. As a result, when the Bragg rods intersect the Ewald sphere, long streaks are formed along q_z, as shown in Fig. 6.7[192]

6.4.4 Interfacing ARPES with MBE

Traditionally, ARPES has been performed on single crystals that are either cleaved or fractured *in situ* under ultra high vacuum (UHV) conditions to access a pristine sample surface. While this approach has been very successful, and is still widely used, it has its own limitations. Firstly, as single crystals are usually very small in size ($\approx 1\text{mm}^2$), and does not always produce an uniform cleave, it is necessary to have a very small beam size to be able to pick a particular cleaved area with a single crystallographic orientation. Secondly, alignment of the sample surface is tricky due to small size of the single crystals that introduces significant error in precise estimation of physical quantities, such as Luttinger volume. But, most importantly, as this approach relies on the availability of single crystals, it limits the application of ARPES investigation only to thermodynamically stable phases that can be grown in a single-crystalline form, and are cleavable. Therefore, such an approach leaves a huge number of mate-

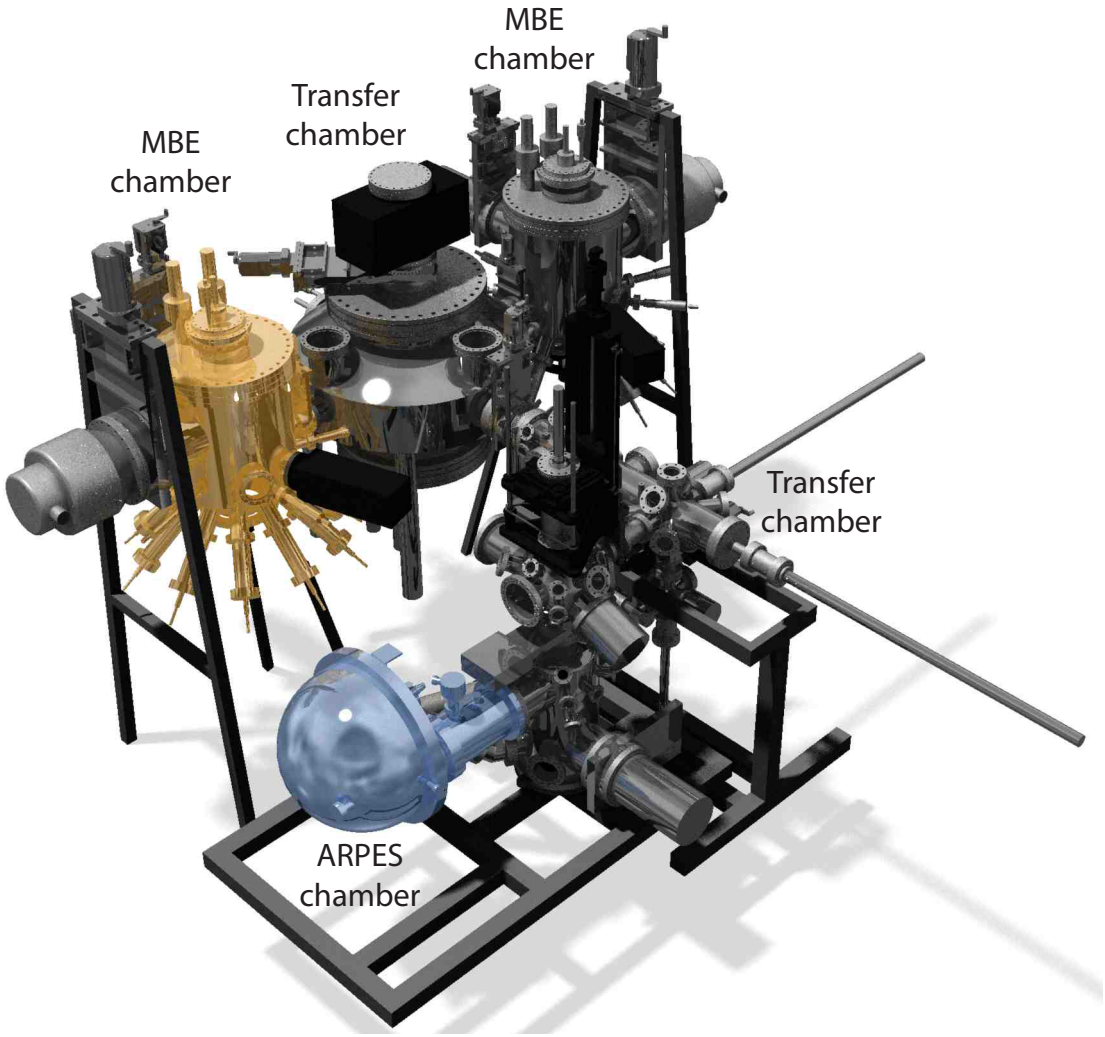

Figure 6.5: CAD rendering of a combined ARPES and MBE setup at Cornell University

rial systems outside its purview, such as Sr_2TiO_4[183] that cannot be grown in a single-crystalline form, and Sr_2RuO_3[191] that is not cleavable due to its three-dimensional nature etc.

On the other hand, MBE allows the possibility of growing these materials with atomic precision, which often allows fabrication of thermodynamic phases that are unstable in the bulk exploiting epitaxial stabilization. Furthermore, both MBE and ARPES being UHV techniques, a combination of the two with capabil-

ity to transfer samples without breaking the vacuum, offers unprecedented possibility of extending photoemission capabilities to systems that were hitherto outside its purview. With MBE, it is also possible to *engineer* materials by creating heterostructures[193], by applying substrate induced epitaxial strain[195] and by fabricating artificial superlattices[194]. Electronic structure of all such designer materials can now be investigated by ARPES. This approach holds immense promise in providing unique insights into the emergent physical phenomena at the interface, at low dimensions, under strain, in artificially created crystal environments etc., thus opening up exciting uncharted territories to explore. Substrates on which thin films are grown can be fairly large (several mm to even an inch or more), thus mitigating problems associated with small crystal size. In our group, we have been successful in overcoming the technical challenges involved in connecting these two techniques[196], which is the crucial enabling factor for performing ARPES measurements, for the first time, on $YbAl_3$ and $LuAl_3$ thin films.

6.5 Film Growth

6.5.1 Crystal Structure and Substrate Consideration

Thin films were grown on MgO substrates in a Veeco GEN10 MBE system with a liquid nitrogen cooled cryoshroud and a base pressure below 2×10^{-9} torr. We use aluminum (Al) as a buffer layer for growing $LuAl_3$ thin films, while employing both Al and $LuAl_3$ as buffer layers for growing $YbAl_3$ thin films. Both $YbAl_3$ and its structural analogue $LuAl_3$ crystallize in a cubic $AuCu_3$ (L12) structure,

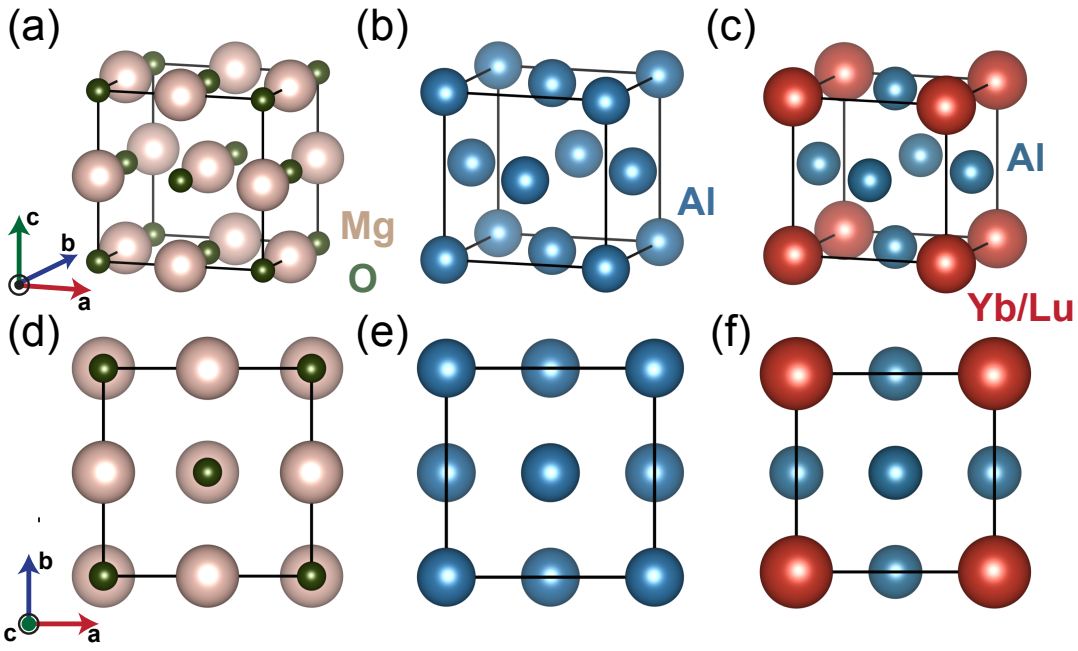

Figure 6.6: Crystal structure of (a) MgO, (b) Al, and (c) $YbAl_3$ / $LuAl_3$. Surface atomic arrangement of (d) MgO, oxygen sub-lattice shown in brown (e) Aluminum (f) $YbAl_3$ / $LuAl_3$

where Yb/Lu atoms occupy the vertices of the unit cell and Al atoms occupy the face-centered positions, as shown in Fig.6.6. Many compounds belonging to the same space group, such as $AuCu_3$, have been reported to show an order-disorder transition, where the disordered face-centered cubic (FCC) phase is stabilized above a certain temperature.[197] In the disordered FCC phase occupation probability of all the lattice sites becomes $\frac{1}{4}$ for Yb/Lu and $\frac{3}{4}$ for Al atoms. Diffraction measurements can distinguish the cubic ordered phase, as its diffraction peaks should be observed for all values of h, k, ℓ indices. On the contrary, in the disordered phase, the structure factor becomes zero when indices are mixed between odd and even h, k, ℓ.

Though, MgO and Al have a different space group ($Fm\bar{3}m$) than that of L12 $YbAl_3/LuAl_3$ ($Pm\bar{3}m$), the surface atomic arrangement of the oxygen atoms on

the (001) surface of MgO and the Al atoms on the aluminum (001) surface provide an excellent template for the epitaxial integration of $YbAl_3/LuAl_3$ on MgO substrates with aluminum as a buffer layer. Furthermore, lattice constants of MgO (4.21 Å) and Al (4.05 Å) are close to that of $LuAl_3$ (4.19 Å) and $YbAl_3$ (4.2 Å) that makes the epitaxial growth possible.

6.5.2 Growth Process

Prior to growth, MgO substrates were annealed in vacuum for 20 minutes at 800°C. The growth of the epitaxial (001) $YbAl_3$ films were achieved by first depositing a 1 - 2 nm thick aluminum buffer layer, followed by a $LuAl_3$ buffer layer on which $YbAl_3$ was grown. For the deposition of the $LuAl_3$ and $YbAl_3$, elements were co-deposited onto a rotating substrate from Langmuir effusion cells at a growth rate of $\approx$ 0.4 nm/min. During growth, *in situ* reflection high-energy electron diffraction (RHEED) was used to monitor the surface evolution. Aluminum buffer layer was deposited at a substrate temperature of 500°C. RHEED patterns taken after the deposition process shown in Fig. 6.7(b) reveal large transmission spots indicative of three-dimensional grains. Subsequently, a second buffer layer of $LuAl_3$ was deposited at a substrate temperature of 200°C and annealed in vacuum at 350°C for 30 minutes. As the $LuAl_3$ growth proceeded, individual grains coalesced into a flat surface,1‘ resulting into a two dimensional sharp and streaky RHEED pattern (Fig. 6.7(d)). Thicker $LuAl_3$ buffer layers and post-annealing resulted in better quality films. Finally, the sample was cooled down to 200°C for the deposition of the $YbAl_3$ layer. The growth temperature was ramped up to 315°C after initiating growth at 200°C. During growth, half-order peaks can be seen in RHEED images taken along the [100]

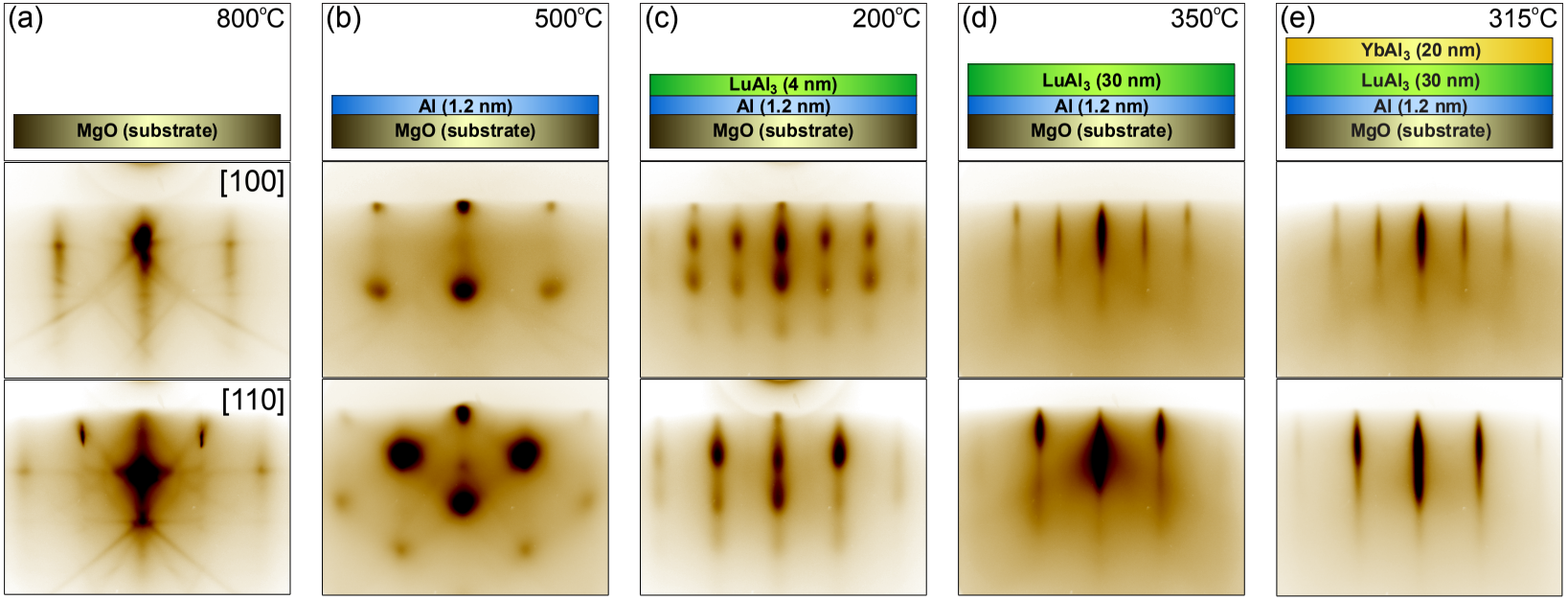

Figure 6.7: RHEED images at different stages of the growth of a $YbAl_3$ / $LuAl_3$ / Al / MgO heterostructure. (a)-(e) Schematics of the layers present in the thin film heterostructure at each stage of growth at which RHEED patterns were recorded. Substrate temperatures are noted in the top right corner of the top panel. Corresponding RHEED spectra along the [100] and [110] azimuths are in the middle and the bottom panels, respectively.

azimuth for both $LuAl_3$ and $YbAl_3$(Fig. 6.7(e)), indicating that they grow with the ordered L12 structure.

6.5.3 Importance of the Buffer Layers

Although, deposition of aluminum at elevated temperatures results in a rough surface, as observed in the RHEED image Fig. 6.7(b), this step is crucial for the fabrication of epitaxial, phase-pure $YbAl_3$ / $LuAl_3$ thin films. Growing $YbAl_3$ or $LuAl_3$ directly on MgO or depositing the Al buffer layer at a lower temperature resulted in a mixed orientation, where a secondary orientation with (111) $YbAl_3$ / $LuAl_3$ || (001) MgO was observed and the film surface becomes rough. This is due to the lower surface energy of the (111) metal surfaces that tend to preferentially stabilize (111) orientation.[198] However, by depositing Al at an elevated temperature we can take advantage of the increased kinetic energy of the Al atoms depositing on the MgO surface and a very strong Al-O bond strength (501.9 KJ / mol) to nucleate epitaxially oriented grains, where Al atoms are in perfect registry with the oxygen sub-lattice of MgO. However, poor wettability of Al at elevated temperatures leads to the formation of three-dimensional islands that can be mitigated by growing $LuAl_3$ over-layers at low temperatures (Fig. 6.7(c)). Use of $LuAl_3$ buffer layers in the growth process of $YbAl_3$ thin films was found to greatly increase the film quality because $YbAl_3$ layers grown directly on top of Al layers have higher tendency to form secondary phases (Fig. 6.8). This is understood in terms of smaller atomic size of Lu in comparison to Yb that has a favorable tolerance factor for the L12 phase in rare-earth trialuminides. Going along the rare-earths in the Lanthanide series it is found that only in the far right end of the periodic table (e.g. Er, Tm, Yb, Lu) $Pm\bar{3}m$ (L12)

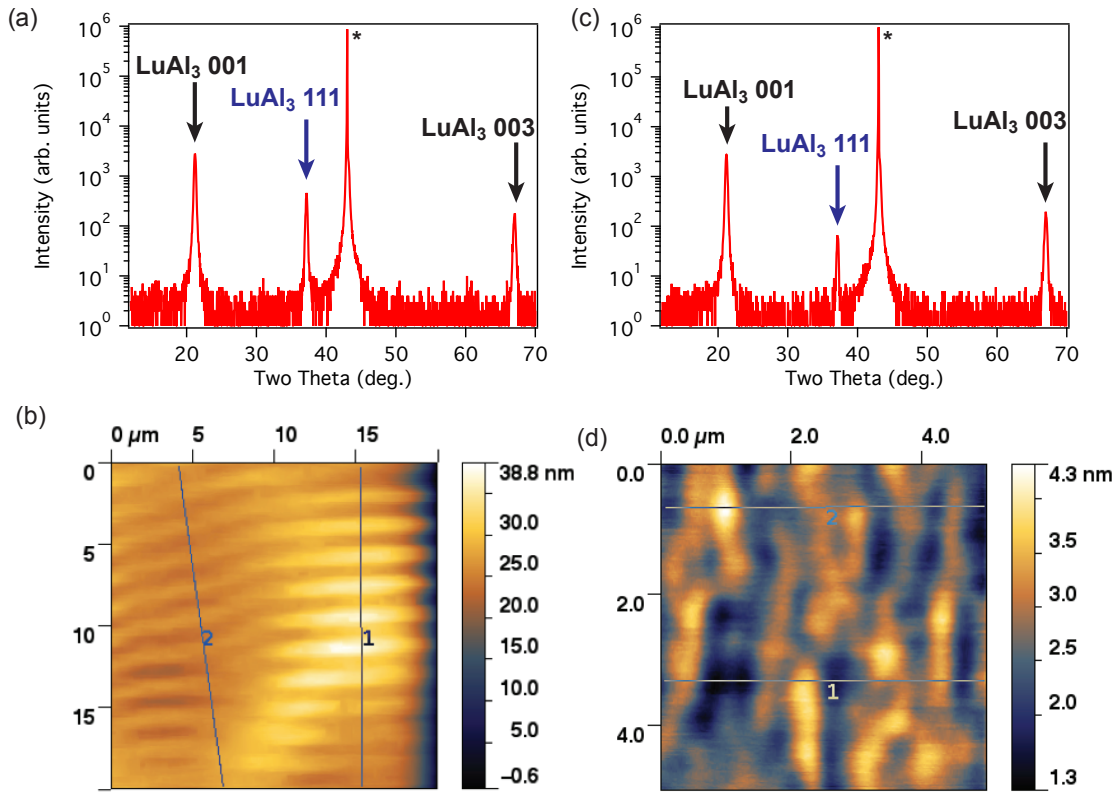

Figure 6.8: (a) Out-of-plane θ-2θ scan of a 25 nm thick $LuAl_3$ grown directly on MgO at 200 °C. 111 $LuAl_3$ diffraction peak can be clearly seen in addition to 001 and 003 diffraction peaks. (b) Corresponding AFM image showing ridge-like microstructures due to mixed phase. (c) Out-of-plane θ-2θ scan of a 25 nm thick $LuAl_3$ on an aluminum buffer layer, where the buffer layer is deposited on MgO substrate at 150 °C. (d) Corresponding AFM image still showing ridge-like microstructures though less pronounced than in (b). Substrate peaks are marked by asterisks.

phase can be stabilized in the bulk.[199]: Using $LuAl_3$ atomic layers as intermediate buffer layers, thus help stabilize the correct phase when growing $YbAl_3$ thin films.

6.6 Film Characterization

6.6.1 X-ray Diffraction

Bulk structural characterization of our thin films was done *ex situ* by four circle x-ray diffraction (XRD) using monochromatized Cu K_α radiation. In Fig. 6.9(a), we show an out-of-plane θ-2θ XRD scan. Prominent 001 and 003 Bragg peaks can be easily identified, confirming the films have the ordered L12 structure. 001 diffraction peaks of $YbAl_3$ and $LuAl_3$ overlap, which makes it difficult to directly estimate the contribution from each layer. Intensity of the 001 diffraction peak of films with different $LuAl_3$ and $YbAl_3$ layer thicknesses was measured to confirm that both $YbAl_3$ and $LuAl_3$ layers are ordered. Moreover, the observation of only 00ℓ film peaks establishes that our films are single phase with the desired (001) $YbAl_3$ out-of-plane orientation. An analysis of the peak positions reveal that the $LuAl_3$ layer is relaxed while $YbAl_3$ is strained to the underlying $LuAl_3$ layer. An azimuthal ϕ scan of the (110) $YbAl_3$ film peak is shown in Fig. 6.9(b). The ϕ scan in combination with the θ - 2θ scans establishes the epitaxial relationship of $YbAl_3/LuAl_3$ with respect to MgO where (001)[100] $YbAl_3/LuAl_3$ ||(001)[100] MgO. Rocking curve measurements were performed on the 001 film peak and the 002 substrate peak, shown in Fig.6.9 (c). The full width at half maximum (FWHM) of the the film peak was found to be 0.32 degrees, while that for the substrate peak was 0.03 degrees.

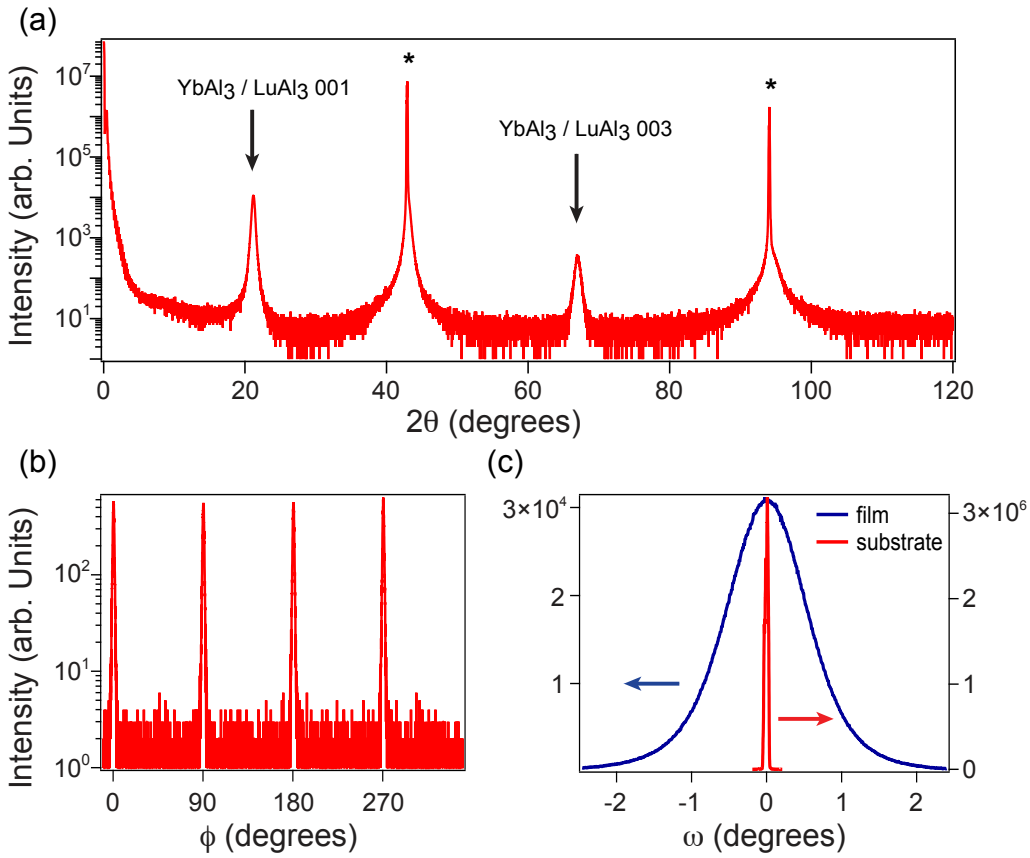

Figure 6.9: (a) Out-of-plane θ-2θ scan of a film with identical composition as in Fig. 6.11(e) and (f) but without a Ti capping layer. 001 and 003 peaks of the ordered L12 structure (shown in Fig. 1 (c)) establish that the film is ordered. Substrate peaks are marked by asterisks. (b) Azimuthal ϕ scan of the 101 $YbAl_3$ diffraction peak at $\chi = 45°$, where $\chi = 0°$ aligns the diffraction vector perpendicular to the plane of the substrate. $\phi = 0°$ corresponds to the in-plane component of the diffraction vector aligned parallel to the [100] direction of the (001) MgO substrate. The ϕ scan in (b) establishes the epitaxial relationship to be (001)[100] $YbAl_3$ || (001)[100] MgO. (c) Rocking curve comparison between the 001 film peak and 002 substrate peak.

6.6.2 Surface Characterization

Surface morphology was investigated by Low energy electron diffraction (LEED), atomic force microscopy (AFM) and scanning electron microcopy (SEM). Samples were transferred into the analysis chamber within 20 minutes after growth, without breaking vacuum at any point to obtain LEED images from a pristine sample surface.

In situ LEED patterns (Fig. 6.10(a)) indicate that the surface of the films is ordered where [100] diffraction spots can be clearly identified with no additional surface reconstruction. Film surfaces were found to be smooth over a wide area with no microstructures (Fig. 6.10(b)). Corresponding energy dispersive x-ray spectroscopy (EDX) measurements on a 35 nm thick $LuAl_3$ film with a 1.2 nm aluminium buffer shown in (Figs. 6.10(c)-(d)) reveal small aluminum-rich regions where excess aluminum has been precipitated out. This observation is in agreement with the Yb-Al phase diagram where we can find that at temperatures relevant to our study, a two-phase Al + $YbAl_3$ region exists.[200]. The expulsion of excess aluminum from the film ensures robustness of the growth method against slight flux mismatch, ensuring correct stoichiometry of our films. As formation enthalpy is lower for $YbAl_2$ than for $YbAl_3$, growing $YbAl_3$ thin films with a little excess Al flux ensures formation of $YbAl_3$ phase, where excess Al precipitates out.[200] The smoothness of the films is further confirmed by AFM measurements (Fig. 6.10(b)) with an rms roughness of only ≈ 1.8 over a 1 μm by 1 μm field of view.

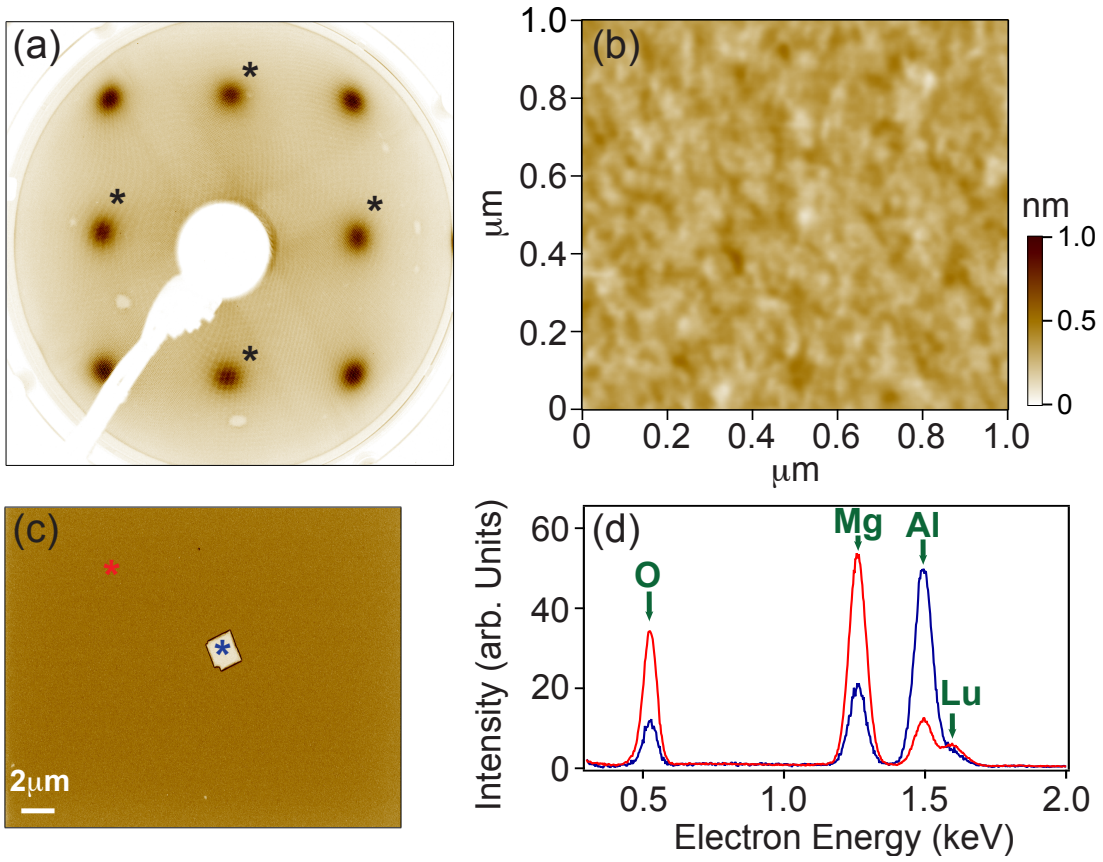

Figure 6.10: (a) LEED image taken on a 20 nm thick uncapped $YbAl_3$ film. Diffraction peaks with mixed indices are marked by asterisks. (b) AFM image of the same film. The measured rms surface roughness is ≈ 0.18 nm (c) SEM image of a 35 nm thick $LuAl_3$ film corroborating the smoothness of the films over a large area. (d) EDX scans taken in regions marked by asterisks in (c).

6.6.3 TEM and Anti-phase defects

The atomic scale structure of the $YbAl_3$ thin film was studied by aberration-corrected scanning transmission electron microscopy (STEM) and electron energy loss spectroscopy (EELS) performed on a FEI Titan Themis 300. Cross-sectional TEM specimen were prepared using a FEI Strata 400 Focused Ion

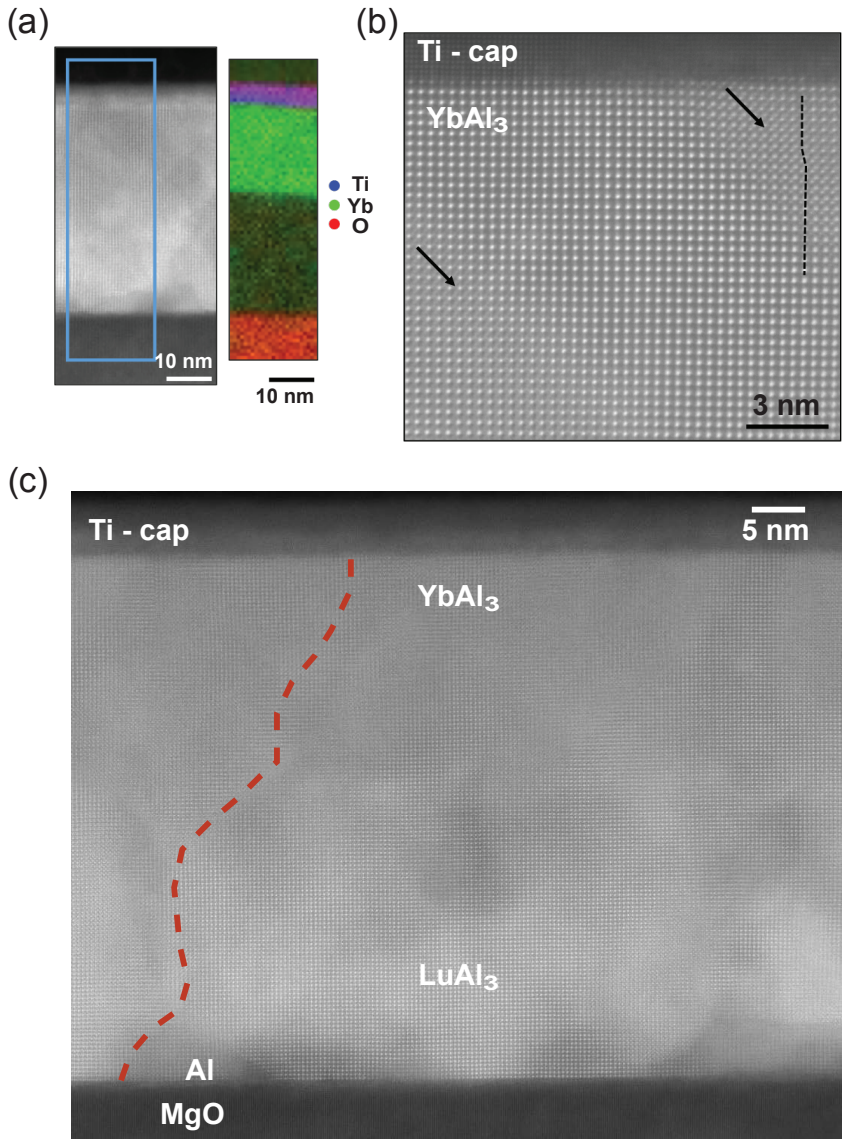

Figure 6.11: a)High resolution high angle annular dark field scanning transmission electron microscope (HAADF-STEM) image and elemental map of a 20 nm thick $YbAl_3$ film grown on 30 nm thick $LuAl_3$ and 1.2 nm Al buffer layers. The film is capped by 6 nm of Ti to protect the films from oxidation. EELS mapping was performed in the area marked in blue. b) HAADF-STEM showing the atomic arrangement of Yb atoms in $YbAl_3$ film. Anti-phase domain boundaries are highlighted with black arrows. Dotted black line shows the shift of Yb atomic positions by $(\frac{1}{2},\frac{1}{2},0)$ across an anti-phase domain boundary. c) Wide area cross-sectional image showing domain boundaries originating at the Al-$LuAl_3$ interface and propagating into the top layers. TEM measurements performed by Suk Hyun Sung.

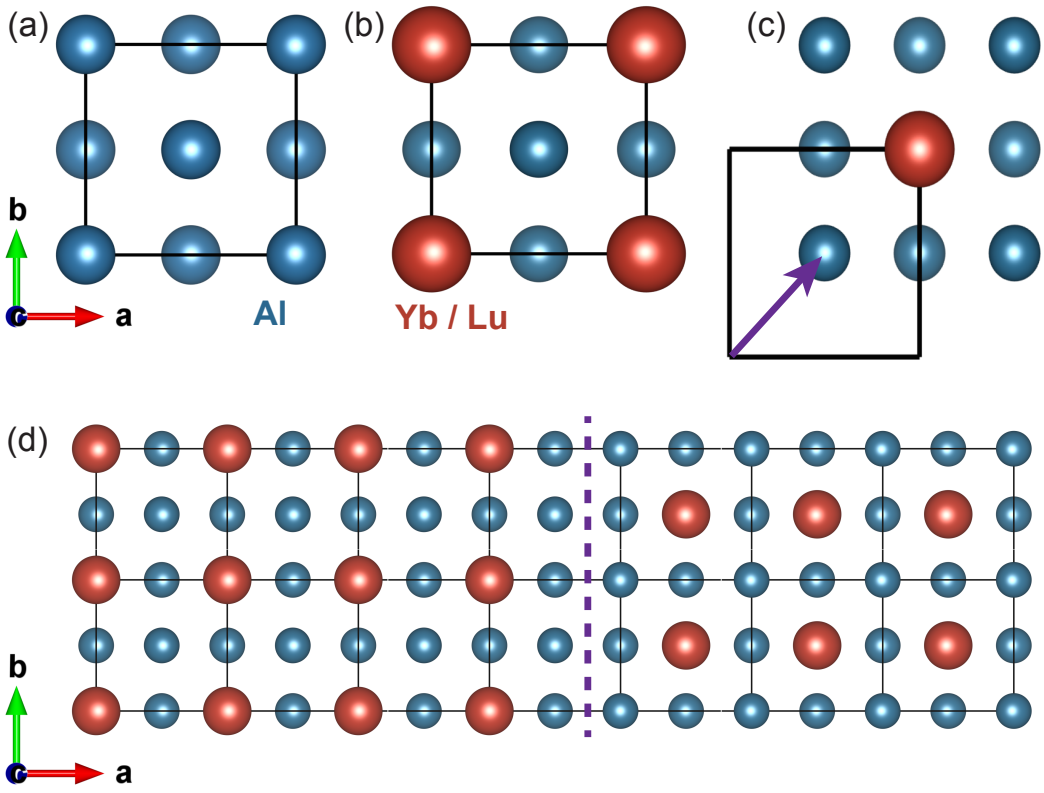

Figure 6.12: Surface atomic arrangement of (a) Al, (b) $YbAl_3$ / $LuAl_3$ and (c) $YbAl_3$ / $LuAl_3$ shifted by $(\frac{1}{2},\frac{1}{2},0)$. Illustration of two possible domains of $YbAl_3$ / $LuAl_3$ on Al when viewed along [001] direction and an anti-phase domain boundary (violet dotted line) between them.

Beam, with a final milling step of 2 KeV to reduce surface damage. Our TEM images reveal the high quality of our thin films with abrupt interface at the $YbAl_3$ - $LuAl_3$ boundary. However $LuAl_3$ - Al interface appears to be diffuse, as expected from our observation of three-dimensional RHEED pattern. Only major drawback in our thin films is the presence of anti-phase domain boundaries that are formed due to the reduced symmetry the of $LuAl_3$ / $YbAl_3$ layers compared to that of MgO or Al.

The face-centered sites and vertices are not equivalent for ($Pm\bar{3}$m) and thus,

the $LuAl_3$ / $YbAl_3$ layers can nucleate either where the $LuAl_3$ / $YbAl_3$ is in perfect registry with that of the Al unit cell (left domain in Fig. 6.11(d)) or where it is shifted by ($\frac{1}{2}$, $\frac{1}{2}$, 0) (right domain in Fig. 6.11(d)) leading to the formation of anti-phase domains (Fig. 6.11(d)). Thus, moving across an anti-phase domain boundary, one would expect to observe a shift in the lattice position of Lu /Yb by ($\frac{1}{2}$, $\frac{1}{2}$, 0) as observed in our TEM images. Furthermore, following any such domains it is observed that they start at the $LuAl_3$ - Al interface, as expected. Growing on suitable substrates with identical crystallographic space group as that of $YbAl_3$ / $LuAl_3$ would mitigate this problem. Unfortunately, currently such substrates are commercially unavailable which will probably be addressed in the future. Moreover, our EELS map confirms that there is negligible inter-diffusion across the boundary between the $YbAl_3$ and $LuAl_3$ layers.(Fig. 6.11(e)).

6.6.4 Resistivity

Having investigated the structural aspects of our thin films, we now turn to their electronic properties. Four-point resistivity measurements were performed in a van der Pauw geometry using both a home-built dipper setup and a Quantum Design PPMS system. The temperature-dependent resistivity for a 20 nm $YbAl_3$/ 1.6 nm $LuAl_3$/ 1.2 nm Al and 35 nm $LuAl_3$/ 1.2 nm Al thin films are shown in Figs. 6.13(a) and 6.13(b), respectively.

The resistivity curves are found to be qualitatively similar to those of single crystals.[201] The resistivity of $YbAl_3$ is plotted as a function of T^2 in the inset of Fig. 6.13(a), which shows that the film deviates from T^2 Fermi liquid behavior ($\rho(T) = \rho_0 + AT^2$) above $T^* \approx 37$ K, similar to single crystals,[32] albeit with a

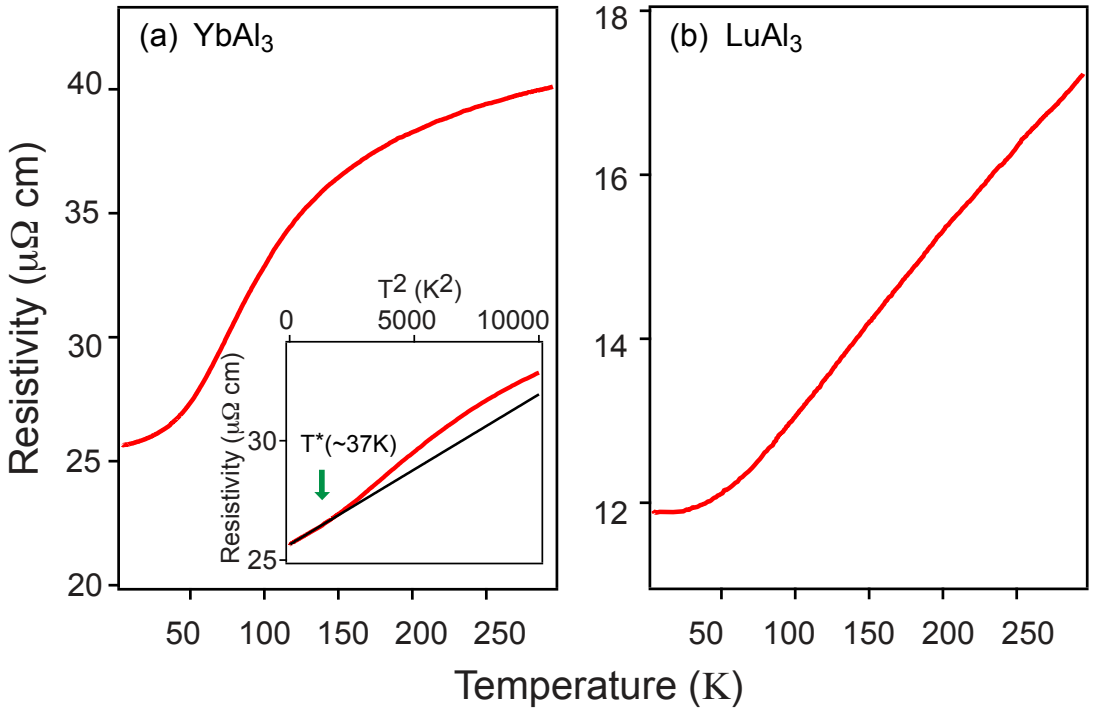

Figure 6.13: Temperature dependence of resistivity of (a) 20 nm $YbAl_3$ / 1.6 nm $LuAl_3$ / 1.2 nm Al and of (b) 35 nm $LuAl_3$ / 1.2 nm Al. Inset in (a) shows the onset of coherence at ≈ 37 K in the 20 nm thick $YbAl_3$ film above which the resistivity starts to deviate from T^2 behavior. (black line)

lower residual resistivity for the single crystals. The roughness of the aluminum buffer layer employed at the beginning of the growth process and the presence of anti-phase domain boundaries, as seen in TEM (Fig. 6.11), could be potential contributors to both the higher residual resistivity and wide rocking curves (Fig. 6.9(c)) of our thin films. The T^2 coefficient of resistivity in our thin films is A = $6\times10^{-4} \pm 1\times10^{-4}$ $\mu\Omega$ cm/K^2 and are similar to the earlier reported values for single crystals.[202, 203] Assuming a similar value of γ = 45 mJ/mol K^2 in our thin films as in single crystals, we obtain a Kadowaki Woods ratio (A/γ^2) of ≈ 3×10^{-7} $\mu\Omega$ cm mol^2 K^2/mJ^2, which is orders of magnitude lower than the

universal behavior observed in many *f* electron systems, $A/\gamma^2 = 1\times10^{-5}$ $\mu\Omega$ cm mol^2 K^2/mJ^2.[204] This apparent discrepancy can be reconciled by incorporating corrections assuming full degeneracy N = 8 fold degeneract of the Yb 4*f* *J* = 7/2 manifold in the ground state that gives a value of $A/\gamma^2 = 3.6\times10^{-7}$ $\mu\Omega$ cm mol^2 K^2/mJ^2. [205] Results from our transport measurements are consistent with neutron scattering experiments where no sharp crystal electric field excitations are observed due to degeneracy of the crystal electric field levels in the ground state.

CHAPTER 7

ELECTRONIC STRUCTURE OF $YbAl_3$ AND $LuAl_3$

Kondo lattice materials present an exotic materials system where peculiarities in the low energy electronic structure can stabilize multitudes of different ground states. In these multi-band systems, it is crucial to distinguish and delineate contributions from individual electronic states in order to obtain a microscopic understanding of their properties. Advanced spectroscopic probes such as ARPES, with its unique momentum resolving capabilities can be extremely beneficial in this regard.[15] In this chapter, we will describe experimentally observed k - resolved electronic structure of $YbAl_3$ and $LuAl_3$ thin films, and compare our results with the predictions from density functional theory calculations. Our results establish the feasibility of combining high quality synthesis with *in situ* ARPES in a Kondo lattice system, thus opening the door for future advanced spectroscopic investigation of systems that are difficult to cleave or even artificial f electron heterostructures.

7.1 Electronic structure calculations

Density functional theory[206] calculations are carried out using a full-potential linearized augmented plane wave method (LAPW), with PBE-GGA[207] functionals for exchange potential as implemented in the WIEN2k code.[208] Scalar relativistic effects and spin-orbit interactions are taken into account for all electrons. Spin-orbit interactions for valence electrons are calculated in a self-consistent manner using second variational procedure. We added on-site Coulomb repulsion U for 4f electrons to take into account their strong correlations. A value of U = 2.08 eV was chosen for $LuAl_3$, to match the simulated Lu 4f

core levels with those of our ARPES experiment. For $YbAl_3$, determining a value of U is tricky as DFT+U approach cannot adequately describe valence fluctuation in $YbAl_3$.[209] Furthermore, it has been shown to perform poorly for many Kondo lattice systems that contain a partially filled *f* shell, both in the mixed valence and heavy fermion regimes, and in particular, for $YbAl_3$. Nevertheless, we perform calculations both with and without U to understand the systematics of the changes in DFT predicted band structure with U, as is discussed later. Calculations are done to a convergence in energy and charge of 1 meV and 0.001 e^- per unit cell. Both $LuAl_3$ and $YbAl_3$ crystallizes in a cubic structure with space group $Pm\bar{3}m$, which has 48 symmetry operations. Eigenvalues are calculated at 356 different *k* points, uniformly distributed in the irreducible 1/48 of the Brillouin zone.

Computed electronic structure along several high symmetry directions of the $LuAl_3$ Brillouin zone is shown in Fig. 7.1. Calculated three-dimensional Fermi surface is shown in Fig. 7.2. Two bands form the Fermi surface in $LuAl_3$. One of them forms a multiply connected Fermi surface centered at Γ with elongated arms along each of the six equivalent Γ - X directions. The other band forms an electron pocket centered at the R point. Fermi surface for $YbAl_3$, obtained from similar calculations without adding any U, is shown in Fig. 7.3. An additional band now crosses the Fermi level which forms closed hole pockets along eight symmetric body diagonal directions of the Brillouin zone along Γ - R. (Fig. 7.3 c). The electron pocket around the high-symmetry R point, as seen in $LuAl_3$, is also present in $YbAl_3$. But, the multiply connected Fermi surface centered at Γ in $LuAl_3$ undergoes a significant change in $YbAl_3$. Now, it consists of two surfaces, a closed electron pocket centered at Γ and another surface extending along six symmetric directions of the Brillouin zone along Γ - X.

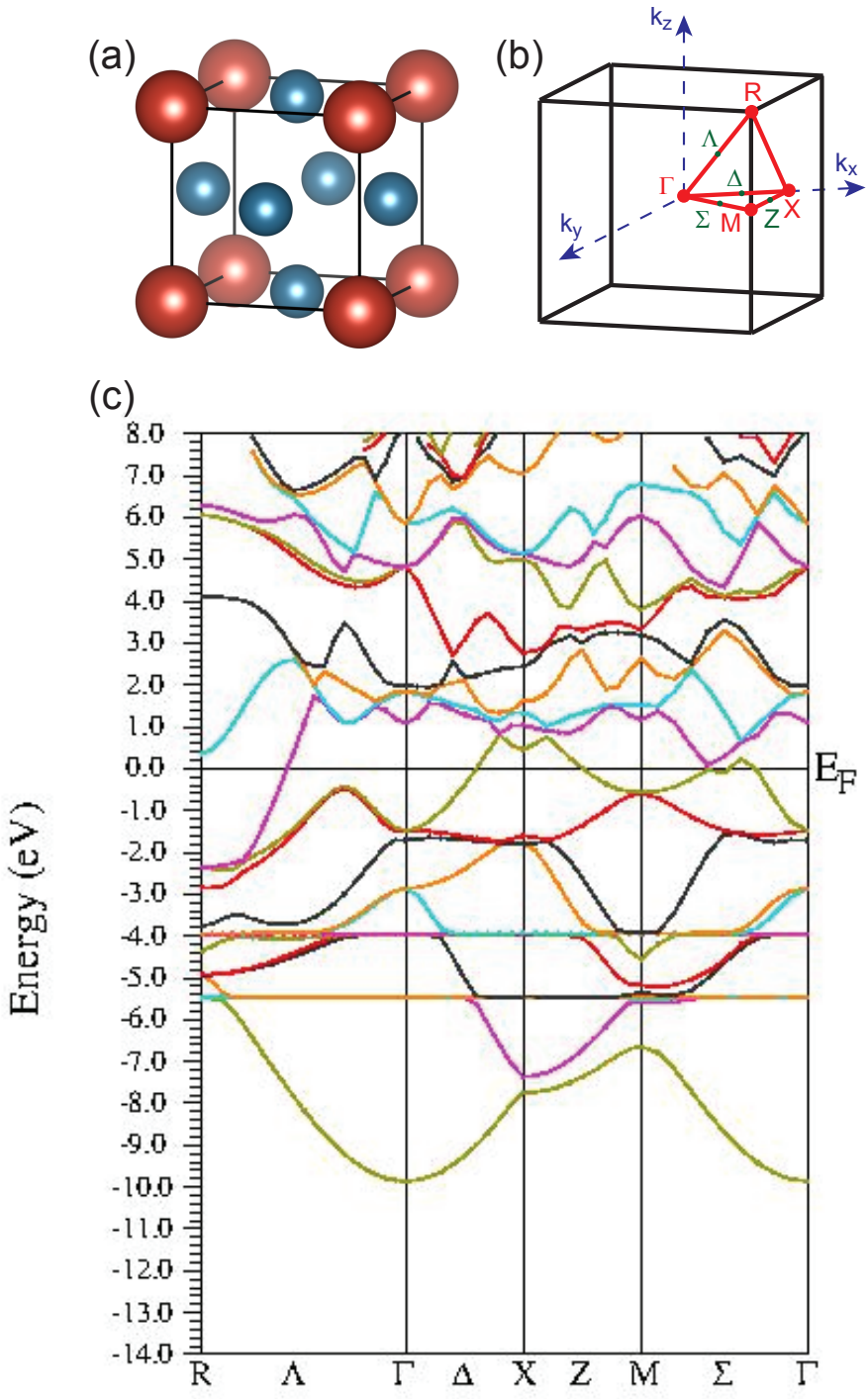

Figure 7.1: a) Crystal structure of $LuAl_3$ / $YbAl_3$ b) Corresponding Brillouin zone c) Spaghetti plot showing calculated electronic band dispersion in $LuAl_3$

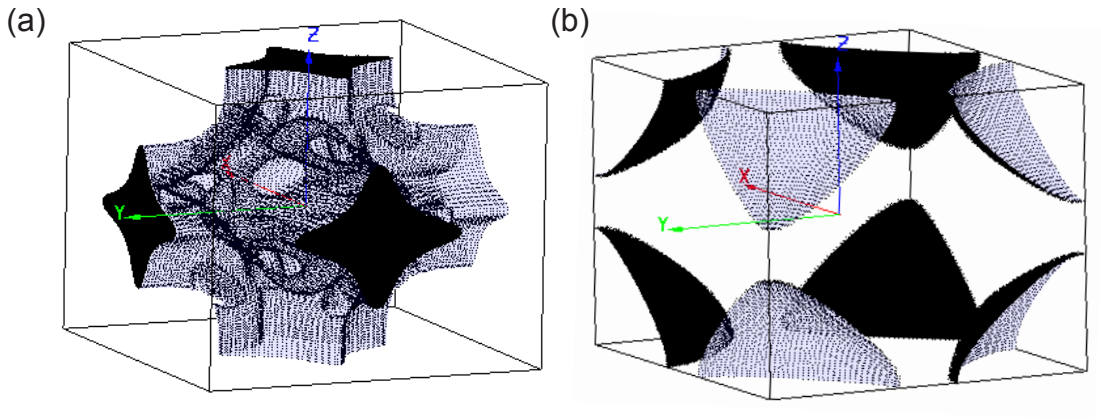

Figure 7.2: a) and b)Two Fermi surface sheets that form the Fermi surface in $LuAl_3$

We have performed LDA + U calculations for $YbAl_3$, with U = 5.44 eV (0.4 Ry). U value is chosen following many reported work on Yb Kondo lattice systems, where the chosen Hubbard U varies between 4 and 6.5 eV.[210] However, it is noted that no additional significance is attached to the correctness of the chosen U value, our purpose here is only to establish systematics in the effect of adding Hubbard U on the electronic structure, particularly on the Yb 4*f* derived states and Fermi surface topology in $YbAl_3$. As expected, addition of U pushes the Yb 4*f* J=7/2 and J=5/2 core-levels to higher binding energy that results in a significant change in the Fermi surface topology seen in Fig. 7.3, particularly, an increase in size of the electron pocket at Γ. A comparison of the two-dimensional Fermi surfaces centered at Gamma and band dispersions along the Γ - X direction for three different situations viz. $LuAl_3$ with U = 2.08 eV, $YbAl_3$ with U = 5.44 eV and $YbAl_3$ without U reveal a reduction in the size of the pocket centered at Γ from $LuAl_3$ to $YbAl_3$; the size of which in $YbAl_3$ is sensitive to the positions of the Yb 4*f* J = 7/2 and J = 5/2 levels, shown in Fig. 8.12. Quantum oscillation measurements at low temperatures in $YbAl_3$ single crystals indicates that the Yb

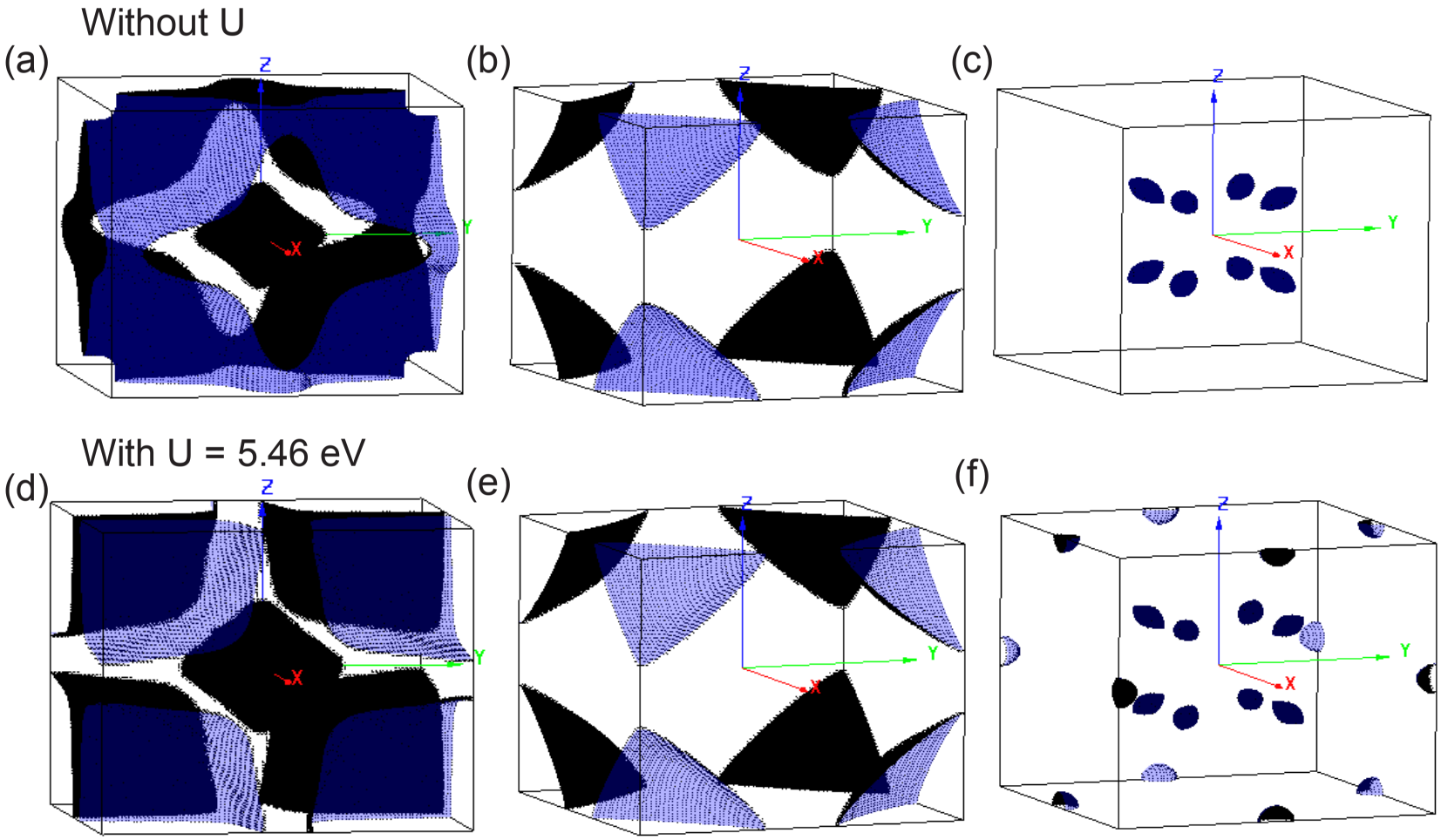

Figure 7.3: Three Fermi surface sheets that form the Fermi surface in $YbAl_3$. a)-c) as calculated without U (itinerant 4*f*) d)-f) with U (localized 4*f*)

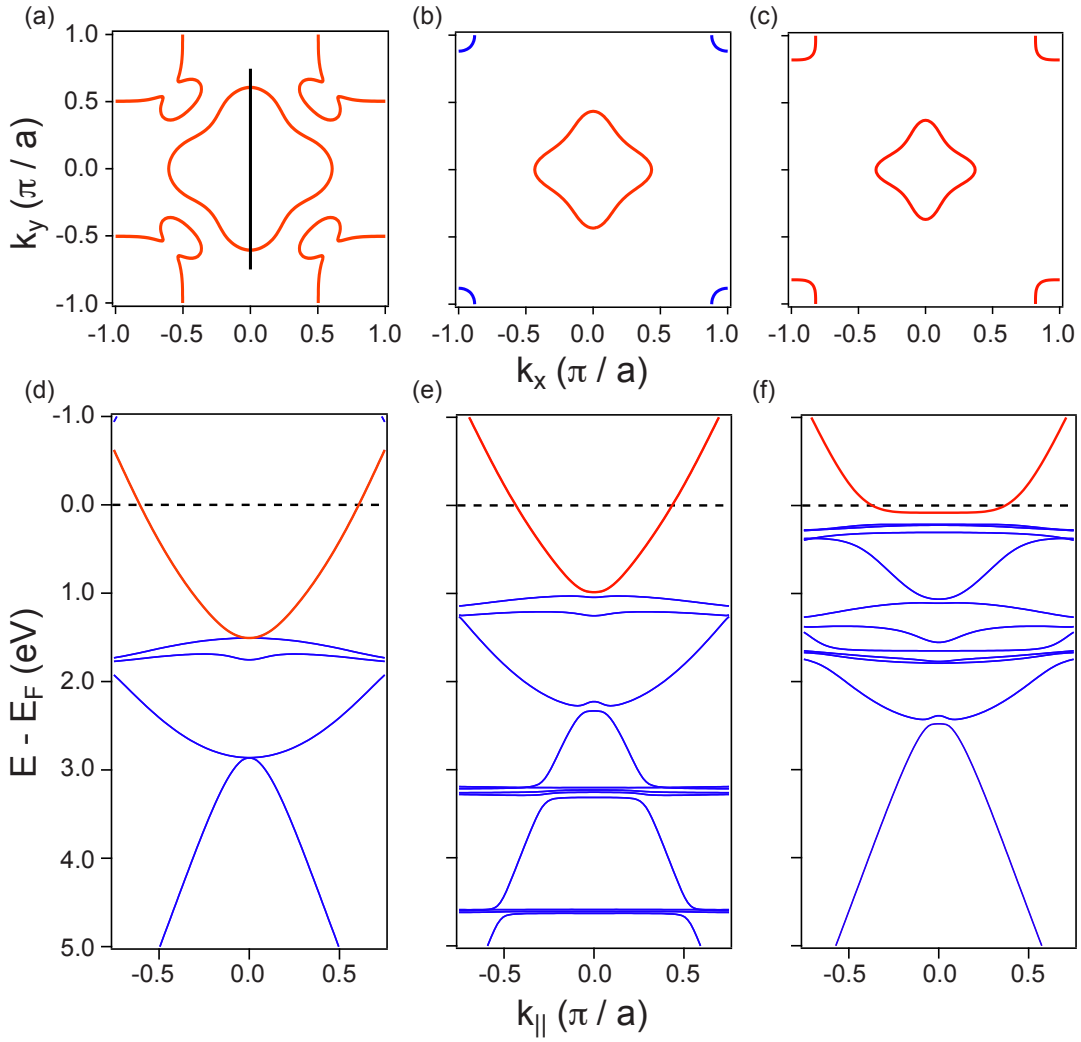

Figure 7.4: Evolution of the electronic structure from $LuAl_3$ to $YbAl_3$. Two-dimensional projection on the k_x - k_y plane of the calculated Fermi surface centered at Γ of a)$LuAl_3$ with U = 2.08 eV b)$YbAl_3$ with U = 5.46 eV c)$YbAl_3$ without U. d) - f) Corresponding energy-momentum spectral map along a cut indicated by the black line in a). Note the change in size of the electron pocket centered at (0,0)

4*f* levels needs to be artificially shifted to lower binding energy that pushes the electron pocket at (0,0) above the Fermi level to get a fair agreement with the DFT calculations. [170]

Thus, knowledge of the binding energy of the 4*f* states is crucial to gain insight into the Fermi surface topology and low energy excitations, as is borne out of our own density functional theory calculations and will be discussed in greater detail in the next chapter.

7.2 ARPES Results

7.2.1 General Electronic Structure

Angle-resolved photoemission measurements were obtained using a monochromatized VUV5000 helium discharge lamp using a photon energy of 21.2 eV and 40.8 eV, characteristic emission lines of He Iα and He IIα respectively, and a R4000 Scienta electron analyzer with a chamber base pressure better than 5×10^{-11} Torr. After completion of growth, thin films were transferred into the analyzer chamber within 20 minutes without breaking vacuum, thus preserving a pristine surface for photoemission.

In Figures 7.5, we show four-fold symmetrized Fermi Surface maps of $LuAl_3$ and $YbAl_3$ respectively, taken using He Iα photon energy (21.2 eV) at 21 K. Fermi surface for $LuAl_3$ consists of an electron pocket centered at (0,0) and another electron pocket centered at (π,π). Corresponding 2D Fermi surface in $YbAl_3$ at 21 K, shown in Fig. 7.5, reveals a very tiny residual spectral weight at (0,0) from an electron pocket whose band bottom is very close, but above E_F and a 4*f* derived hole pocket centered at (π,π). LDA calculation for $YbAl_3$, as discussed in the previous chapter, predicts the presence of an electron pocket centered at Γ, but completely fails to reproduce the hole pocket that is derived from the

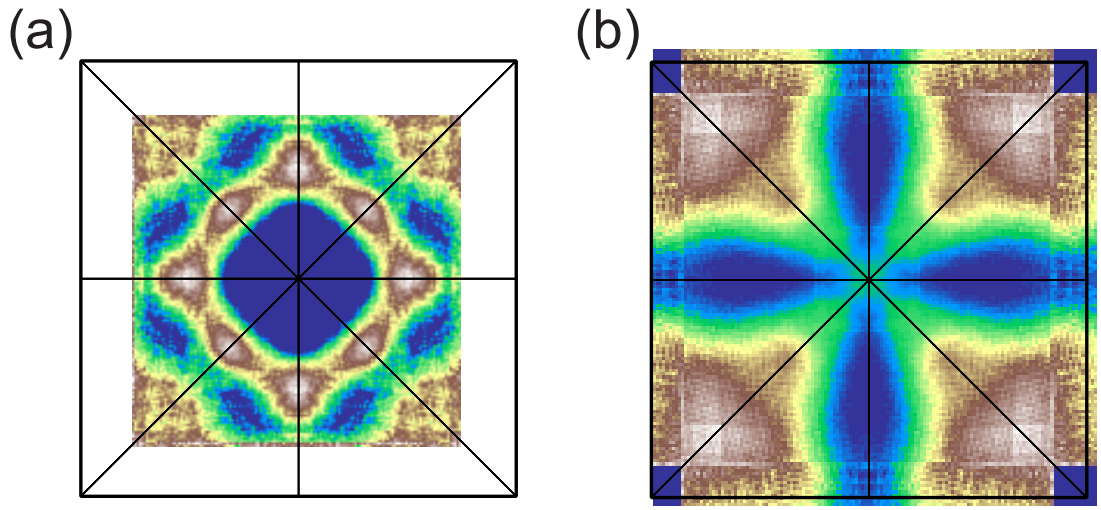

Figure 7.5: Fermi surface maps of a)$LuAl_3$ and b)$YbAl_3$ taken using HeIα photons.

renormalized 4*f* states described in greater detail in the next chapter.

Intensity spectral maps taken along (0,0 - π,0) for $LuAl_3$ and $YbAl_3$ are shown in Fig. 7.6. For $LuAl_3$, contribution only from Lu $4f^{13}$ final states is observed in Fig. 7.6, where the spin-orbit split core levels with J = 7/2 and J = 5/2 are at binding energies 6.72 eV and 8.18 eV, respectively. In contrast, in $YbAl_3$, contributions from both f^{13} and f^{12} final states can be identified indicating that $YbAl_3$ is a mixed valence compound. Spectral peaks very close to the Fermi level with a binding energy of 0.03 eV and 1.34 eV, respectively, constitute features derived from f^{13} final states, the former being derived from $J = 7/2$ final state also known as the Kondo resonance peak, and the latter the spin-orbit split peak derived from $J = 5/2$ final state. Peaks marked with asterisks at binding energies 0.6 eV and 1.9 eV are corresponding surface core levels. The difference in binding energy between the bulk and surface doublets in our measurements is found to be $\approx$ 0.6 eV, consistent with earlier photoemission (PES) measurements on $YbAl_3$

single crystals.[162] Spectral features observed at binding energies between 5 and 11 eV are derived from the $Yb^{3+}f^{12}$ final states.

7.2.2 Correspondence in electronic structure between $LuAl_3$ and $YbAl_3$

Lu, Yb and Al in free form has the following electronic structure

Lu = [Xe] $4f^{14}$ $5d^1$ $6s^2$

Yb = [Xe] $4f^{14}$ $6s^2$

Al = [Ne] $3s^2$ $3p^1$

But, in $LuAl_3$ both Lu is in 3^+ valence state contributing three valence electrons ($5d^1$ $6s^2$). In $YbAl_3$ nominal Yb valence is intermediate between 2^+ and 3^+. So chemical potential in $YbAl_3$ is expected to be at a lower energy than in $LuAl_3$. When Yb is in 3^+ valence state, f electrons are localized, having $4f^{13}$ configuration and contributing 3 valence electrons ($6s^2$ $5d^1$). However, hybridization between the $4f$ and $5d$ states results in a $4f^{14}$ configuration leading to Yb^{2+} valence state. This is because $5d$ electrons are relatively delocalized and do not feel atomic correlations as much as $4f$ electrons. In $YbAl_3$ ground state can be thought to comprise of both $Yb^{2+}(6s^2)$ and $Yb^{3+}(5d^16s^2)$ valence states leading to non-integral Yb valence. At at low temperatures the Yb nuclear charge can be screened by Kondo coupling leading to an increase in the Yb^{2+} f^{14} contribution and creating, as a result, an additional hole at the Fermi surface. Enhanced Kondo screening in $YbAl_3$ at low temperatures is expected to result in the de-

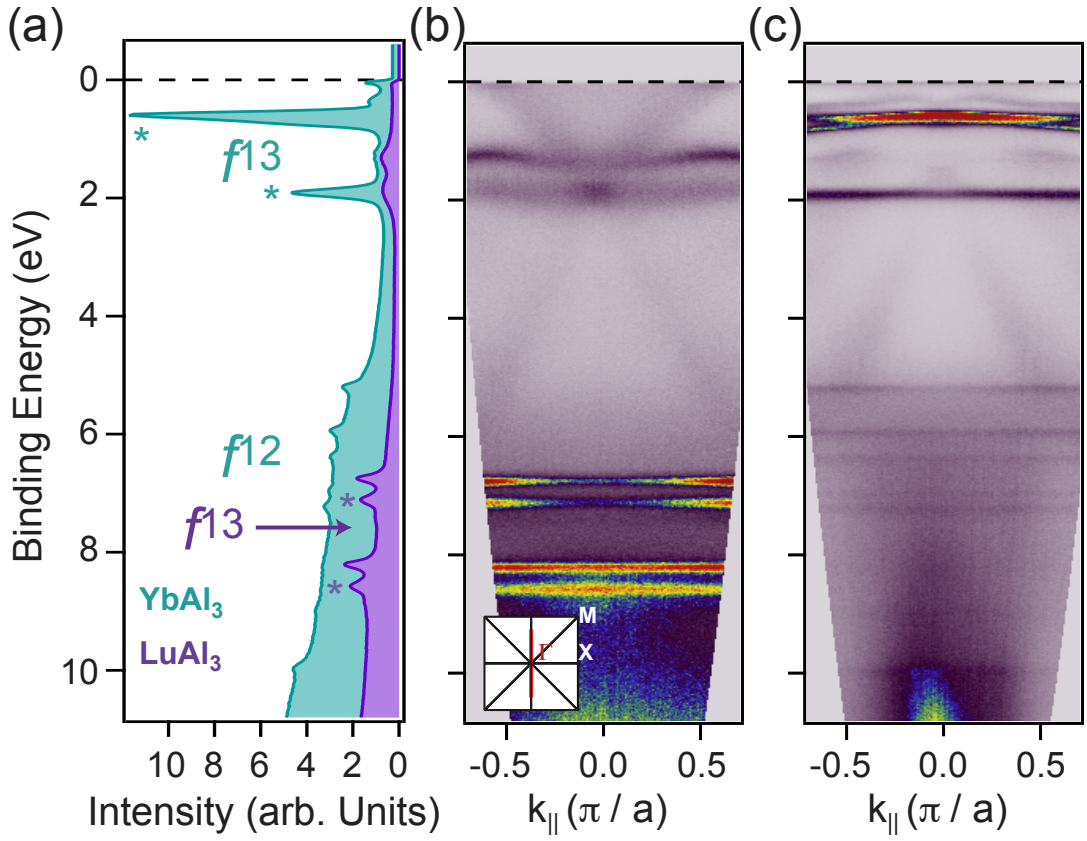

Figure 7.6: E-k spectral map of b)$LuAl_3$ and c)$YbAl_3$. Corresponding EDCs obtained after integrating over the whole momentum region is shown in a).

velopment of Abrikosov-Suhl resonance.[61, 62] As, in Yb, 4*f* orbitals are more than half filled, single impurity Anderson model predicts the resonance to be pinned close but below the Fermi level.[67, 211]

In Fig. 7.7, we compare spectral intensity maps obtained in $LuAl_3$ and $YbAl_3$ for identical ARPES cuts along several different momentum regions. From the spectral map comparison, it is clearly seen that light broadly dispersive and mostly Al derived band-like conduction electron states are similar in $YbAl_3$ and $LuAl_3$ at identical momentum regions within a shift in chemical potential that

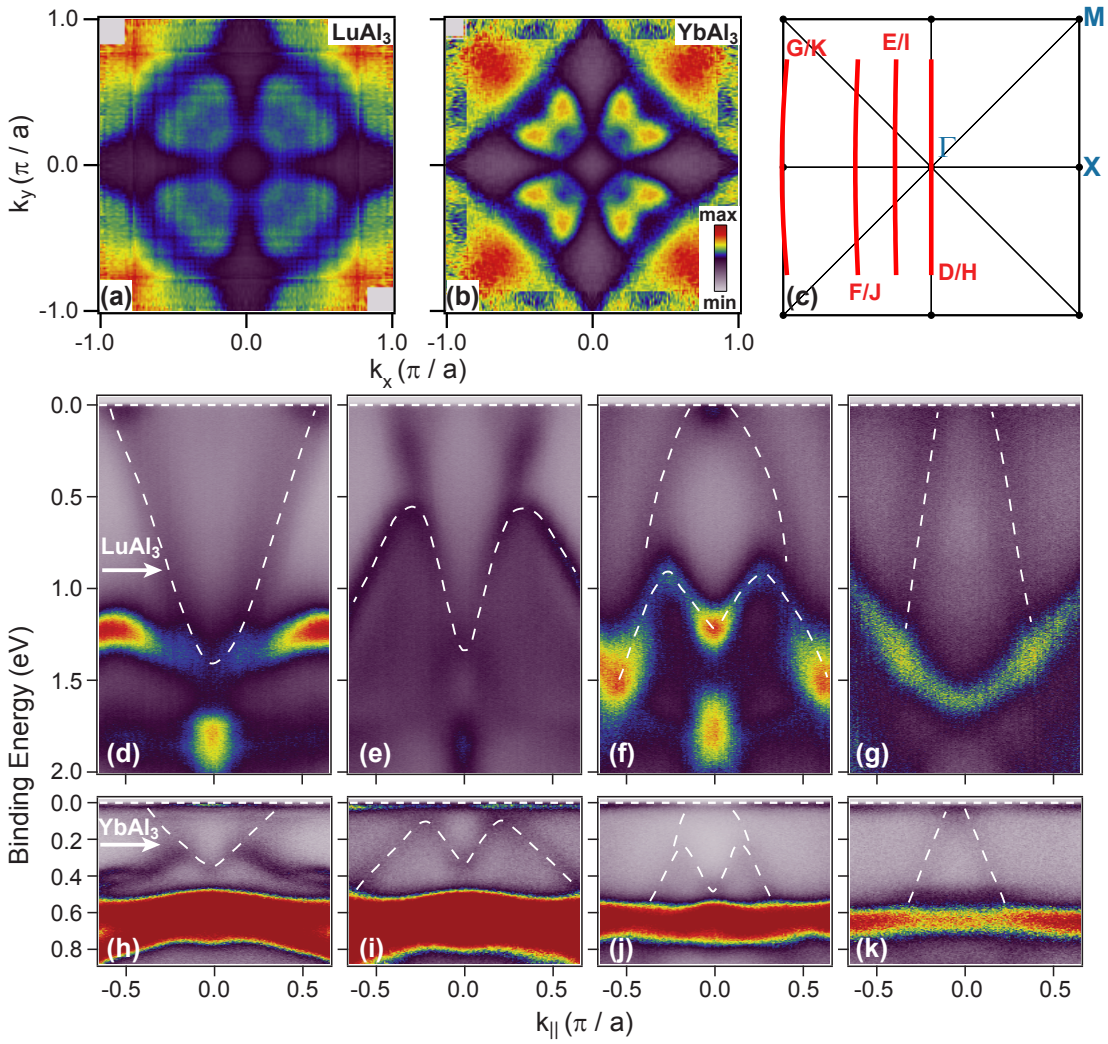

Figure 7.7: Similarity in electronic structure between $YbAl_3$ and $LuAl_3$. Four-fold symmetrized two-dimensional electronic structure of (a) $LuAl_3$ at 0.95 eV binding energy and of (b) $YbAl_3$ at 0.22 eV binding energy, both obtained with photon energy 21.2 eV (He I α). (c) Surface Brillouin zone of $YbAl_3$ and $LuAl_3$ showing high symmetry points and location of the ARPES cuts in the momentum space. Spectral intensity maps corresponding to the ARPES cuts in (c) are shown in (d - g) for $LuAl_3$ and in (h - k) for $YbAl_3$. White dotted lines are guides to eye highlighting similar dispersion in $LuAl_3$ and $YbAl_3$. White arrows in panels (**D**) and (**H**) indicate the binding energies at which two-dimensional maps shown in (a) and (b) are taken, respectively.

accounts for the difference in the Yb and Lu average valence in $YbAl_3$ and $LuAl_3$, respectively. We will focus on the interaction between the broad, dispersive states and the renormalized f states (Abrikosov-Suhl resonance)[61, 62] resulting from Kondo interaction, near the Fermi level in the next chapter. Nevertheless, experimentally observed one-to-one comparison between the momentum-resolved electronic structure in $YbAl_3$ and $LuAl_3$ establishes that we are probing identical momentum region in k_z, both in $YbAl_3$ and $LuAl_3$ for the same photon energy. Because of similarity in the crystal structure of $LuAl_3$ and $YbAl_3$, it is reasonable to expect similar inner potentials for the identical (001) surfaces studied here, which is what we find experimentally.

7.2.3 Determination of k_z

Our ARPES measurements access a two dimensional projection of the three dimensional Brillouin zone centered around a particular k_z value that depends on the incident photon energy, as discussed in Chapter 1. Both $YbAl_3$ and $LuAl_3$ has a three dimensional cubic structure and thus expected to have significant dispersion in their electronic band structure along k_z, as also predicted from ab-initio calculations. Thus, it is important to determine the momentum region we are probing with our particular photon energy of 21.2 eV. One way to determine k_z is by comparing experimentally measured electronic band dispersions with the predictions form DFT+U calculations. However, such an approach poses a challenge for $YbAl_3$, as it is well known that DFT+U methods perform poorly for Kondo lattice systems because they fail to satisfactorily account for the strong correlations of the partially filled f shell.[209] But, such a method should perform reasonably well for $LuAl_3$, which is a conventional metal with completely

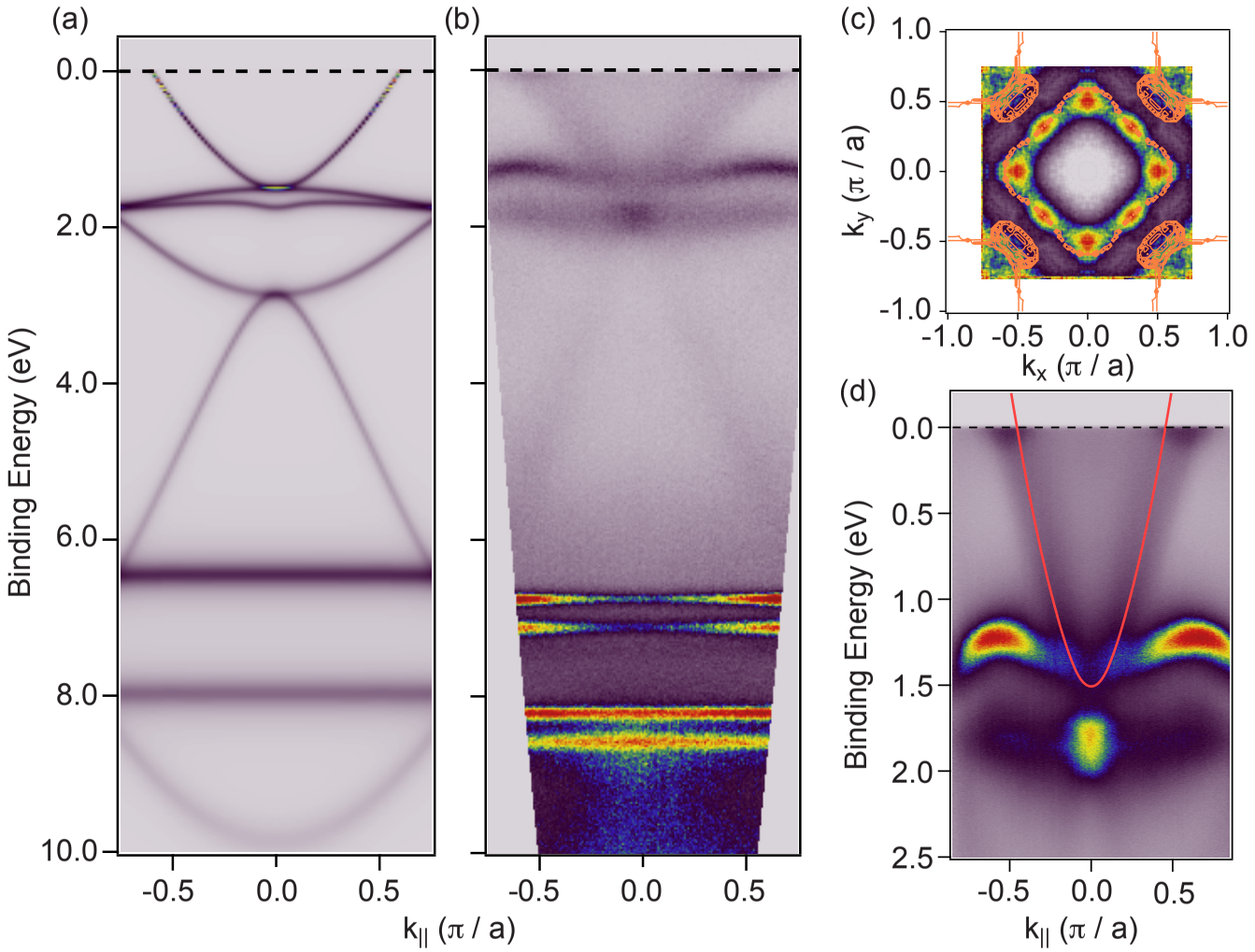

Figure 7.8: Correspondence between calculated and measured bandstructure. a)Simulated electronic spectrum along (0,0 - π,0) at Γ b)Measured electronic structure along identical momentum region using HeIα photons. c) Measured Fermi surface using HeIα photons and calculated two dimensional projection of the Fermi surface on the k_x - k_y plane centered at Γ exhbiting remerakable correspondence between the two. d) Experimentally observed electron pocket at Γ can also be well reproduced in our DFT calculations.

filled *f* shell. Hence, we compare calculated band structure with our experimentally observed data for $LuAl_3$ to help figure our the momentum region along the z direction that we are probing. In the previous section, we have already established that we are measuring identical momentum region in k_z for same photon energies in $YbAl_3$ and $LuAl_3$. Therefore, knowing the probed momentum region for $LuAl_3$ allows us to gain information for $YbAl_3$ as well. Fermi surface of $LuAl_3$ predicted from LDA calculations comprise of a multiply connected hole pocket centered at Γ and an electron pocket centered at the R point. A two dimensional cut at Γ would access only the hole band, the 2D projection of which would consist of features centered at (0,0) and (π,π), consistent with our ARPES measurements. In Fig. 7.8 (c), we show experimentally obtained Fermi surface and the simulated two-dimensional contour plot of the Fermi surface in the k_x - k_y plane centered at Γ overlaid on top, establishing a very good agreement between simulation and experiment. We also compare spectral maps obtained from simulation and experiment along (0,0 - π,0) of the surface Brillouin zone and find very good agreement over a wide energy range.(7.8) In particular, our simulation accurately reproduces dispersion of the electron pocket centered at (0,0). Therefore, comparing measured band structure with ab-initio calculations for $LuAl_3$ and the observed correspondence between the electronic structure for similar ARPES cuts between $LuAl_3$ and $YbAl_3$, we determine that for an incident energy of 21.2 eV, we are accessing a two dimensional momentum region centered around Γ in both $YbAl_3$ and $LuAl_3$.

7.2.4 Influence of crystal field in $YbAl_3$

The intriguing dichotomy of the nature of f electrons is at the heart of many exotic properties in Kondo lattice systems. From early studies involving magnetism in f electron systems, it was realized that strong on-site Coulomb repulsion plays a significant role in the f electrons, leading to a localized character. Such localized states then naturally interact with their environment via crystal field forces, where crystal electric field can lift the degeneracy of a particular spin-orbit split manifold. For example, in a cubic environment, assuming crystal field is weak compared to spin-orbit coupling strength, which is the case for $4f$ systems such as $YbAl_3$, magnetically relevant $J = 7/2$ manifold (relevant for $YbAl_3$) is expected to break up into three crystal field split states - two doublets Γ_6 and Γ_7 and a quartet Γ_8.[212]

However, this idea was strongly challenged in Kondo Lattice systems. It was realized that in order to explain the dramatic $\alpha - \gamma$ iso-structural phase transition of Ce involving a volume change of 14% under a pressure of 7 Kbar, an itinerant model to describe the f electrons in the α phase needs to be invoked. Subsequently, in many lanthanide and actinide based inter-metallic systems, experimental evidence of f electrons forming coherent Bloch waves were found. Today, this is primarily understood in terms of the Kondo screening of the f moments that results in the formation of itinerant heavy bands in a lattice. Subsequently such materials came to be generically known as Kondo lattice systems. However, the degree of delocalization of these strongly correlated f electrons primarily depends on the Kondo coupling strength along with other competing interactions and can be highly material dependent. Even in materials family containing the same rare earth element, the degree of delocalization can vary.

For example in uranium compounds, 5f electrons become increasingly localized going across α-U, US, URu_2Si_2, USe and UTe, where the 5f electrons primarily have an itinerant character in α-U, but are almost completely localized in UTe.[105] A rigorous understanding of the dual nature of f electrons in these systems remains a central challenge in condensed matter systems.[213, 214, 79]

One might then wonder how the crystal electric fields affect the level splittings in these compounds as f electrons become increasingly itinerant. Theoretically, within a self-consistent slave-boson mean field type calculations, it has been predicted that crystal fields can indeed vary as a function of the exchange interaction between the rare earth ion and the conduction electrons, where when fully itinerant, crystal field effects on f electrons should be negligible.[215] Experimentally, information about CEF split levels of the f states has mostly been obtained from neutron scattering experiments where sharp crystal field transitions should be observed in the dynamic magnetic susceptibility.[216, 217] However, this assumes a completely localized picture for the f electrons, where crystal field split states lack well-defined structure in momentum space.

Situation in the Kondo lattice systems, as has been described above, is very different. In such systems localized f states can combine with delocalized conduction electrons forming dispersive hybridized heavy bands that can result in significant deviation from their atomic properties. Such a process can then result in CEF split states acquiring dispersion, where the energy levels can vary as a function of momentum. Understanding the nature of such states is extremely important to gain a microscopic understanding of the magnetic as well as emergent properties of these systems. To identify such effects one needs a k - resolved probe, as methods like inelastic neutron scattering or resonant x-ray

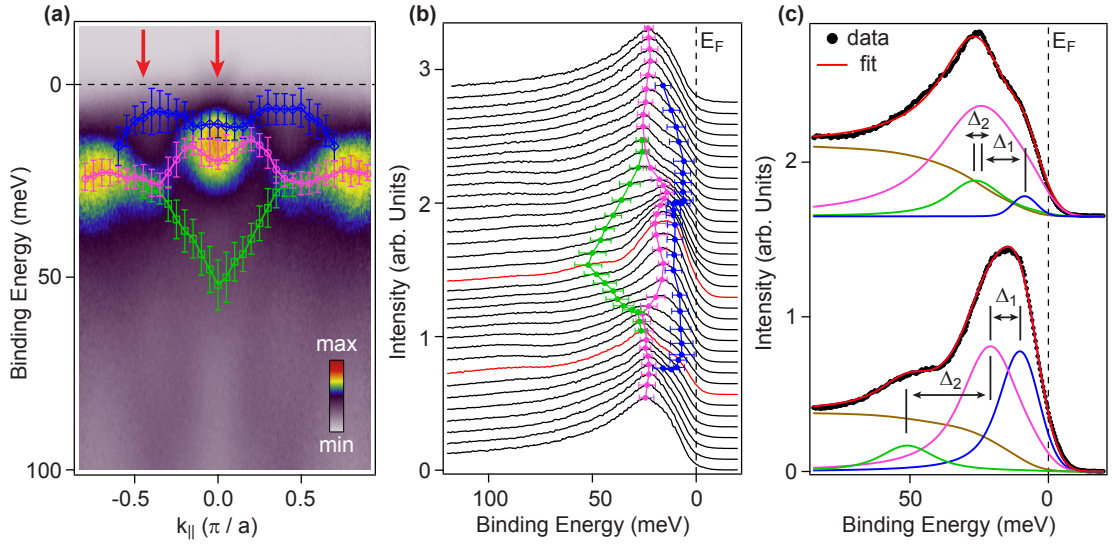

Figure 7.9: Crystalline Electric Field (CEF) split states in $YbAl_3$ (a) High resolution spectral intensity map along (0,0 - π,0) in $YbAl_3$ taken at 21 K showing dispersive CEF split states. (b) Waterfall EDC plot with the extracted dispersion of the CEF split states overlaid on top. (c) EDCs taken at the momentum region shown by red arrows in (a), also highlighted in red in (b) with their corresponding fits showing individual contributions. Two different EDCS cuts are displaced vertically for clarity. A Shirley background [27] that has been subtracted prior to the fitting process accounting for the inelastically scattered electrons is shown in brown. Binding energy separation between the CEF split states (Δ_1, Δ_2) at the two different k points are also indicated.

scattering integrate excitations over the whole *k* - space. Momentum resolving capabilities of ARPES can uniquely address this problem. Indeed, recent ARPES studies has revealed dispersive CEF states in a few Kondo lattice systems, such as $YbRh_2Si_2$[218], $CeRh_2Si_2$[219], whose energy levels can get altered at certain momentum regions.

In $YbAl_3$, as has been described in Section 7.3, an analysis of the transport coefficient indicates full N=8 fold degeneracy of J=7/2 manifold.[175] This is consistent with the lack of any sharp CEF excitations in neutron scattering experi-

ments on this material.[220, 221, 222] This has generally been ascribed to high Kondo temperature ($T_K \approx 670$ K) in this compound. In Fig.7.9 using high resolution ARPES measurements, we show that the degeneracy of the CEF states can be lifted at certain k-points as they become dispersive hybridizing with the conduction electrons at the band crossings. In a cubic environment, Yb J=7/2 manifold is expected to break up into three crystal field levels Γ_6, Γ_7 and Γ_8 and we observed three individual bands in Fig. 7.9. Extracted dispersions from our ARPES data, shown in Fig. 7.9 can be well understood as arising out of the hybridization of a light band and three crystal field levels of the J=7/2 manifold, degeneracy of which is lifted as they hybridize with the light bands. The bandwidth of each of these crystal field split states is roughly comparable to their separation ($\approx$ 10 meV), which would suggest that when integrating all allowed transitions over k, no sharp structure in energy should be observed, explaining the absence of well-defined excitations in inelastic neutron scattering data. Energy distribution curves, shown in Fig.7.9 (c) taken at two different momentum regions indicated in Fig.7.9 (a) establish momentum dependent energy separation between the CEF split states. This again underscores the importance of momentum dispersive measurements in understanding the properties of Kondo lattice systems.

CHAPTER 8

TEMPERATURE DEPENDENT EVOLUTION OF THE ELECTRONIC STRUCTURE IN $YbAl_3$: CONNECTING *r*-SPACE WITH *k*-SPACE

In this chapter, we describe how enhancement of the Kondo coupling at lower temperatures brings about a change in the electronic structure of $YbAl_3$. In $YbAl_3$, the local electronic structure changes with temperature that is believed to be due to enhanced Kondo screening of the $4f$ moments at the Yb sites, resulting in a decrease in the average Yb valence. But, how such a local change is manifested in changes in low energy excitations and Fermi surface topology that are crucial to understand its physical properties and Fermi surface instabilities, has remained enigmatic. In this chapter, combining high and low energy spectroscopy, we provide a microscopic picture elucidating an intimate connection between the temperature dependent changes in real and momentum space electronic structure in $YbAl_3$, which should be generic to any mixed valence system.

8.1 Evolution of Yb valence in $YbAl_3$ thin films

In this section, we describe temperature dependent changes in the average Yb valence in our $YbAl_3$ thin films that represents changes in the local electronic environment at the Yb sites, estimated using x-ray photoemission spectroscopy (XPS) and resonant x-ray emission spectroscopy(RXES). We compare our results with existing estimates reported in the literature from measurements on $YbAl_3$ single crystals.

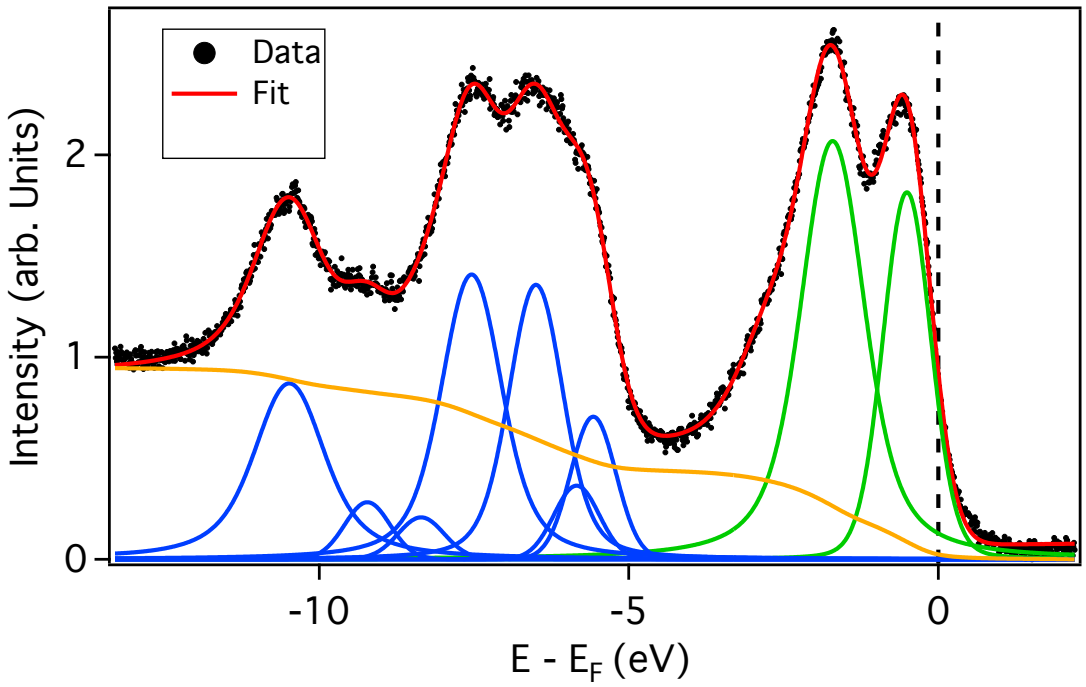

Figure 8.1: Fit to XPS spectrum obtained using Al Kα photons at 110 K from a 25 nm thick $YbAl_3$ film. Shirley type background accounting for inelastically scattered electrons is shown in orange. Lorentzians shown in green and blue account for Yb^{2+} and Yb^{3+} contributions to the measured XPS spectrum, respectively.

8.1.1 Evolution of XPS spectra

X-ray photoemission spectroscopy (XPS) is a close cousin of ultra-violet photoemission (UV-PES), only difference being that in XPS, x-rays are used instead of ultra-violet photons. In XPS more energetic photons are employed, leading to less surface sensitivity compared to UV-PES.(Fig.2.2) Here, we have used XPS to determine the average Yb valence and its evolution as a function of temperature. To generate x-rays, we used a commercial dual-anode x-ray source using Al k_α photons with characteristic energy 1486.6 eV. Emitted photoelectrons

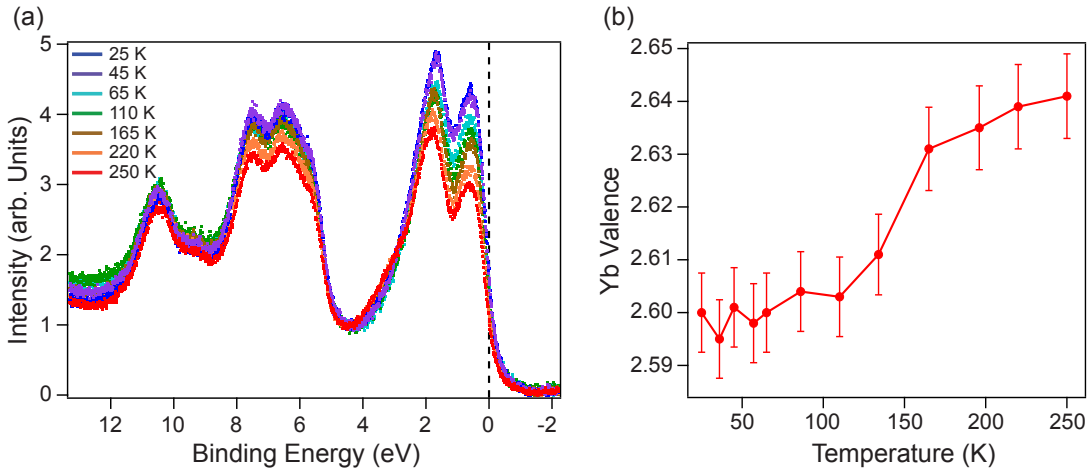

Figure 8.2: a)Evolution of XPS spectra with temperature b)Yb valence as a function of temperature evaluates estimating spectral intensity corresponding to f^{13} and f^{12} final states.

were detected using Scienta R4000 analyzer in the high pass mode, suitable for detection of high kinetic energy electrons. In mixed valence systems, such as $YbAl_3$ photoemission spectra should consist of two different final state multiplets corresponding to different initial valence configurations. For $YbAl_3$, both $4f^{13}$ (spectral peaks between 0 - 2 eV) and $4f^{12}$ (spectral peaks between 5 - 12 eV) final states that correspond to Yb^{2+} $4f^{14}$ and Yb^{3+} $4f^{13}$ initial states, respectively and are separated by $U_{ff} \approx 6.5eV$. Average Yb valence v can be determined evaluating the integral spectral weight corresponding to $4f^{13}$ (I^{2+}) and $4f^{12}$ (I^{3+}) final states as

$$v = 3 - \frac{I^{2+}/14}{I^{2+}/14 + I^{3+}/13} \tag{8.1}$$

Individual XPS scans measured at a particular temperature is fitted by a waveform consisting of a number of lorentzians, 2 for Yb^{2+} final state and 7 for Yb^{3+} final state (7 lorentzians were found to be adequate to fit our data, as our experimental resolution, ≈ 90 meV, is not able to resolve all the $4f^{13}$ fi-

nal state multiplets), multiplied by an appropriate Fermi-Dirac distribution and convoluted by a Gaussian that accounts for experimental broadening.(Fig. 8.1) A Shirley type background that accounts for contributions from inelastically scattered electrons is subtracted before the fitting procedure is performed. In Fig. 8.2, we show estimated variation in average Yb valence in $YbAl_3$ with temperature. As described in Chapter 1, measured intensity can be strongly influenced by matrix element and final state effects. Furthermore, to have a good estimation of the background intensity, knowledge of the non-4*f* spectral weight at that particular photon energy and contributions from inelastically scattered electrons is required. This makes the estimation process tricky, leading to errors in estimated absolute Yb valence. However, we can determine a relative change in intensity as a function of temperature with much better precision leading to accurate estimation of temperature dependent change in Yb valence, because a change in temperature is expected to negligibly affect the factors modulating measured photoemission intensity and non-4*f* spectral weight.

8.1.2 Evolution of RXES spectra

Introduction to RXES

Resonant x-ray emission spectroscopy (RXES) is a photon-in photon-out technique that can be used as a truly bulk sensitive alternative to XPS for determination of rare-earth valence in Kondo lattice systems. For $YbAl_3$, we use incident photon energy tuned to the Yb L_3 absorption edge, thus resonantly enhancing signal from Yb atoms in $YbAl_3$, making it element specific. As ground states with Yb^{2+} and Yb^{3+} valence states undergo slightly different transitions as

shown in Fig.8.3, absorption edges corresponding to two different Yb valence configuration is seprated in energy by $\approx$ 8 eV.[164] Hence, an analysis of the absorption spectral weight corresponding to different Yb valence leads to an estimate of the average Yb valence in $YbAl_3$. In RXES the emitted x-rays are energy resolved and only a particular decay channel is collected.[223, 161] In contrast, in x-ray absorption spectroscopy (XAS) in the transmission mode, the total absorption by the sample is measured, and in the Total fluorescence yield (TFY) mode, all emitted x-rays from the excited state are collected leading to poor energy resolution. In this particular experiment, we collect only Yb $L_{\alpha 1}$ photons. RXES has a better intrinsic line width of the spectral features resulting in greater resolving power compared to XAS. In $YbAl_3$, L_3 absorption edge creates a 2p core hole exciting an electron from 2p to 5d. The intrinsic spectral broadening for XAS in transmission or in TFY mode is then determined by the lifetime of deep lying 2p core level. But, in RXES, we are only collecting photons emitted in the $L_{\alpha 1}$ decay channel that creates a 3d hole. The spectral broadening is now determined by the 3d level that is much shallower compared to the deeply bound 2p level, hence intrinsic spectral broadening is much smaller. This can be seen in the two-dimensional spectral map of the RXES spectra in Fig.8.4 a), where the spectral broadening along the x- axis(Excitation energy), Γ_p is much larger than along the y-axis(Energy transfer, (E_{in} - E_{out})), Γ_d.

Experimental SetUp

RXES spectra was collected at the Cornell High Energy Synchrotron Source (CHESS) at the C1 bend magnet beamline under ring conditions of 5.3 GeV and 100 mA. Incident x-ray radiation was monochromated using a Rh mirror and

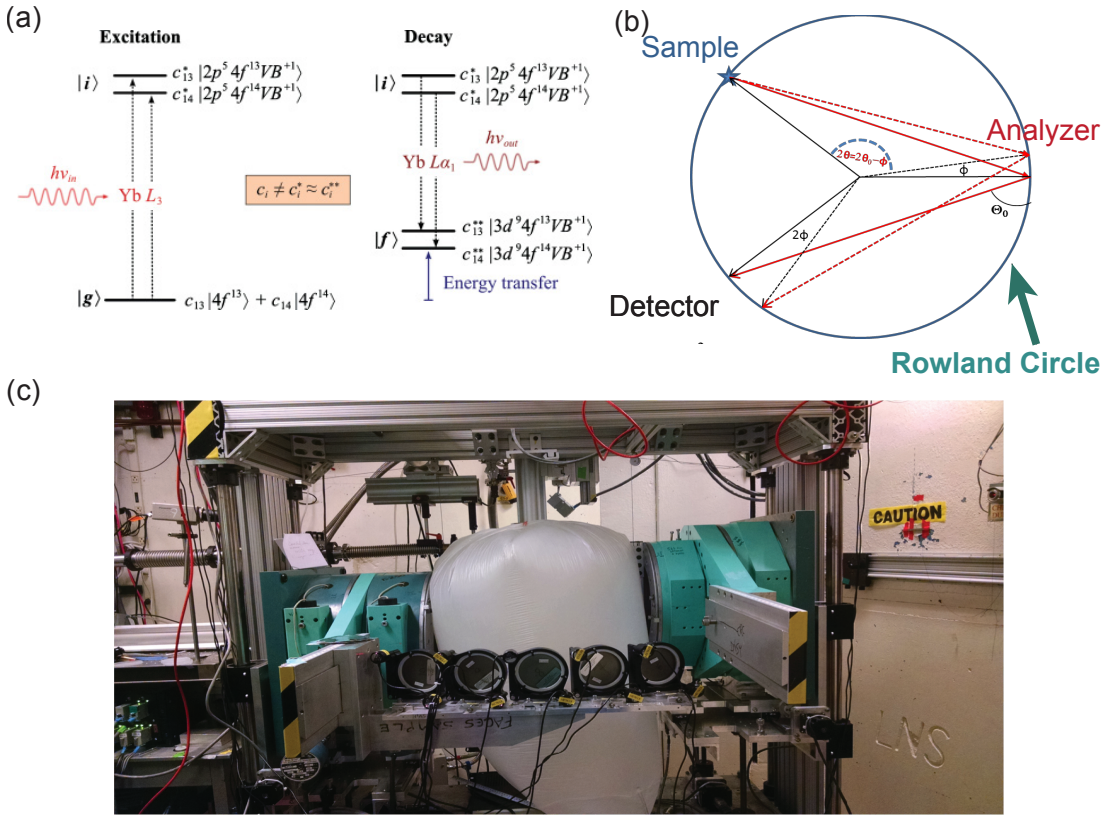

Figure 8.3: RXES process and the experimental setup. a)Energy diagram showing relevant excitations for Yb L_{III} - $L_{\alpha 1}$ RXES process. b) The measurement geometry with the sample, analyzer crystal and detector all on a Rowland circle. c) Experimental setup for RXES at the C2 beamline at CHESS

sagittal focus double Si (220) crystal monochromator. Incident energy was calibrated by using Cu foil where the energy of the first inflection point was set to 8980.3 eV. X-ray emission was monochromated and focused using five spherically bent Si(444) crystals in the Rowland geometry by using the CHESS dual array valence emission spectrometer (DAVES).[224] X-rays were finally collected with a Pilatus 100K area detector (Dectris). Use of area detector offered significant advantages for the current experiment in terms of ease of alignment and reliable background subtraction. Two regions of interest (ROIs) were chosen,

one containing more than 95% of the emission signal and another centered on the first ROI, but twice in size. The larger ROI was used to correct for the average background counts as

$$I_{corrected} = I_{ROI_1} - Area_{ROI_1}(\frac{I_{ROI_2} - I_{ROI_1}}{Area_{ROI_2} - Area_{ROI_1}}) \tag{8.2}$$

Measured counts were further corrected for variations in incident photon flux by normalizing with the measured incident flux using a N_2-filled ionization chamber placed upstream of the sample stage. x-ray emission energy was calibrated measuring the $K_{\alpha 1}$ and $K_{\alpha 2}$ lines of a Cu foil. Overall energy resolution of the setup was determined to be better than $\approx$ 3 eV measuring quasi-elastic scattering from a polyimide sample. No photodamage was observed even after taking more than 4 scans (maximum number of scans taken at a particular spot) at a single spot. Sample was mounted on a closed cycle cryostat with base temperature of 45 K. A helium filled bag covered most of the x-ray path between the sample, analyzer and detector. This was placed to minimize ambient scattering of the x-rays.

Results

In Fig. 8.4 we show normalized spectra taken at $L_{\alpha 1}$ emission line both at 300 K and 45 K. It is clearly seen that the contribution of Yb^{2+} absorption peak increases at the lower temperature indicating that average Yb valence decreases with temperature. To obtain a quantitative estimate of the average Yb valence, the RXES spectra was fitted with Voigt functions for absorption peaks corresponding to Yb^{2+} and Yb^{3+}. Absorption feature corresponding to Yb^{3+} exhibits a double peak structure requiring two component Voigt function. The double-peak structure for Yb^{3+} component has been seen in other Yb-intermetallic com-

pounds such as YbCuAl[225] and $Yb_2Ni_{12}P_7$[226] and is ascribed to the crystal field splitting of the unoccupied Yb 5*d* states.

A series of *arctan-like* function capturing the edge jumps corresponding to the absorption edges are used to estimate the background. RXES spectra along with the corresponding fit showing contributions from individual components is shown in Fig.8.4. Average Yb valence was found to be 2.83 ± 0.01 at 300 K and 2.78 ± 0.01 at 45 K, and were estimated using the following formula

$$\nu = 2 + \frac{I(3^+)}{I(2^+) + I(3^+)} \tag{8.3}$$

where $I(2^+)$ and $I(3^+)$ are respective intensities of Yb^{2^+} and Yb^{3^+} components.[223, 160] Thus, from 300 K to 45 K average Yb valence in $YbAl_3$ decreased by ≈ 0.05, consistent with results from similar measurements on $YbAl_3$ single crystals.[161, 168]

8.1.3 Conclusion

In Table 8.1, we present Yb valence in $YbAl_3$ as estimated using various spectroscopy techniques, including our own results from $YbAl_3$ thin films. Due to uncertainty in background estimation, final state effects, and inability to satisfactorily separate the bulk from surface contributions, absolute value of the estimated Yb valence varies depending on the nature of the probe used.

However, as discussed earlier, all such methods should allow for estimation of change in valence with temperature much more accurately. Accordingly, we have plotted change in Yb valence, $\Delta\nu$ as a function of temperature in Fig. 8.5, calculated both from values reported in the literature and from our own results. We have calculated change in valence at a temperature T by subtracting

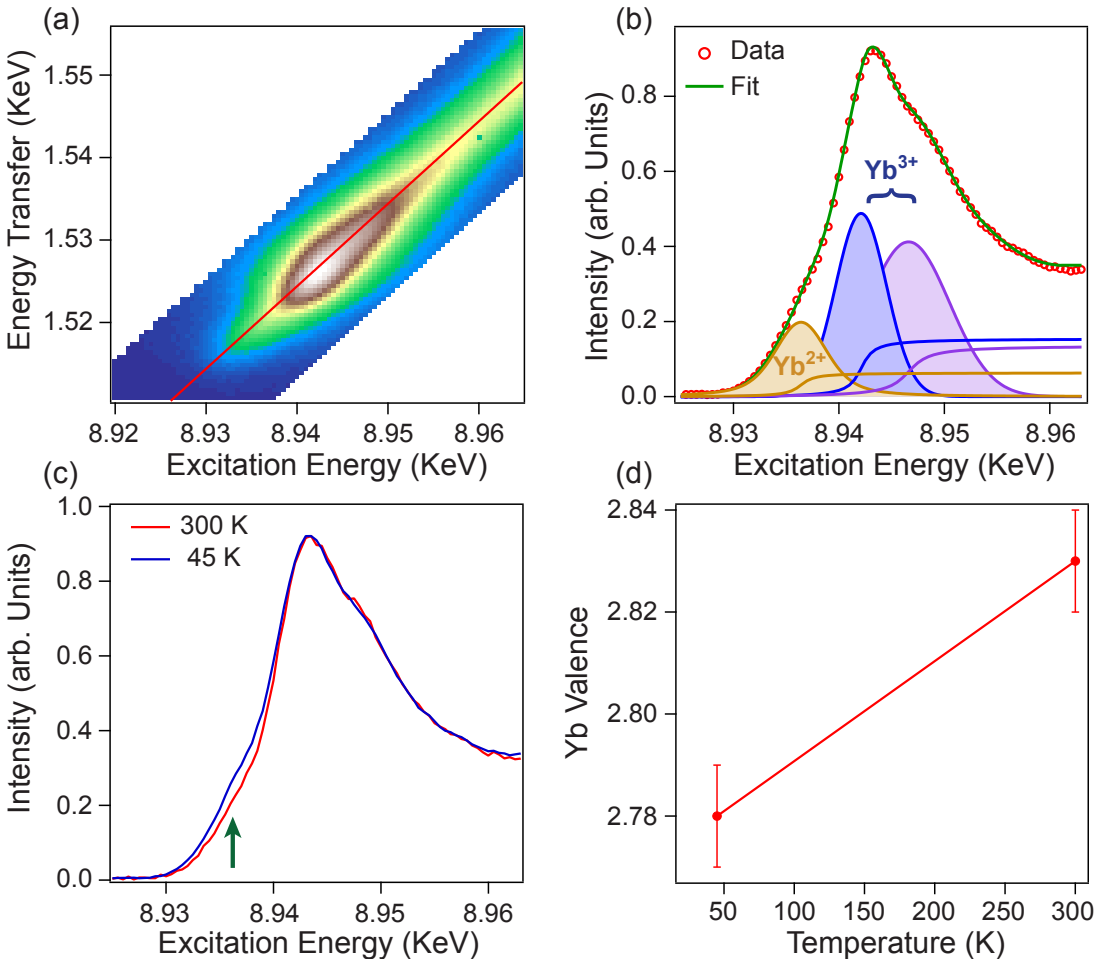

Figure 8.4: a) Two-dimensional intensity map of the photon yield around Yb $L_{\alpha 1}$ emission energy plotted as a function of incident energy and energy transfer into the sample (E_{in} - E_{out}). Line cut shown in red b) Corresponding RXES spectra of $YbAl_3$ at the Yb $L_{\alpha 1}$ emission energy with the corresponding fit showing contributions from Yb^{2+} and Yb^{3+} and arc-tan like contributions capturing the edge jumps. Absorption feature corresponding to Yb^{3+} has a double peak structure which is ascribed to the crystal field splitting of Yb 5d band. corresponds to $L_{\alpha 1}$ emission energy. c) Identical cut as in b) at two different temperatures. Spectra are scaled to highlight enhanced contribution from Yb^{2+} at the lower temperature. d) Estimated Yb valence as a function of temperature as obtained from RXES

Table 8.1: Estimated Yb valence employing various spectroscopies

Technique	$YbAl_3$ valence
PES (hν < 120 eV)	2.77 (10 K)[166]2.77 (21 K)[227]2.63 (20 K)[228]
PES (hν > 500 eV)	2.60(21 K)[227]2.65 (20 K) [162]
4*f* HAXPES	2.71 (180 K)[162]2.47 (20 K)[161]
XAS/RXES	2.78 (300 K)[160, 161]2.78 (45 K)[227]2.75 (10 K)[168]

measured valence at the lowest temperature in the data set, from the measured valence at T. For each of the reported data sets, lowest temperature at which Yb valence was measured is equal to or lower than 45 K, below which change in Yb valence with temperature is negligible within the experimental error. Hence, our procedure of calculating the change in valence $\Delta\nu$ does not add any additional errors. From Fig. 8.5, we can immediately conclude that most of the spectroscopic results agree that the change in Yb valence is ≈ 0.05 between 300 K and temperatures below ≈ 45 K. Only outliers are the results from hard x-ray photoemission (HAXPES) that uses Yb 4*f* core-levels to determine Yb valence from fractured single crystals. Such discrepancy probably originates primarily from large perturbed regions of the surface[171] resulting from scraping or trying to cleave a not so easily cleavable sample, as has been pointed out by the authors of the ref.[161] themselves. An analysis of HAXPES data from deeply bound Yb 3d core levels, which are expected to be less influenced by surface disorders, yields values for Yb valence in agreement with the XAS/RXES results. This further bolsters the above assertion that the discrepancy in Yb valence obtained from HAXPES measurements of the Yb 4*f* core-levels is due to significant

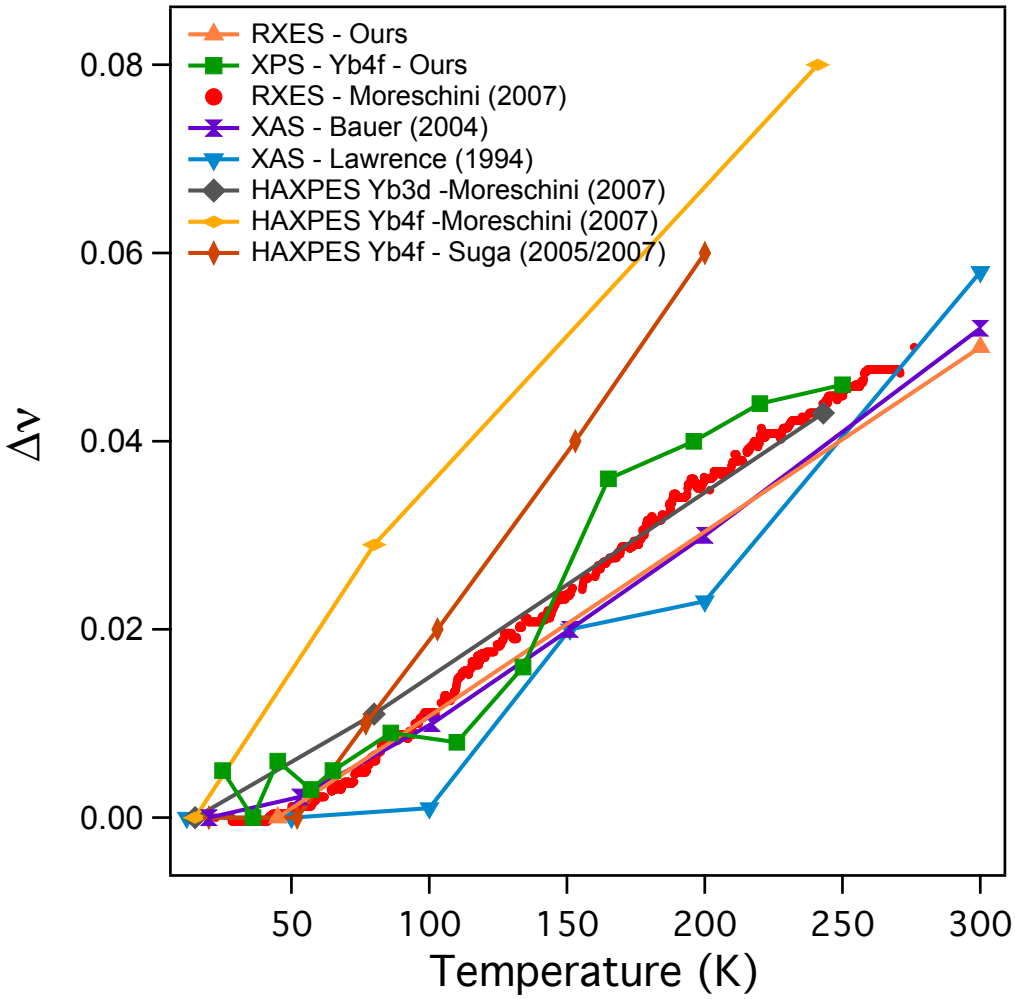

Figure 8.5: Change in Yb valence in $YbAl_3$ as obtained using various spectroscopic probes. Moreschini(2007) [161], Bauer(2004) [168], Lawrence(1994) [160], Suga(2005) [162], Suga(2007) [163]

surface disorder in scraped single crystals.

8.2 Evolution of low energy electronic structure in $YbAl_3$ thin films

8.2.1 Evolution of the light bands

Having estimated the temperature dependent change in Yb valence, we now turn towards the evolution of its k - resolved electronic structure. In Fig. 8.6, we show a series of high resolution spectral intensity maps obtained along (0,0 - π,0) at $k_z \approx 0$ between 255 K and 21 K, as temperature was lowered.

Our measurements reveal a dramatic temperature dependent shift of the chemical potential $\delta\mu$, resulting in the renormalized $4f$ derived states moving closer to the Fermi level at lower temperatures, consistent with earlier angle-integrated result of scraped $YbAl_3$ single crystals. However, the most dramatic effect of such a chemical potential shift is on the parabolic electronic pocket centered at Γ. At 255 K, the electron pocket can be clearly observed with the band bottom at 50 ± 5 meV binding energy and at a k_F of 0.20 ± 0.03 π/a. As the temperature is lowered, the electron pocket is shifted in energy towards lower binding energies and eventually undergoes a Lifshitz transition and becomes entirely unoccupied. This is clearly seen in Fig.8.7 a), where we show a stacked plot of momentum distribution curves (MDCs) at the Fermi level(E_F) at different temperatures. For all temperatures till 31 K, two spectral peaks can be distinguished, as expected for Fermi crossings of a parabolic electron-like band centered at (0,0). However, at 21 K within our experimental resolution, only a single spectral peak can be identified because now the electron pocket has become completely unoccupied and only the residual spectral weight is observed

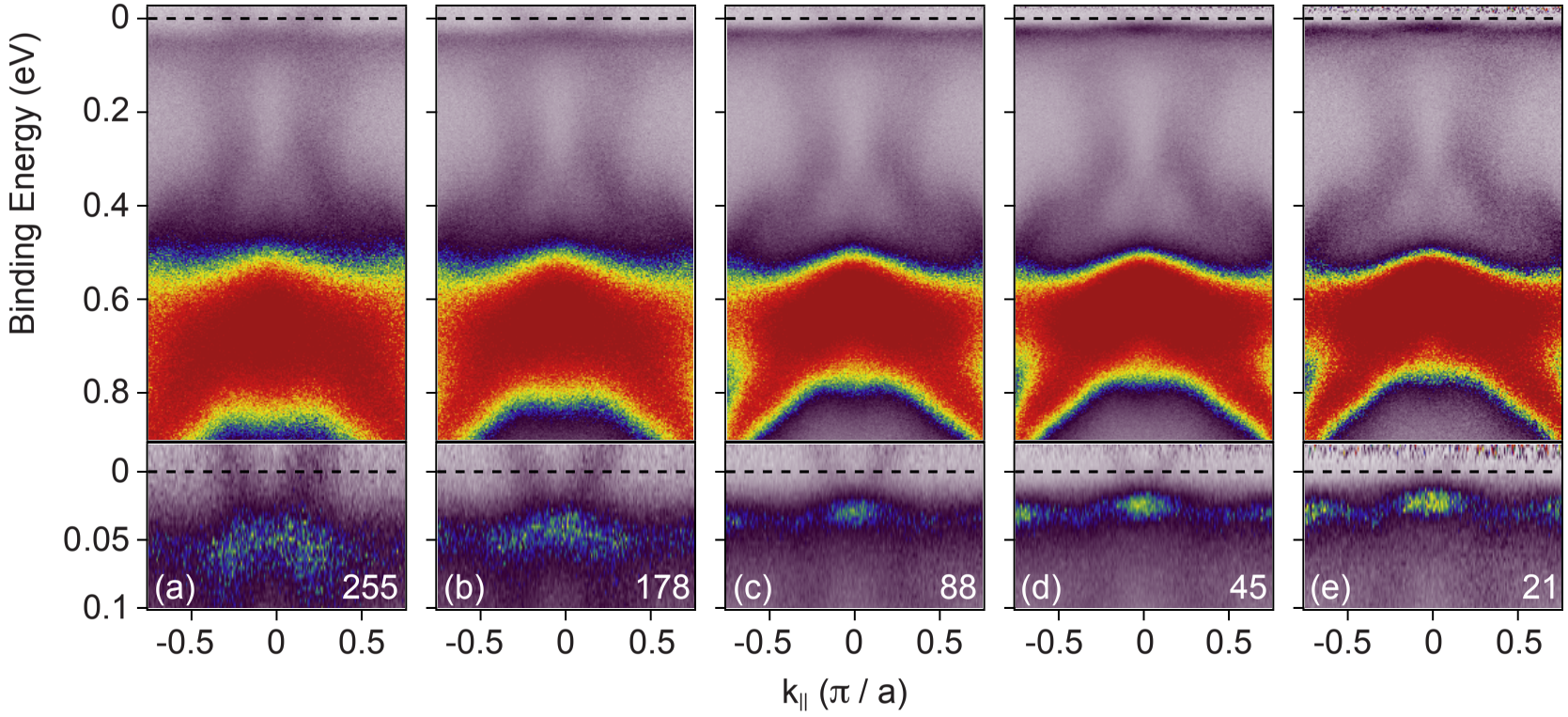

Figure 8.6: Chemical Potential Shift in $YbAl_3$. a - e) Temperature evolution of the ARPES intensity plots in $YbAl_3$ taken along (0,0 - 0,π) direction with He Iα excitation energy. Corresponding zoomed in plots near the Fermi energy are shown at the bottom. Spectral maps are divided by the corresponding Fermi-Dirac distribution to account for temperature dependent thermal broadening to emphasize intrinsic temperature dependence of the spectral features at low binding energies .

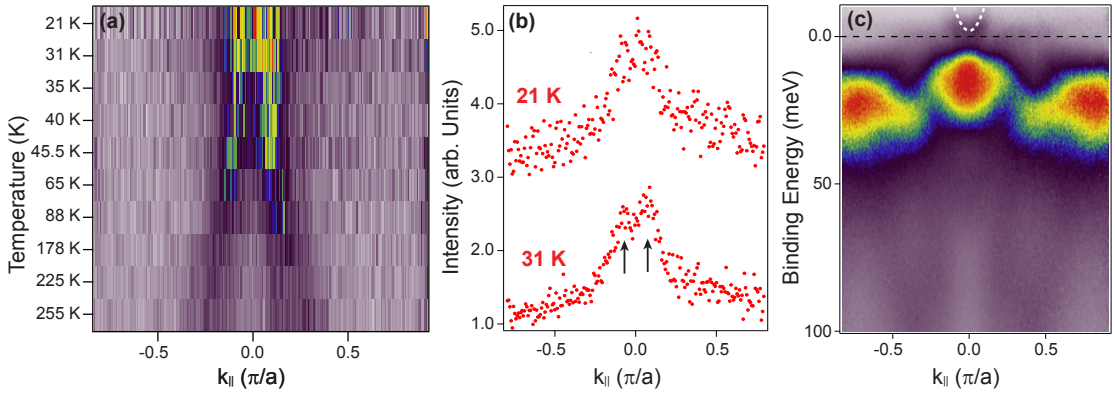

Figure 8.7: Lifshitz transition in $YbAl_3$ a)Stacked plot of MDCs at different temperatures. b) Two spectral peaks can be identified in the MDC plot taken at 31 K while only one spectral peak is observed in teh corresponding MDC plot at 21 K establishing that the electron pocket centered at (0,0) is now completely unoccupied. The central spectral peak at 21 K is due to residual spectral weigh because of finite energy resolution of the experiment. c) High resolution, high-statistic spectral intensity map at 21 K obtained after dividing by the resolution broadened Fermi function. The parabolic band (white dotted line), is a guide to eye for the dispersion of the electron-like pocket at Γ.

at (0,0) (Fig.8.7 b)). This is clearly seen in Fig. 8.7 c), where high resolution high statistic spectral intensity map taken at 21 K is divided by resolution broadened Fermi-Dirac distribution to access thermally populated electrons. The band bottom of the electron pocket centered at (0,0) is now clearly seen above the Fermi energy. We can now understand anomalies in specific heat in the temperature range 15 - 40 K (Fig. 6.1), as arising out of the Lifshitz transition. Within our experimental resolution, we did not observe any noticeable change in dispersion of the electron pocket with temperature. Thus, the most pronounced effect of lowering the sample temperature is that of a chemical potential shift. However, unlike Yb f^{13} final states, Yb f^{12} final state did not appear to shift in binding energy with temperature, consistent with earlier high energy photoemission re-

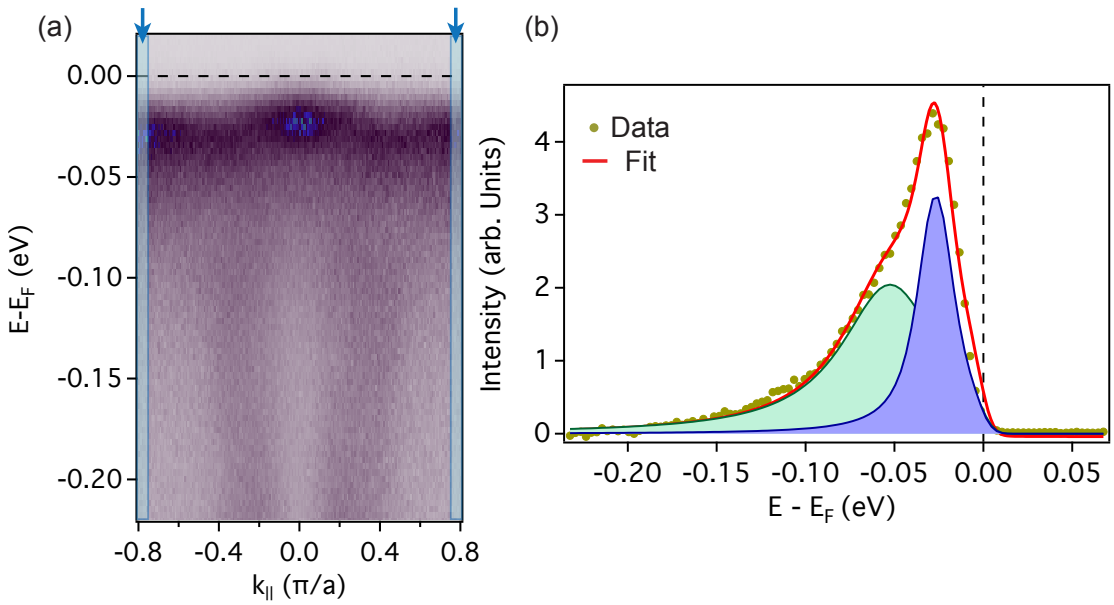

Figure 8.8: a)EDCs are obtained by integrating over the momentum region highlighted in blue. b) A representative EDC with corresponding fit is shown along with individual contributions. A shirley type[27] background has been subtracted.

sults on single crystals.[162] This indicates that the observed shift in chemical potential is brought about by low energy alteration in band filling due to the emergence of a Kondo screened many body state.

8.2.2 Evolution of the heavy bands

We now turn towards the evolution of the 4*f* derived heavy bands. In Fig.8.9 a), we show a few representative energy distribution curves (EDCs) at different temperatures obtained by integrating over a momentum region indicated in Fig. 8.8.

By fitting the EDCs, we obtain a quantitative estimate of the change in 4*f*

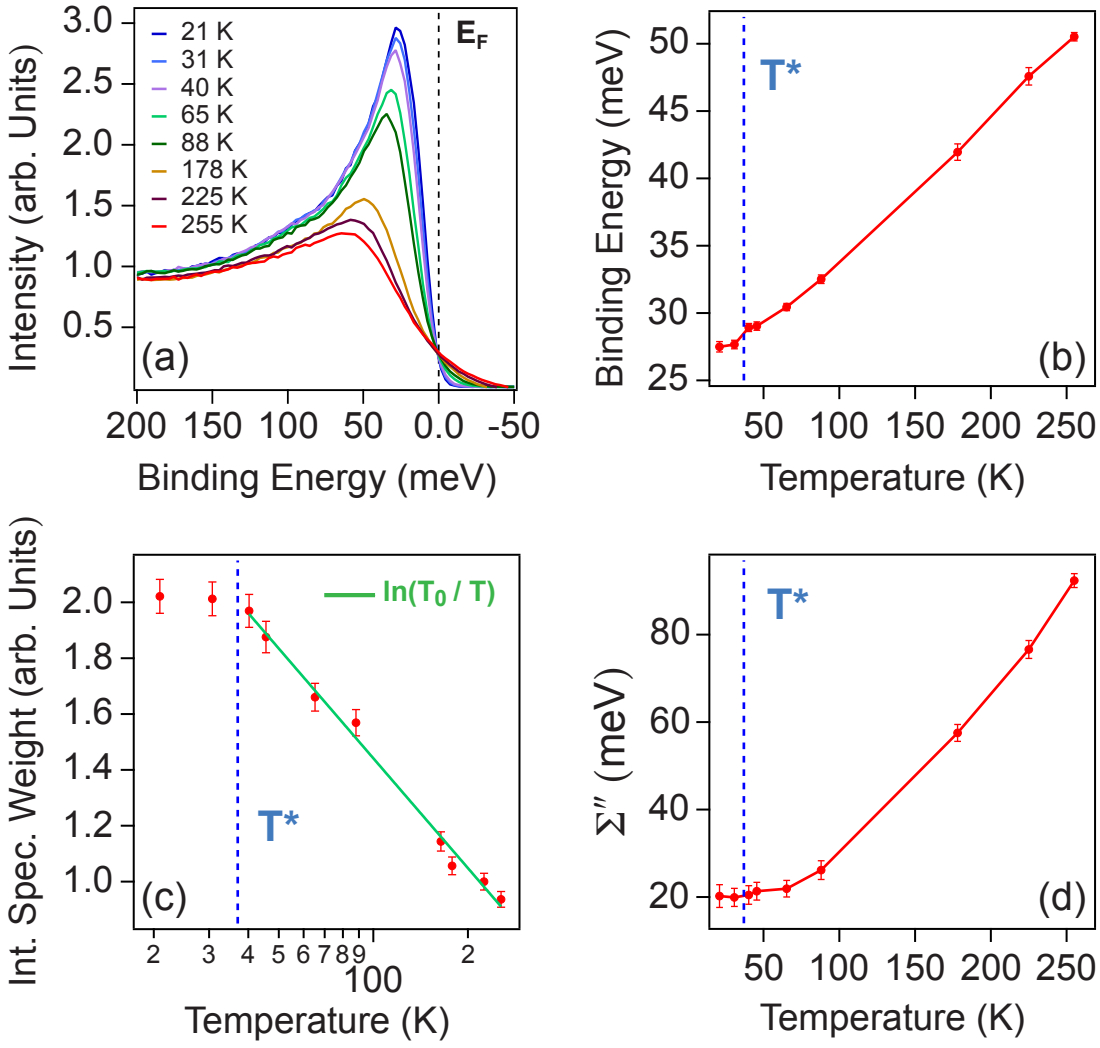

Figure 8.9: a) Evolution of the Kondo resonance peak with temperature. EDCs are obtained by integrating over a momentum region shown in Fig. 8.8 a). Temperature dependence of b) 4*f* binding energy, c) integrated spectral weight, d) scattering rate. A fit to $\ln(\frac{T_0}{T})$ functional form of the data points above T^* is shown in green in c).

binding energy, spectral weight and the scattering rate as a function of temperature, shown in Fig 8.9 b), c) and d) respectively. As temperature is lowered, the heavy 4*f* derived band moves towards a lower binding energy due to the shift in chemical potential as discussed earlier. 4*f* spectral weight increases while the 4*f* scattering rate decreases, both of these quantities together with 4*f* binding energy saturate below $T^* \approx 37$ K, the coherence temperature in our thin films. Saturation of the movement of the heavy band towards a lower binding energy indicates that the screening of the 4*f* moments by the conduction electrons is almost complete at T^*. This also results in a saturation of the 4*f* spectral weight. Till the onset of the Fermi liquid behavior at T^*, integrated spectral weight shows a $\ln(\frac{T_0}{T})$ scaling behavior as expected from a two fluid model.[77] Similar to the DFT+DMFT prediction for $CeIrIn_5$[229], 4*f* spectral weight in $YbAl_3$ does not show any clear onset temperature till 255 K, the highest temperature at which our data is taken. Hence, we do not attempt to estimate T_0, but the observed scaling behavior establishes that the logarithmic increase in the density of states of heavy electron Kondo liquid is saturated as low temperature Landau Fermi liquid behavior emerges. Finally, transport and thermodynamic measurements have already indicated that T^* in $YbAl_3$ could be related to coherence in the 4*f* states as it has been found to be very sensitive to dilution of the Yb sublattice.[32, 168] Saturation of the 4*f* quasiparticle lifetime in our photoemission data provides a direct spectroscopic evidence of the emergence of coherence in the 4*f* derived states at T^*.

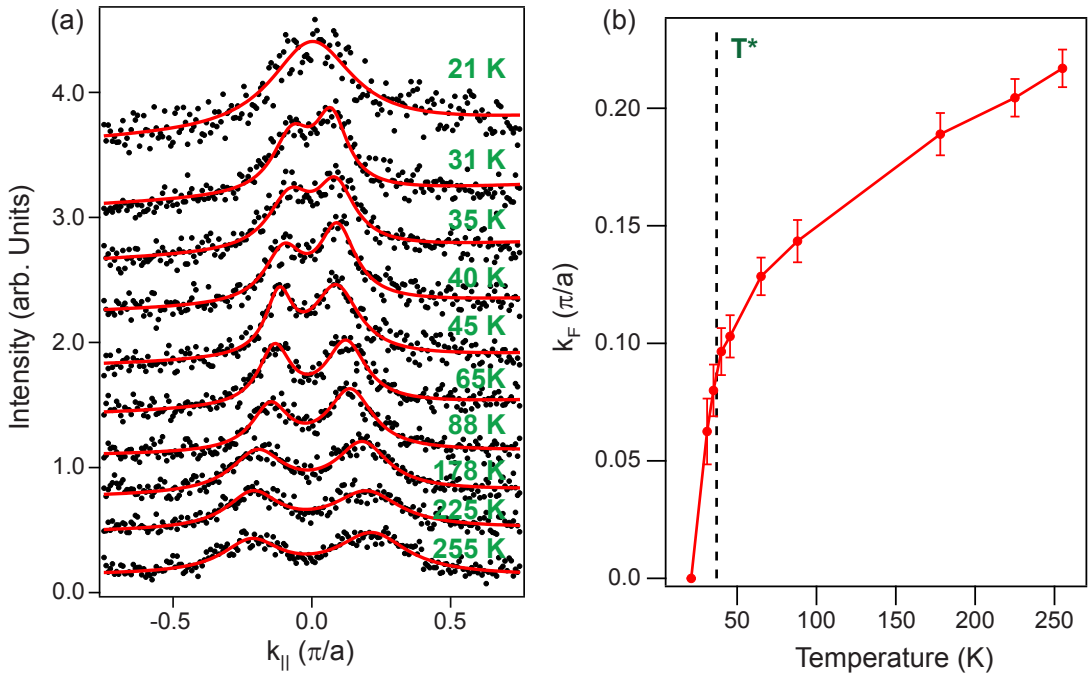

Figure 8.10: Change in Fermi wavevector of the electron pocket at γ with temperature in $YbAl_3$ a) MDCs taken at E_F at different temperatures with correspomding fits from which Fermi wavevector k_F is estimated and is plotted as a function of temperature in b).

8.3 Connection between r-space and k-space electronic structure in $YbAl_3$

To make a quantitative connection between the observed change in band filling and the estimated change in the Yb valence, we calculate the change in occupation of the electron pocket from its Fermi wave vector (k_F) as a function of temperature. k_F is determined from the momentum distribution curves (MDCs) taken at the Fermi Energy (E_F).

In Fig. 8.10, we show MDCs at E_F taken at different sample temperatures

along with their corresponding fits where the spectral profiles are fitted with two lorentzians and a linear background.(eqn. 2.25,2.26) We note that our incident photon energy samples the two dimensional momentum space centered at Γ. Therefore, our obtained k_F value should correspond to the extremal k_F for the electron pocket. Due to three dimensional cubic crystal structure of $YbAl_3$ we assume a spherical geometry for the electron pocket and calculate corresponding Luttinger volume as $\frac{4}{3}\pi k_F^3$.

In Fig. 8.11 a) we plot, both the estimated change in the Luttinger volume and the average Yb valence obtained from XPS measurements that reveals a striking correspondence between the two quantities. Our experimental result thus provides first direct microscopic evidence that the Kondo screening of the 4*f* moments at the Yb sites by the conduction electrons (here, an electron pocket centered at Γ) of primarily Al *3p* and Yb *5d* character, leads to a change in their band filling and is manifested as a reduction of the local Yb valence, thus establishing a connection between the two quantities. This situation is illustrated in Fig. 8.11 b). Such a temperature dependent behavior should be generic to any mixed valence system. Indeed, recent RIXS measurements have suggested some alteration in band fillings at the the first order phase transition in $YbInCu_4$, across which Yb valence is known to undergo a significant change.[230] Self-consistent mean field calculations taking into account changes in chemical potential predicts a slower crossover from the local moment regime to the Kondo screened regime than what is predicted by Single Impurity Anderson model, similar to experimental observations in $YbAl_3$ further underscoring the importance of the observed chemical potential shift.[167, 32, 231, 232]

Our experimental result also reconciles the necessity to shift the chemical

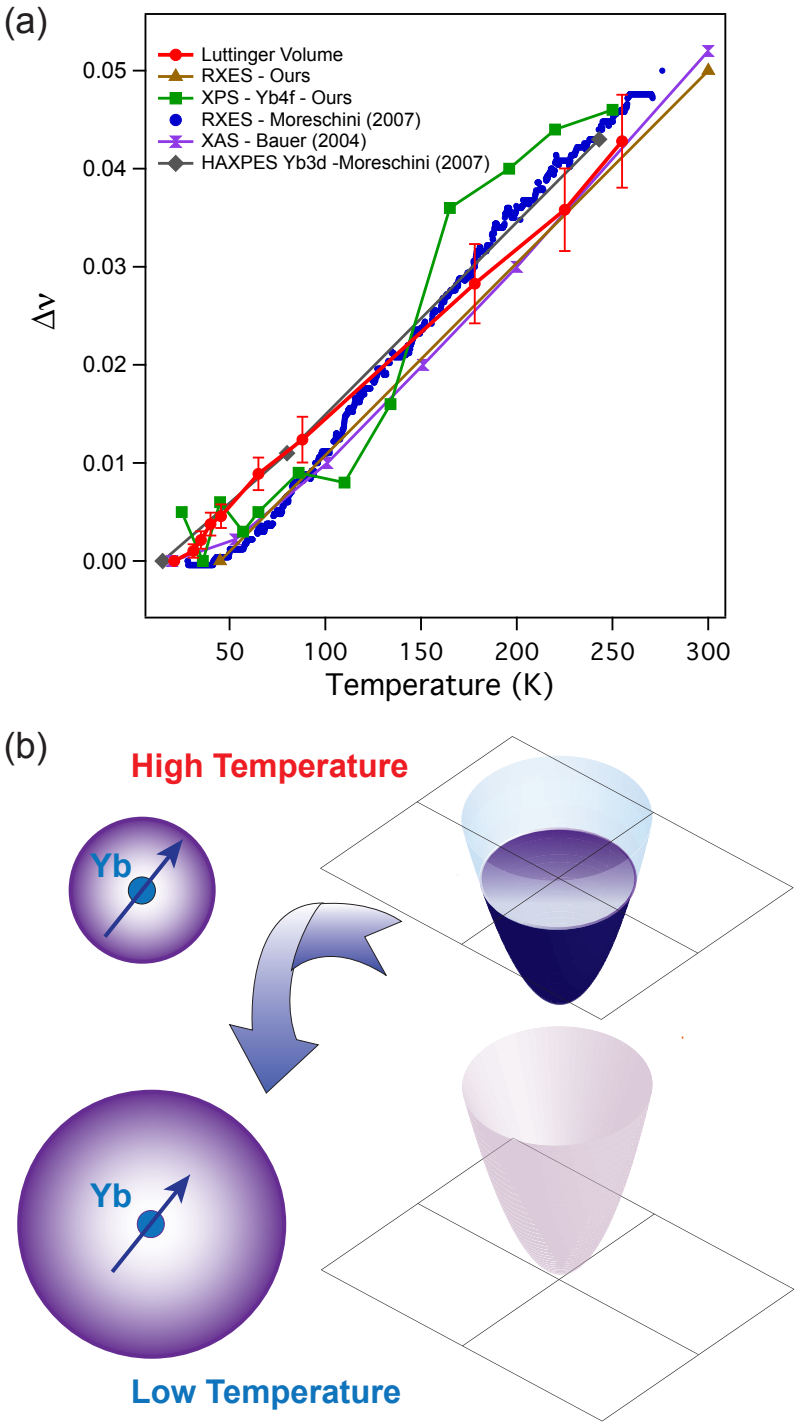

Figure 8.11: a) Variation of Yb valence as obtained from high energy spectroscopies and Luttinger volume of the electron pocket centered at Γ as obtained from ARPES measurements revealing a remarkable corresp[ondence between the two quantities. b) Cartoon illustrating change in electronic structure with temperature in $YbAl_3$.

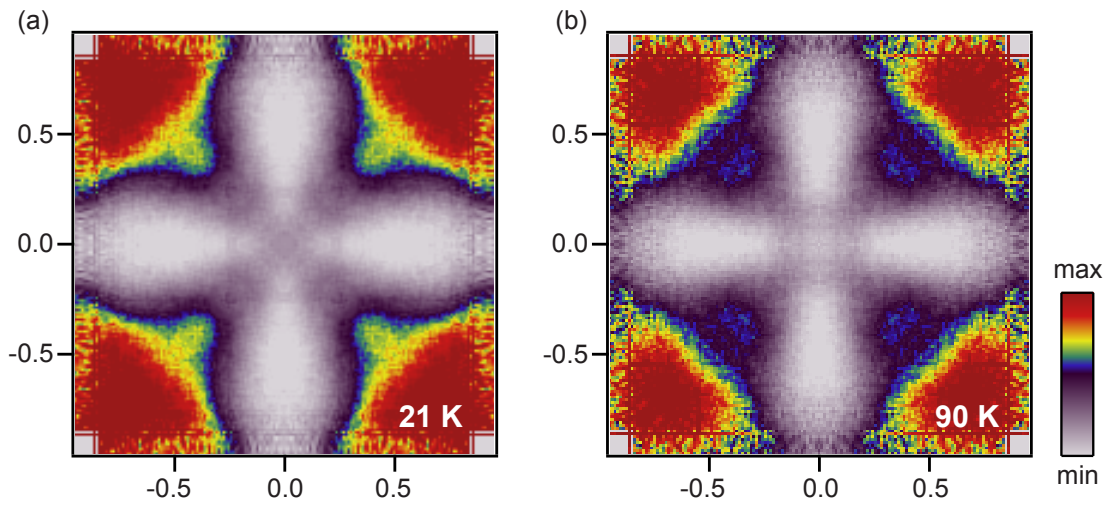

Figure 8.12: $YbAl_3$ Fermi surface map at $k_z = \Gamma$ at a) 21 K b) 90 K

potential in band structures obtained from ab-initio calculations in order to reproduce results from quantum oscillation measurements in $YbAl_3$ taken at low temperatures.[170] In Figs. 8.12 a) and b) we show associated temperature dependent changes of the Fermi surface topology. In addition to a reduction in size of the electron pocket that mostly accounts for the observed change in Yb valence, an increase in size of the 4*f* derived hole pocket can also be observed at a lower temperature. This indicates that an increase in contribution of holes to the Fermi Sea as Kondo screening is enhanced at lower temperatures, as is expected from existing theories of the Kondo lattice systems. A recent temperature dependent ARPES study could not observe any change in the Fermi surface topology across the Kondo temperature in $YbRh_2Si_2$.[233] Although we cannot provide any definitive reason for such an observation, we would like to highlight differences between $YbRh_2Si_2$ and $YbAl_3$ studied here. Energy scale in $YbAl_3$ is much higher than in $YbRh_2Si_2$ with the single ion Kondo temperature $T_K \approx 670$, while it is only 25 K for $YbRh_2Si_2$. Furthermore, although technically $YbRh_2Si_2$ is still in the mixed valence regime, the change in Yb valence from 100

K to 1 K , the temperature range accessed by the above mentioned experiment, is much smaller than in $YbAl_3$. While we have unambiguously demonstrated how changes in band filling is related to the changes in Yb valence in $YbAl_3$, which should be ubiquitous in any mixed valence compound, the details of $YbRh_2Si_2$ band structure coupled with a tiny change in Yb valence might make temperature dependent changes in its band structure difficult to detect. However, even for compounds in the heavy fermion regime, where the charge fluctuations are frozen out, change in Fermi surface topology is expected[28, 54], which should be investigated in the future.

CHAPTER 9

DIMENSIONALITY TUNING OF THE KONDO LATTICE

In the previous chapters we have demonstrated how Kondo screening at the Yb 4*f* moments by the conduction (Al3*p* - Yb5*d*) electrons brings about a profound change in its electronic structure. At the same time, we have established the feasibility and efficacy of combining high resolution spectroscopy with advanced synthesis tools in understanding microscopic mechanisms responsible for the exotic properties of the Kondo lattice systems. In this chapter, we harness the full potential of our novel approach by designing artificial quantum structures involving Kondo lattice layers and use *in situ* ARPES to visualize how Kondo coherence is destroyed at reduced dimensions. Our approach provides the first direct visualization of effective hybridization control by artificial structural modifications in *f* electron systems.

9.1 Film Growth and Characterization

To control the effective dimensionality of $YbAl_3$ thin films, we fabricated ultra-thin $YbAl_3$ layer, as well as superlattice films, where few atomic layers of $YbAl_3$ are interrupted by $LuAl_3$ layers. Film growth was performed in a similar manner as has been described in Chapter 6. For both ultra-thin $YbAl_3$ layers and superlattice films, we used aluminum and $LuAl_3$ as buffer layers, as has been used for the synthesis of thick $YbAl_3$ films. A rough estimation of the time required for a monolayer formation was obtained from flux calibration using QCM. This was fine tuned by growing test samples of desired nominal thicknesses and comparing with the actual thickness values estimated from x-ray reflectivity measurements.

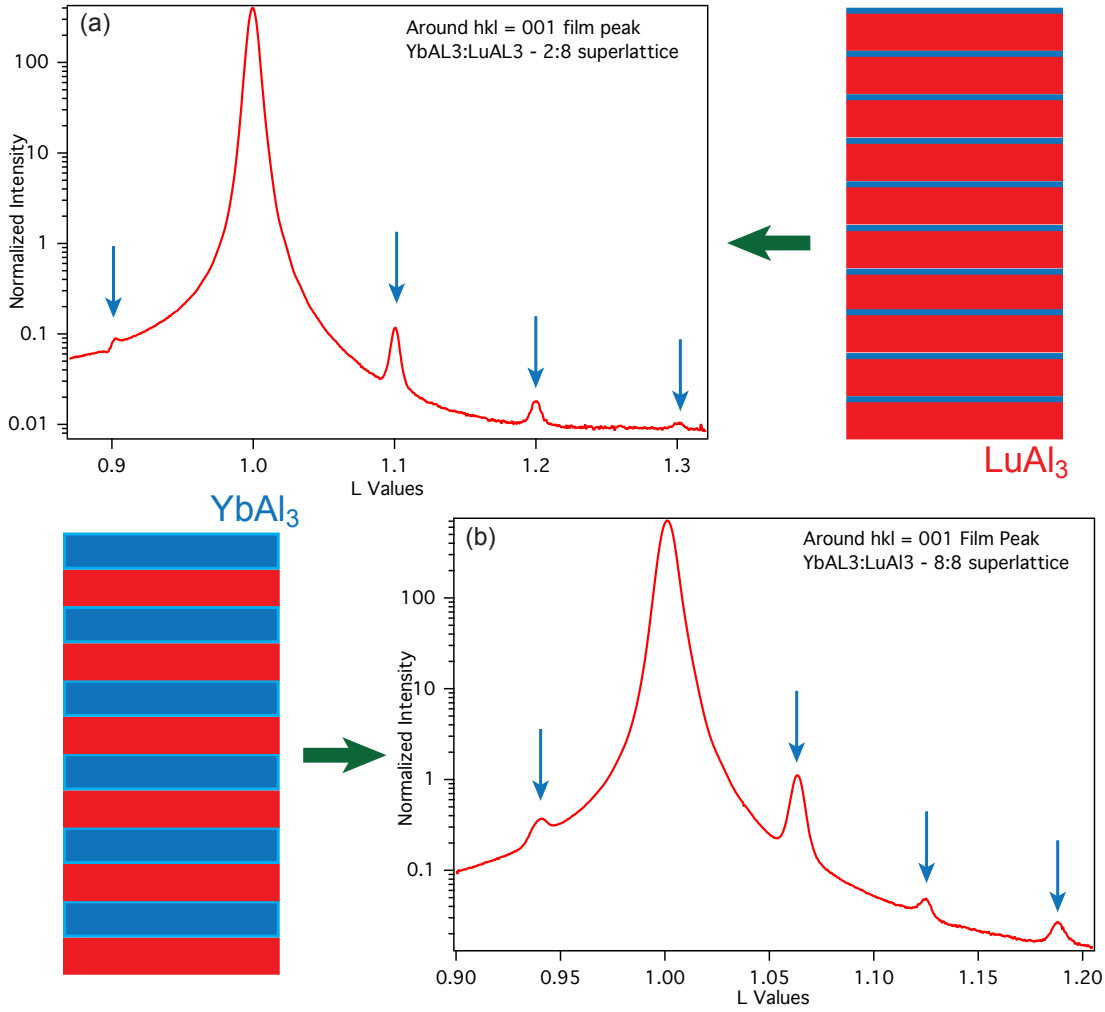

Figure 9.1: L-scans along 001 film direction for a) 2:8 superlattice, where, 2 atomic layers of $YbAl_3$ are alternated with 8 atomic layers of $LuAl_3$ b) 8:8 superlattice, where 8 atomic layers of $YbAl_3$ are alternated with 8 atomic layers of $LuAl_3$. Superlattice diffraction peaks are indicated by blue arrows. Presence of superlattice diffraction peaks at the correct $(0,0,\ell)$ values confirms correct oredering of the atomic layers in the superlattice structure.

In addition to confirming ordered structure both in the bulk and at the film surface, and epitaxial orientation with respect to MgO substrate, as has been established for thick $YbAl_3$ films (Fig. 6.9, 6.10), additional diffraction peaks were identified for the $YbAl_3$ superlattice thin films establishing the correct ordering of the layers along the 001 direction. Intensity of the superlattice diffraction peaks depends on the density difference between the two dissimilar atomic layers present in the superlattice structure. As molar mass of $YbAl_3$ and $LuAl_3$, atomic layers constituting $YbAl_3$ superlattice structures, is almost identical (254 gm/mol for $YbAl_3$, 256 gm/mol for $LuAl_3$), intensity of the superlattice diffraction peaks is too weak to be resolved by standard x-ray diffraction apparatus. To identify superlattice diffraction peaks in our superlattice thin films, we performed diffraction experiment at the A2 beamline using high intensity 15 KeV x-rays at the Cornell High Energy Synchrotron Source (CHESS). In Fig. 9.1, we show representative line scans along 001 direction around (001) Bragg peak for *'2:8'* and *'8:8'* superlattice thin films, where two and eight atomic layers of $YbAl_3$ are interrupted by eight atomic layers of $LuAl_3$, respectively. Presence of superlattice diffraction peaks at the correct (0,0,ℓ) positions confirms that the superlattice films have the desired periodicity along the out of plane direction.

9.2 ARPES Results

In situ ARPES measurements were performed by transferring the samples immediately after growth (within 20 minutes) into the measurement chamber maintaining a pressure better than 5×10^{-10} torr during the entire transfer process. In Fig. 9.2, we compare evolution of spectral intensity maps obtained from identical ARPES cuts at 21 K, along (0,0 - π,0), for a series of films viz. 25 nm

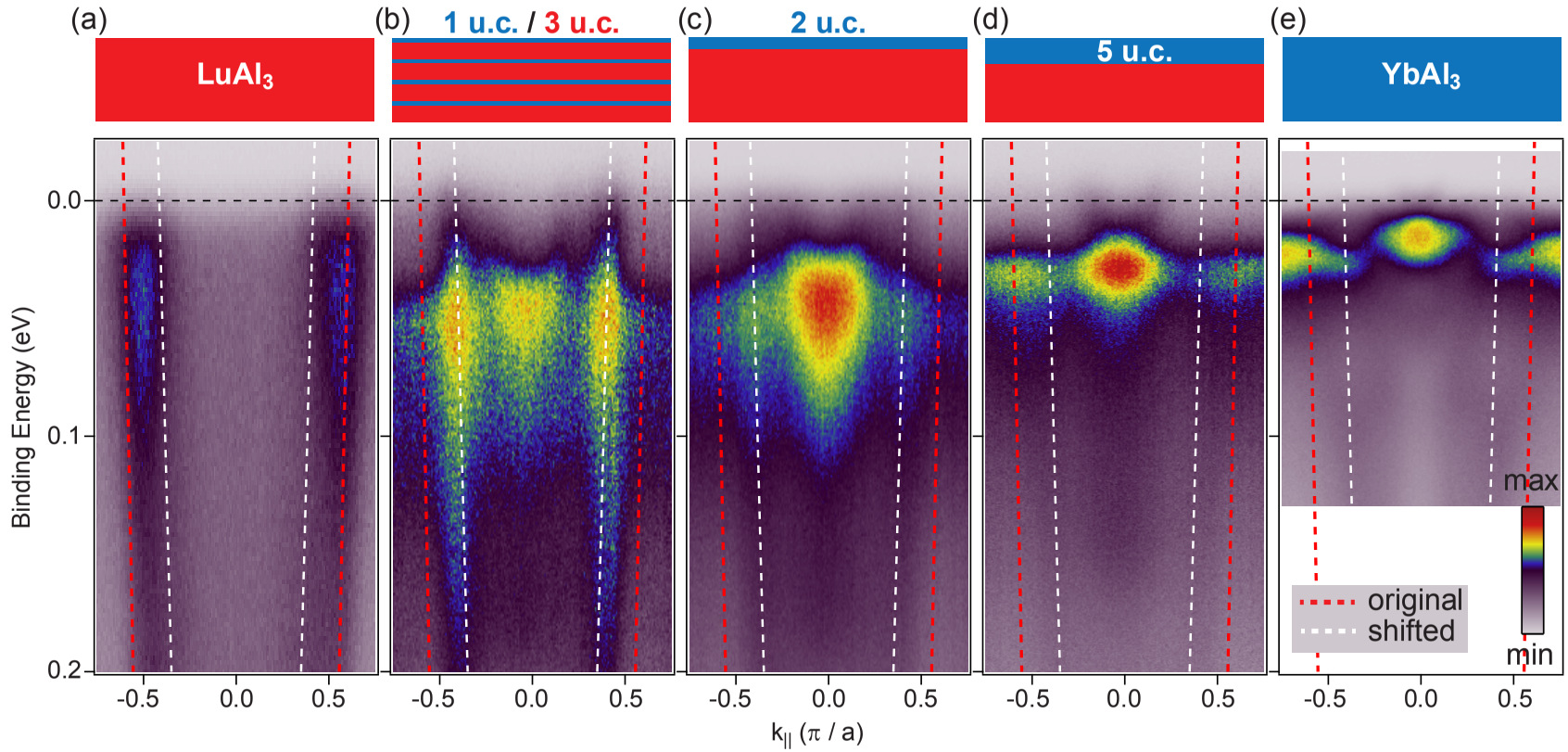

Figure 9.2: Schematic of the film structure and corresponding spectral intensity maps along (0,0 - π,0) taken at 21 K using 21.2 eV excitation energy for a) 25 nm thick $LuAl_3$ b) 1:3 $YbAl_3$: $LuAl_3$ superlattice with 25 repeat units, terminated with 1 u.c. of $YbAl_3$ on top c) 2 u.c. thick $YbAl_3$ d) 5 u.c. thick $YbAl_3$ e) 25 nm thick $YbAl_3$. All the films have 25 nm thick $LuAl_3$ and 1.6 nm of aluminum as buffer layer. Calculated dispersion of the electron pocket centered at (0,0) for $LuAl_3$, as described in Chapter 7 overlaid on top (red dotted line). The electron pocket is displaced in binding energy according to the estimated chemical potential shift between $LuAl_3$ and $YbAl_3$, as shown in Fig. 7.7 and is overlaid on top (white dotted line).

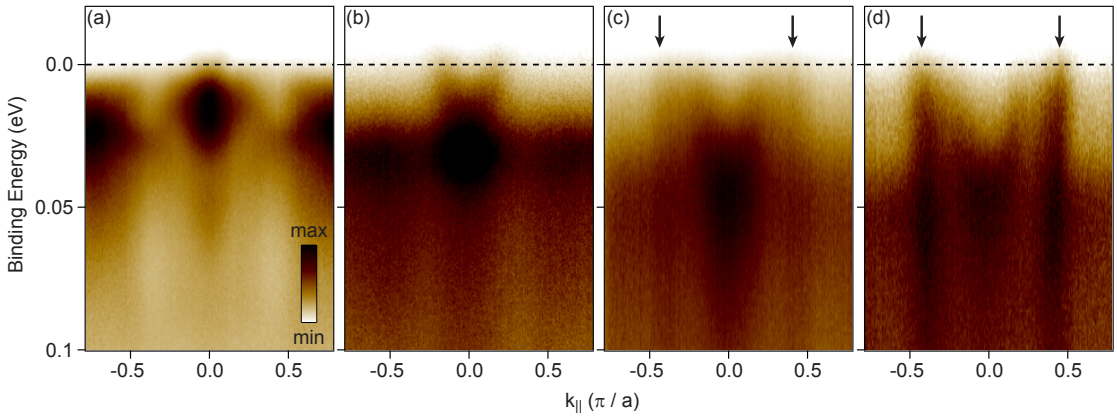

Figure 9.3: Near E_F electronic structure in a) 25 nm thick $YbAl_3$ b) 5 u.c. $YbAl_3$ c) 2 u.c. thick $YbAl_3$ d) 1:3 $YbAl_3$ $LuAl_3$ superlattice with 25 repeat units and terminated with 1 u.c. of $YbAl_3$. All the films have 25 nm thick $LuAl_3$ and 1.6 nm of aluminum as buffer layer. Additional Fermi crossings is seen (indicated by black arrows) in panels c) and d) due to suppression of Kondo coherence at reduced dimensions. As $YbAl_3$ layers are made thicker conduction electrons hybridize with the the renormalized 4*f* states forming dispersive heavy bands as seen in panel a). All measurements are performed at 21 K with 21.2 eV excitation energy.

$LuAl_3$, *1:3* $YbAl_3$ / $LuAl_3$ superlattice film with 25 repeat units terminated with 1 unit cell(u.c.) of $YbAl_3$ on top, 5 u.c. of $YbAl_3$ ($\approx$ 2.1 nm), 2 u.c. of $YbAl_3$ ($\approx$ 0.82 nm), and a 25 nm thick $YbAl_3$ film. All of them are grown on MgO 100 and have identical buffer layers of 25 nm thick $LuAl_3$ and 1.6 nm thick aluminum. Dramatic alterations of the near E_F electronic structure is seen across the films with different compositions with the tuning of effective dimensionality of the $YbAl_3$ layers. A clear shift in chemical potential is identified from the shift in binding energy of the electron-like pocket centered at (0,0) between the 25 nm thick $LuAl_3$ film and the rest that have various thicknesses of $YbAl_3$ layers on top (Fig. 9.2). Furthermore, the estimated shift in binding energy is in remarkable agreement with what has been deduced in Fig. 7.7.

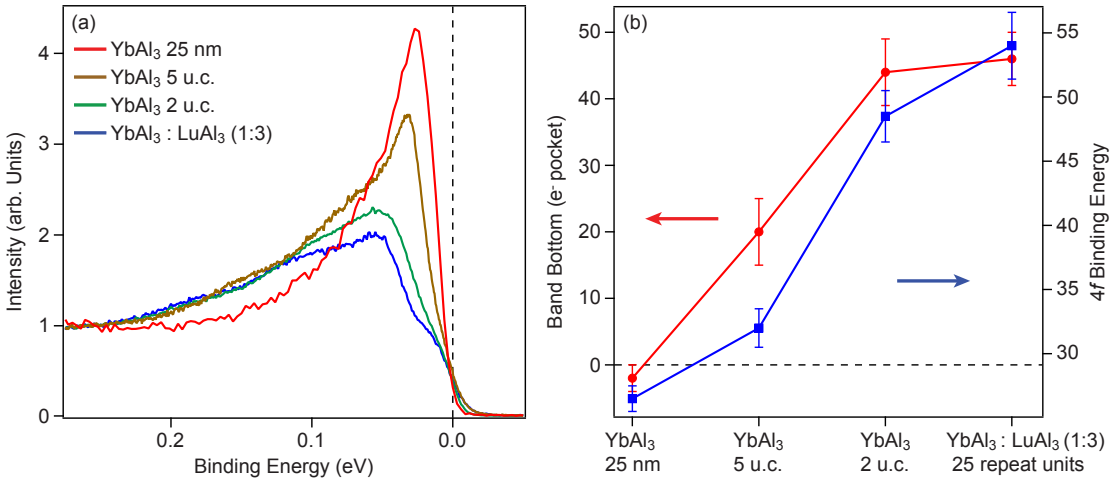

Figure 9.4: Evolution of the light and heavy bands with effective dimensionality tuning in a Kondo lattice system. a) Energy distribution curves integrated over a momentum region 0.63 π/a and 0.73 π/a for different thin film structures. A coherent Kondo peak develops with increasing $YbAl_3$ layer thickness. b) Evolution in binding energy of the renormalized 4*f* states and the small electron-like pocket centered at (0,0) with $YbAl_3$ layer thickness. With the development of coherence the 4*f* spectral weight shifts towards lower binding energy pushing the electron pocket closer to E_F. All measurements are performed at 21 K with 21.2 eV excitation energy.

This indicates that the additional Fermi surface crossings, observed in the 2 monolayer thick $YbAl_3$ and the *1:3* superlattice film, clearly seen in Figure 9.3, is due to the un-hybridized $YbAl_3$ bands because of suppression of Kondo coherence at reduced dimensions. Simultaneous observation of these Fermi crossings from the un-hybridized $YbAl_3$ bands and a small electron pocket centered at (0,0), resulting ostensibly from the hybridization process (as described in detail in earlier chapters, particularly Chapter 7), in the same film is most likely indicative of a mixed phase, where both hybridized and un-hybridized bands co-exist. As $YbAl_3$ layers are made thicker, intensity of the Fermi crossings diminish along with a reduction in spectral line-width of the renormalized Yb 4*f*

states. At 5 monolayer $YbAl_3$ thickness, Fermi crossings from the original unhybridized bands are no longer observed, while in the thick limit renormalized Yb 4*f* states themselves become dispersive as they become fully coherent (Fig. 8.9, 9.2, 9.3). A coherent Kondo peak develops as $YbAl_3$ layer thickness is increased (fig.9.4 a)). Binding energy of the renormalized Yb 4*f* spectral weight also moves closer to E_F. This is also accompanied by a change in occupation of the small electron-like pocket, centered at (0,0). As shown in Fig. 9.4 b), the band-bottom of the electron-like pocket moves from a binding energy of 46 ± 4 meV for the 1:3 $YbAl_3$ / $LuAl_3$ superlattice film to above E_F in the 25 nm thick $YbAl_3$ film at 21 K. This again reinforces the fact that the occupation of the electron-like pocket is tied to the nature of the Yb 4*f* states. How these changes in low-energy electronic structure is related to the effective Yb valence and Kondo temperature in these systems, is of immense interest and will be investigated in the future.

BIBLIOGRAPHY

[1] P. W. Anderson, *Science*, 177, 393 (1972)

[2] S. Hüfner, *Photoelectron Spectroscopy*, Springer-Verlag, Berlin (1995)

[3] S. Hüfner (ed.), *Very High Resolution Photoelectron Spectroscopy*, Springer, Berlin (2007)

[4] H. Hertz, *Ann. Phys. (Berlin)*, 267, 983 (1887)

[5] P. Lenard, *Ann. Phys. (Berlin)*, 2, 359 (1900)

[6] P. Lenard, *Ann. Phys. (Berlin)*, 313, 149 (1902)

[7] A. Einstein, *Ann. Phys. (Berlin)*, 322, 132 (1905)

[8] M. Planck, *Ann. Phys. (Berlin)*, 309, 553 (1901)

[9] R. A. Millikan, *Phy. Rev.*, 7, 355 (1916)

[10] C. N. Berglund and W. E. Spicer, *Phy. Rev.*, 136, A1030 (1964)

[11] C. N. Berglund and W. E. Spicer, *Phy. Rev.*, 136, A1044 (1964)

[12] C. N. Berglund and W. E. Spicer, *Phy. Rev. Lett.*, 12, 97 (1964)

[13] N. V. Smith, M. M. Traum, and F. J. DiSalvo *Phy. Rev. Lett.*, 32, 1241 (1974)

[14] N. V. Smith, M. M. Traum, and F. J. DiSalvo *Solid State Comm.*, 15, 211 (1974)

[15] A. Damascelli, Z. Hussain, and Z. X. Shen *Rev. Mod. Phys.*, 75, 473 (2003)

[16] J. D. Denlinger et. al. *J. Electron. Spectrosc. Relat. Phenom.*, 117-118, 347 (2001)

[17] M. P. Seah and W. A. Dench, *Surf. Interface Anal.*, 1, 2 (1979)

[18] V. N. Strocov, *J. Electron. Spectrosc. Relat. Phenom.*, 130, 65 (2003)

[19] E. J. Monkman, Ph.D. Thesis, Cornell University (2014)

[20] P. A. M. Dirac, *Proc. R. Soc. Lond.*, A114, 243 (1927)

[21] M. Randeria et. al., *Phys. Rev. Lett.*, 74, 4951 (1995)

[22] J. D. Koralek et. al., *Phys. Rev. Lett.*, 96, 01705 (2006)

[23] G. D. Mahan, *Many-particle Physics*, Kluwer Academic/Plenum Publishers (2000)

[24] R. Mattuck, *A Guide to Feynman Diagrams in the Many-Body Problem*, McGraw-Hill, New York (1976)

[25] A. Roth, *Vacuum Technology*, North-Holland, Amsterdam (1982)

[26] A. A. Kordyuk et. al., *Phys. Rev. B*, 71, 214513 (2005)

[27] D. A. Shirley, *Phys. Rev. B*, 5, 4709 (1972)

[28] A. C. Hewson, *The Kondo Problem to Heavy Fermions*, Cambridge University Press (1993)

[29] F. Steglich, *Physica B+C*,130, 145-150 (1985)

[30] Y. Onuki and T. Komatsubara, *J. Mag. Mat.*, 63-64, 281 (1987)

[31] G. R. Stewart, Z. Fisk, and M. S. Wire, *Phys. Rev. B* 30, 482 (1984)

[32] A. Cornelius et. al. *Phys. Rev. Lett.*, 88, 117201 (2002)

[33] C. Geibel et. al., *Zeit. Phys. B.* 83, 305 (1991)

[34] C. Geibel et. al., *Zeit. Phys. B.* 84, 1 (1991)

[35] F. Steiglich et. al., *Phys. Rev. Lett.* 43, 1892 (1976)

[36] H. R. Ott et. al., *Phys. Rev. Lett* 50, 1595 (1983)

[37] H. R. Ott et. al., *Phys. Rev. Lett* 52, 1915 (1984)

[38] C. Petrovic et. al., *J. Phys.: Condens. Matter* 13, L337 (2001)

[39] V. A. Sidorov et. al., *Phys. Rev. Lett.* 89, 157004 (2002)

[40] K. Kim et. al., *Phys. Rev. Lett.* 91, 256401 (2003)

[41] T. T. M. Palstra et. al., *Phys. Rev. Lett.* 55, 2727 (1985)

[42] P. Gegenwart, Q. Si, and F. Steglich, *Nat. Phys.* 4, 186 (2008)

[43] Q. Si and S. Paschen, *Phys. Status Solidi B* 250, 425-438 (2013)

[44] O. Stockert and F. Steglich, *Annu. Rev. Condens. Matter Phys.* 2, 79 (2011)

[45] P. Nozières and D. Pines, *Theory of Quantum Liquids*, Perseus Books, Cambridge, Massachusetts (1999)

[46] P. Coleman, *arxiv:cond-mat*, 0612006v3 (2007)

[47] C. M. Varma, *Rev. Mod. Phys.*, 48, 219 (1976)

[48] W. J. deHaas, J. de Boer, and G. J. van dën Berg, *Physica*, 1, 1115 (1933)

[49] A. M. Clogston et. al., *Phys. Rev.*, 125, 541 (1962)

[50] M. Sarachik, E. Corenzwit, and L. D. Longinotti, *Phys Rev.*, 135, A1041 (1964)

[51] R. H. White and T. H. Geballe, *Solid State Physics*, Academic Press, New York, vol 15, p283 (1979), volume 15, p. 283.

[52] P. W. Anderson, *Phys. Rev.*, 124, 41 (1961)

[53] A. Blandin and J. Friedel, *J. Phys. Radium*, 19, 573 (1958)

[54] P. Coleman, *Introduction to Many-Body Physics*, Cambridge University Press (2015)

[55] B. Coqblin and J. R. Schrieffer, *Phys. Rev.*, 185, 847 (1969)

[56] J. R. Schrieffer and P. Wolff, *Phys. Rev.*, 149, 491 (1966)

[57] J. Kondo, *Prog. Theo. Phys.*, 28, 772 (1962)

[58] J. Kondo, *Prog. Theo. Phys.*, 28, 772 (1964)

[59] K. G. Wilson, *Rev. Mod. Phys.*, 47, 773 (1976)

[60] P. Coleman, *arxiv:cond-mat*, 1509.05769v1 (2015)

[61] A. A. Abrikosov, *Soviet Phys. JETP*, 21, 660 (1965)

[62] H. Suhl, *Phys. Rev.*, 138, A515 (1965)

[63] J. W. Allen et. al., *Phys. Rev.*, 28, 5347 (1983)

[64] J. W. Allen et. al., *Phys. Rev. Lett.*, 2635, 54 (1985)

[65] D. Langreth, *Phys. Rev.*, 150, 516 (1966)

[66] J. S. Langer and V. Ambegaokar, *Phys. Rev.*, 121, 1090 (1961)

[67] B. Horvatić, D. Sokcević, and V. Zlatić, *Phys. Rev. B*, 36, 675 (1987)

[68] S. Doniach, *Physica B*, 91, 231 (1977)

[69] T. Kasuya, T., *Prog. Theo. Phys.*, 16, 45 (1956)

[70] M. A. Ruderman and C. Kittel, *Phys. Rev*, 78, 275 (1950)

[71] K. Yosida, *Phys. Rev.*, 106, 896 (1957)

[72] S. V. Dordevic et. al., *Phys. Rev. Lett.*, 86, 684 (2001)

[73] H. J. Im et. al., *Phys. Rev. Lett.*, 100, 176402 (2008)

[74] A. R. Schmidt et. al., *Nature*, 465, 570 (2010)

[75] J. E. Crow, R. P. Guertin (ed.), and T. W. Mihalisin, *Crystallinie Electric Field and Structural Effects in f-electron Systems*, Plenum Press, New York (1980)

[76] S. Nakatsuji, D. Pines, and Z. Fisk, *Phys. Rev. Lett.*, 92, 016401 (2004)

[77] Y. -F. Yang and D. Pines, *Phys. Rev. Lett.*, 100, 096404 (2008)

[78] Y. -F. Yang et. al., *Nature*, 454, 611 (2008)

[79] Y. -F. Yang and D. Pines, *Proc. Natl. Acad. Sci. USA*, 109, 45, E3060 (2012)

[80] K. R. Shirer et. al., *Proc. Natl. Acad. Sci. USA*, 45, 3067 (2012)

[81] J. A. Mydosh and P. M. Oppeneer, *Rev. Mod. Phys.*, 83, 1301 (2011)

[82] S. Chatterjee et al., *Phys. Rev. Lett.*, 110, 186401 (2013)

[83] M. B. Maple, *Phys. Rev. Lett.*, 56, 185 (1986)

[84] T. T. M. Palstra, A. A. Menovsky, and J. A. Mydosh, *Phys. Rev. B* 33, 6527 (1986)

[85] W. Schlabitz et. al., *Z. Phys. B: Condens. Matter* 62, 171 (1986)

[86] M. Jaime et. al. , *Phys. Rev. Lett.*, 89, 287201 (2002)

[87] J. Y. Jo et. al., *Phys. Rev. Lett.*, 98, 166404 (2007)

[88] S. Y. Oh et. al., *Phys. Rev. Lett.*, 98, 016401(2002)

[89] S. Uemura et. al., *J. Phys. Soc. Japan*, 74, 2667 (2005)

[90] H. Amitsuka et. al., *J. Magn. Magn. Mater*, 310, 214 (2007)

[91] E. Hassinger et. al., *Phys. Rev. B*, 77, 115117 (2008)

[92] J. Schoenes et. al., *Phys. Rev. B*, 35, 5375 (1987)

[93] T. Mason et. al., *Phys. Rev. Lett.*, 65, 3189 (1990)

[94] T. Ito et. al., *Phys. Rev. B*, 60, 19, 13390 (1999)

[95] P. Thalmeier and G. Zwicknagl, *Unconventional superconductivity and magnetism in lanthanide and actinide intermetallic compounds*, vol 34, 135287, Elsevier (2004)

[96] C. R. Wiebe et. al., *Nat. Phys.*, 3, 96 (2007)

[97] P. Aynajian et. al., *Proc. Natl. Acad. USA*, 107, 10383 (2010)

[98] J. A. Janik, *Ph. D. Thesis*, Florida State University (2004)

[99] M.M.Altarawneh et. al., *Phys. Rev. Lett.*, 108, 066407 (2012)

[100] P. Chandra, R. Flint, and P. Coleman, *Nature*, 493, 621 (2013)

[101] M. Werwinski et. al., *Phys. Rev. B*, 90, 064430 (2014)

[102] J. -Q. Meng et. al., *Phys. Rev. Lett.*, 111, 127002 (2013)

[103] F. L. Boariu et. al., *Phys. Rev. Lett.*, 110, 156404 (2013)

[104] C. H. Booth et. al., *Phys. Rev. B*, 94, 045121 (2016)

[105] J. R. Jeffries et. al., *Phys. Rev. B*, 82, 033103 (2010)

[106] C. Broholm et. al., *Phys. Rev. Lett.*, 58, 1467 (1987)

[107] C. Broholm et. al., *Phys. Rev. B*, 43, 12809 (1991)

[108] D. E. MacLaughlin et al., *Phys. Rev. B* 37, 3153 (1988)

[109] G. J. Nieuwenhuys, *Phys. Rev. B*, 35, 5260 (1987)

[110] P. Santini and G. Amoretti, *Phys. Rev. Lett.*, 73, 1027 (1994)

[111] Y. Okuno and K. Miyake, *J. Phys. Soc. Jpn.*, 67, 2469 (1998)

[112] P. Chandra et. al., *Nature*, 417, 831 (2002)

[113] A. Kiss and P. Fazekas, *Phys. Rev. B*, 71, 054415 (2005)

[114] K. Haule and G. Kotliar, *Nat. Phys.*, 5, 796 (2009)

[115] F. Cricchio et. al., *Phys. Rev. Lett.*, 103, 107202 (2009)

[116] H. Harima, K. Miyake and J. Flouquet, *J. Phys. Soc. Jpn.*, 79, 033705 (2010)

[117] P. Thalmeier and T. Takimoto, *Phys. Rev. B*, 83, 165110 (2011)

[118] H. Kusunose and H. Harima, *J. Phys. Soc. Jpn.*, 80, 084702 (2011)

[119] H. Ikeda et. al., *Nat. Phys.*, 528 (2012)

[120] H. -H. Kung et. al., *Science*, 347, 1339 (2015)

[121] A. Viroszek, K. Maki, and B. Dóra, *Int. J. Mod. Phys. B*,16, 1667 (2002)

[122] S. Elgazzar et. al., *Nat. Mater.*, 8, 337 (2009)

[123] Y. Dubi and A. V. Balatsky, *Phys. Rev. Lett.*, 106, 086401 (2011)

[124] C. Pépin et. al., *Phys. Rev. Lett.*, 106, 106601 (2011)

[125] P. S. Riseborough, B. Coqblin, and S. G. Magalhaes, *Phys. Rev. B*, 85, 165116 (2012)

[126] T. Das, *Sci. Rep.*, 2, 596 (2012)

[127] C. -H. Hsu and S. Chakravarty, *Phys. Rev. B*, 87, 08511 (2013)

[128] N. P. Butch, *Phys. Rev. B*, 91, 035128 (2015)

[129] R. Okazaki et. al., *Science*, 331, 430 (2011)

[130] S. Tonegawa et. al., *Phys. Rev. Lett.*, 109, 036401 (2012)

[131] T. Shibauchi and Y. Matsuda, *Phys. C*, 481, 229 (2012)

[132] S. Tonegawa et. al., *Phys. Rev. B*, 88, 245131 (2013)

[133] S. Kambe et. al., *Phys. Rev. Lett.*, 110, 246406 (2013)

[134] S. Tonegawa et. al., *Nat. Commun.*, 5, 4188 (2014)

[135] C. Tabata et. al., *Philos. Mag.*, 94, 32-33 (2014)

[136] P. Das et. al., *New. J. Phys.* 15, 05303 (2013)

[137] K. A. Ross *Phys. Rev. B*, 89, 155122(2014)

[138] C. Pfleiderer, J. A. Mydosh, and M. Vojta, *Phys. Rev. B*, 74, 104412 (2006)

[139] S. Takagi et. al., *J. Phys. Soc. Jpn.*, 81, 114710 (2012)

[140] A. Amato et. al., *J. Phys. Condens. Matter*, 16, S4403 (2004)

[141] E. R. Schlemm et. al., *Phys. Rev. B*, 91, 140506 (2015)

[142] J. D. Denlinger, private communication.

[143] A. F. Santander-Syro et al., *Nature Phys.* 5, 637(2009).

[144] F. L. Boariu et al., *J. Electron Spectrosc.*, 181, 82(2010)

[145] R. Yoshida et al., *Phys. Rev. B*, 82, 205108 (2010)

[146] R. Yoshida et al., *Phys. Rev. B*, 85, 241102 (2012)

[147] R. Yoshida et al., *Sci. Rep.*, 3, 3750 (2013)

[148] E. Hassinger et al., *Phys. Rev. Lett.*, 105, 216409 (2010)

[149] H. Ohkuni et al., *Philos. Mag. B*, 79, 1045 (1999)

[150] H. Shishido et al., *Phys. Rev. Lett.*, 102, 156403 (2009)

[151] H. Pfau et al., *Phys. Rev. Lett.*, 110, 256403 (2013)

[152] D. Aoki et al., *J. Phys. Soc. Jpn.*, 81, 074715 (2012).

[153] U. Nagel *et al.*, PNAS doi/10.1073/pnas.1208249109 (2012).

[154] G. L. Dakovski et al., *Phys. Rev. B*, 84, 161103 (2011).

[155] D. A. Bonn et al., *Phys. Rev. Lett.*, 61, 1305 (1988).

[156] J.S. Hall et al., *Phys. Rev. Lett.* 86, 035132 (2012).

[157] J. R. Jeffries et al., *Phys. Rev. Lett.*, 99, 217207 (2007)

[158] S. A. M. Mentink et al., *Phys. Rev. B* 53, R6014 (1996)

[159] T. Yuan et al., *Phys. Rev. B*, 86, 035129 (2012).

[160] J. M. Lawrence et al., *Phys. Rev. B*, 49, 1627 (1994)

[161] L. Moreschini et al., *Phys. Rev. B*, 75, 035113 (2007)

[162] S. Suga et al., *J. Phys. Soc. Jpn.*, 74, 2880 (2005).

[163] J. Yamaguchi et al., *New J. Phys.*, 9, 317 (2007)

[164] R. S. Kumar et al., *Phys. Rev. B*, 78, 075117 (2008).

[165] E. E. Havinga, K. H. J. Buschow, and H. J. van Daal, *Solid State Commun.*, 13, 621 (1973)

[166] L. H. Tjeng et al.,*Phys. Rev. Lett.* 71, 1419 (1993)

[167] S. Burdin and V. Zlatic, *Phys. Rev. B*, 79, 115139 (2009)

[168] E. Bauer et al., *Phys. Rev. B*, 69, 125102 (2004).

[169] T. Ebihara et al., *Phys. Rev. Lett.*, 90, 166404 (2003)

[170] T. Ebihara et al., *J. Phys. Soc. Jpn.*, 69, 895 (2000)

[171] P. Wahl et al., *Phys. Rev. B*, 84, 245131 (2011).

[172] R. I. R. Blyth et al., *Phys. Rev. B*, 48, 9497 (1993).

[173] H. Shishido et al., *Science*, 327, 980 (2010).

[174] E. Wang et al., *Nat. Phys.*, 9, 621 (2013)

[175] S. Chatterjee et al., *J Appl. Phys.*, 120, 035105 (2016)

[176] M. Shimozawa et al., *Phys. Rev. Lett.*, 112, 156404 (2014)

[177] E. Wang et al., *Nat. Phys.*, 9, 621 (2013)

[178] H. Shishido, T. Shibauchi, K. Yasu, T. Kato, H. Kontani, T. Terashima, and Y. Matsuda, Science 327, 980 (2010)

[179] D. Rowe et al., *J. Phys. D: Appl. Phys.*, 35, 2183 (2002)

[180] J. W. Harter, Ph. D. thesis, Cornell University (2013)

[181] A. Y. Cho and J. RÀrthur, *Prog. Solid State Chem.*, 10, 157 (1975)

[182] D. T. J. Hurle, *Handbook of Crystal Growth, Volume 3a: Thin Films and Epitaxy*, North-Holland, Amsterdam (1994)

[183] Y. F. Nie et al., *Phys. Rev. Lett.*, 115, 096405 (2015)

[184] S. Ueda et al., *Physica C: Superconductivity*, 471, 1167 (2011)

[185] D. C. Tsui, H. L. Stormer, and A. C. Gossard, *Phys. Rev. Lett.*, 48, 1559 (1982)

[186] Y. Cordier et al., *IEEE Electron Device Lett.*, 29, 1187 (2008)

[187] K. Dasari et al., *J Electron Mater*, 45, 2071 (2016)

[188] M. Knudsen, *Ann. Phys. (Leipzig)*, 4, 999 (1909).

[189] K. Seshan, *Handbook of Thin Film Deposition: Processes and Technologies*, William Andrew Inc., New York (2002)

[190] R. F. C. Farrow, *Molecular Beam Epitaxy: Applications to Key Materials*, Noyes Publications, New Jersey (1995)

[191] D. E. Shai et al., *Phys. Rev. Lett.*, 110, 087004 (2013)

[192] J. E. Mahan et al., *J. Vac. Sci. Technol.*, A 8, 3692 (1990)

[193] A. Disa et al., *Phys. Rev. Lett.*, 114, 026801 (2015)

[194] E. J. Monkman et al., *Nat. Mater*, 11, 855 (2012)

[195] B. Burganov et al., *Phys. Rev. Lett.*, 116, 197003 (2016)

[196] J. Rondinelli and S. May, *Nat. Mater*, 11, 833 (2012)

[197] B. D. Cullity, and S. R. Stock, *Elements of X-Ray Diffraction*, Prentice Hall, Upper Saddle River, 315-326 (2014)

[198] V. M. Kuznetsov et al., *J. Mater. Sci. Technol.*, 14, 320 (1998)

[199] J. H. N. van Vucht, and K. H. J. Buschow, *J Less-Common MET.*, 10, 98 (1966)

[200] Springer Materials Data Base, *http://materials.springer.com/isp/phase-diagram/docs/c0902758* and references therein.

[201] S. Ohara, G. F. Chen, and I. Sakamoto, *J. Alloys and Compd.*, 323, 632 (2001)

[202] Z. Fisk, and M. B. Maple, *J. Alloys Compounds*, 183, 303 (1992)

[203] T. Ebihara et al., Physica B, 281/282, 754 (2000)

[204] K. Kadowaki, and S. B. Woods, *Solid State Commun.*, 58, 507 (1986)

[205] N. Tsujii, H. Kontani, and K. Yoshimura, *Phys. Rev. Lett.*, 94, 057201 (2005)

[206] P. Hohenberg and W. Kohn, *Phys. Rev.*, 136, B864 (1964)

[207] D. C. Langreth and J. P. Perdew, *Phys. Rev. B*, 21, 5469 (1980)

[208] P. Blaha et al., *Wien2k: An Augmented Plane Wave Plus Local Orbitals Program for Calculating Crystal Properties*, TU Wien, Austria, (2001)

[209] G. Zwicknagl, *Physica Scripta*, T49, 34 (1993)

[210] S. Murthy, Ph.D. Thesis, Rutgers University (2004)

[211] N. E. Bickers, D. L. Cox, and J. W. Wilkins, *Phys. Rev. B*, 36, 2036 (1987)

[212] K. R. Lea, M. J. M. Leask, and W. P. Wolf, *J. Phys. Chem. Solids*, 23, 1381 (1962)

[213] G. Zwicknagl and P. Fulde, *J Phys:Condens. Matter*, 15, S1911 (2003)

[214] T. Park, *Proc. Natl. Acad. Sci. USA*, 105, 6825 (2007)

[215] S. Maekawa et al., *J. Phys. Soc. Jpn.*, 54, 1955 (1985)

[216] A. Severing et al., *Phys. Rev. B*, 41, 1739 (1990)

[217] E. A. Goremychkin and R. Osborn, *Phys. Rev. B*, 47, 14280 (1993)

[218] D. V. Vyalikh et al., *phys. rev. Lett.*, 105, 237601 (2010)

[219] S. Patil et al., *Nat. Commun.*, 7, 11029 (2016)

[220] A. D. Christianson et al., *phys. Rev. Lett.*, 96, 117206 (2006)

[221] R. osborn et al., *J Appl. Phys.*, 85, 5344 (1999)

[222] A. P. Murani, *Phys. Rev. B*, 50, 9882 (1994)

[223] K. Kummer et al., *Phys. Rev. B*, 84, 245114 (2011)

[224] K. D. finkelstein et al., *AIP Conf. Proc.*, 1741, 030009 (2016)

[225] H. Yamaoka et al., *Phys. Rev. B*, 87, 205120 (2013)

[226] W. B. Jiang et al., *Sci. Rep.*, 5, 17608 (2015)

[227] S. Chatterjee et al., *unpublished*

[228] J. J. Joyce et al., *Phys. Rev. B*, 54, 17515 (1996)

[229] J. H. Shim, K. Haule, and G. Kotliar, *Science*, 318, 1615 (2007)

[230] I. Jarrige et al., *Phys. Rev. Lett.*, 114, 126401 (2015)

[231] L. -B. Hu and T. -H. Lin, *Commun. Theor. Phys.*, 21, 147 (1994)

[232] D. M. Newns and N. Read, *Adv. Phys.*, 36, 799 (1987)

[233] K. Kummer et al., *Phys. Rev. X*, 5, 011028 (2015)